REPUBLIQUE DU CAMEROUN
Paix - Travail - Patrie

UNIVERSITE DE YAOUNDE I

CENTRE DE RECHERCHE ET DE FORMATION DOCTORALE EN SCIENCES, TECHNOLOGIES ET GEOSCIENCES

Unité de recherche et de formation Doctorale en physiques et applications
---
B.P 812 Yaoundé
Email: crfd_stg@uy1.uninet.cm

REPUBLIC OF CAMEROON
Peace - Work - Fatherland

UNIVERSITY OF YAOUNDE I

POSTGRADUATE SCHOOL OF SCIENCES, TECHNOLOGY AND GEOSCIENCES

Research and postgraduate training unit for physics and Applications
---
P.O. Box 812 Yaounde
Email: crfd_stg@uy1.uninet.cm

DÉPARTEMENT DE PHYSIQUE
DEPARTMENT OF PHYSICS

LABORATOIRE DE MÉCANIQUE, MATÉRIAUX ET STRUCTURES
LABORATORY OF MECHANICS, MATERIALS AND STRUCTURES

Wireless Power Transfer in Parity Time Symmetry electronic circuits

Thesis submitted and defended in fulfillment of the requirements for the awards of a Doctor of Philosophy (PhD) degree in Physics

Specialty: Mechanics, Materials and Structures

Option: Fundamental Mechanics and Complex Systems

By

NJIKE NJIKE Idriss Baudouin

Registration number: 10W0630
Master in Physics

Under the supervision of:

FOTSA NGAFFO Fernande
Associate Professor
University of Yaounde I

KENFACK JIOTSA Aurélien
Professor
University of Yaounde I

UNIVERSITÉ DE YAOUNDÉ
THE UNIVERSITY OF YAOUNDE I

FACULTÉ DES SCIENCES
FACULTY OF SCIENCES

DÉPARTEMENT DE PHYSIQUE
DEPARTMENT OF PHYSICS

ATTESTATION DE CORRECTION DE LA THÈSE DE DOCTORAT/Ph.D

Nous, Professeur **NANA ENGO Serge Guy** et Professeur **WOAFO Paul**, respectivement Examinateur et Président du jury de la Thèse de Doctorat/Ph.D de Monsieur **NJIKE NJIKE Idriss Baudouin**, Matricule **10W0630**, préparée sous la direction des Professeurs **KENFACK JIOTSA Aurélien** (Université de Yaoundé I) et **FOTSA NGAFFO Fernande** (Université de Yaoundé I), intitulée :« **Wireless power transfer in parity time symmetry electronic circuits** », soutenue le lundi, **24 avril 2025**, en vue de l'obtention du grade de Docteur/Ph.D. en Physique, Spécialité **Mécanique, Matériaux et Structures,** option **Mécanique Fondamentale et Systèmes Complexes,** attestons que toutes les corrections demandées par le jury de soutenance ont été effectuées.

En foi de quoi, la présente attestation lui est délivrée pour servir et valoir ce que de droit.

Fait à Yaoundé, le 23 MAI 2025

Examinateur	Le Président du jury	Le Chef de Département de Physique
Pr. NANA ENGO Serge Guy	Pr. WOAFO Paul	Pr. NDJAKA Jean-Marie

REPUBLIQUE DU CAMEROUN
Paix - Travail - Patrie

UNIVERSITE DE YAOUNDE I

CENTRE DE RECHERCHE ET DE FORMATION DOCTORALE EN SCIENCES, TECHNOLOGIES ET GEOSCIENCES

Unité de recherche et de formation Doctorale en physiques et applications
---
B.P 812 Yaoundé
Email: crfd_stg@uy1.uninet.cm

REPUBLIC OF CAMEROON
Peace - Work - Fatherland

UNIVERSITY OF YAOUNDE I

POSTGRADUATE SCHOOL OF SCIENCES, TECHNOLOGY AND GEOSCIENCES

Research and postgraduate training unit for physics and Applications
---
P.O. Box 812 Yaounde
Email: crfd_stg@uy1.uninet.cm

DÉPARTEMENT DE PHYSIQUE
DEPARTMENT OF PHYSICS

LABORATOIRE DE MÉCANIQUE, MATÉRIAUX ET STRUCTURES
LABORATORY OF MECHANICS, MATERIALS AND STRUCTURES

Wireless Power Transfer in Parity Time Symmetry electronic circuits

Thesis submitted and defended in fulfillment of the requirements for the awards of a Doctor of Philosophy (PhD) degree in Physics

Specialty: Mechanics, Materials and Structures

Option: Fundamental Mechanics and Complex Systems

By

NJIKE NJIKE Idriss Baudouin

Registration number: 10W0630
Master in Physics

Devant le Jury Composé de :

Président :	**WOAFO Paul**	Professeur, Université de Yaoundé I
Rapporteurs:	**KENFACK JIOTSA Aurélien**	Professeur, Université de Yaoundé I
	FOTSA NGAFFO Fernande	Maître de Conférences, Université de Yaoundé I
Membres :	**NANA ENGO Serge Guy**	Professeur, Université de Yaoundé I
	SIEWE SIEWE Martin	Professeur, Université de Yaoundé I
	KENFACK SADEM Christian	Professeur, Université de Dschang

Wireless Power Transfer in Parity Time Symmetry electronic circuits

THÈSE

Thesis is submitted to the Department of Physics
in fulfillment of the requirements for the degree of Doctor
of Philosophy in field of Fundamental Mechanics and Complex Systems

By

NJIKE NJIKE Idriss Baudouin
Master in Physics

Ph.D candidate

Specialty: Mechanics, Materials and Structures

Option : Fundamental Mechanics and Complex Systems

Co-Directors:

FOTSA NGAFFO Fernande
Associate Professor
University of Yaounde I

KENFACK JIOTSA Aurélien
Professor
University of Yaounde I

University of Yaounde I
Centre de Recherche et de Formation Doctorale en Sciences, Technologie et Geosciences
B.P. Box 812 Yaoundé, Cameroon

Citation

"If you want to find the secrets of universe,
think in terms of energy, frequency and vibration."

Nikola Tesla

Dedication

♡ *To my late beloved father,*
peace to his soul ***NJIKE Joseph,***
Born around 1937 - 2001
and

♡ *To my mother*
MBEUNKWE Charlotte

Declaration

This is to certify that the research work presented in this thesis, entitled **" Wireless power transfer in Parity time symmetry electronic circuits "** was conducted by Pr. Fernande FOTSA NGAFFO under the supervision of Pr. Aurélien KENFACK JIOTSA. No part of this thesis has been submitted anywhere else for any other degree. This thesis is submitted to the Department of Physics in partial fulfillment of the requirements for the degree of Doctor of Philosophy in Field of Fundamental Mechanics and Complex Systems, Department of physics, University of Yaounde I.

Authors :

NJIKE NJIKE Idriss Baudouin
PhD candidate
University of Yaounde I

FOTSA NGAFFO Fernande
Associate Professor
University of Yaounde I

KENFACK JIOTSA Aurélien
Professor
University of Yaounde I

Acknowledgments

This thesis would have been impossible without the help and support from several people. Here, I would like to express my sincere gratitude to them.

First of all, I would like to thank **God, the Almighty** for giving me the patience, the strength and the mercy to accomplish this modest work, despite the difficulties encountered.

I would like to express my thankfulness to my advisor, **Pr. Fernande FOTSA NGAFFO**. It has not always been easy to integrate and accept your rigor in the research. That's the reason I went to your school. I learned a lot with you, patience, a job well done, discipline, thanks to your research experience, especially in the field of non-Hermitian systems. There is no doubt that I am now in this field of research thanks to you. Our many long hours of discussions have greatly influenced the way I think about research problems in general and of this thesis in particular. Thank you also, for all the advice and support you have given me over the years. As a mother, you taught me to get up in the face of difficulties, a behavior I remain proud of.

Next, I am also express my deepest gratitude and my unwavering attachment to my thesis supervisor, **Pr. Aurélien KENFACK JIOTSA**, who accepted me in his Laboratory since the Master's degree until this Ph.D thesis, where I was able to combine, throughout these years of fruitful and stimulating collaboration, the pleasures of research and intellectual complicity. I hope I have been worthy of the trust you have placed in me. I have no other ambition than to include my future works in this continuity. The clarity of this manuscript owes much to its many and necessary corrections. His sympathetic attitude and encouragements have enabled me to broaden my knowledge and improve my research skill and capability.

I would like to thank each member of jury who has accepted to evaluate the present work.

I would also like to thank all those who dedicated their time to teach me a part

of what they knew, from primary school to University, with a particular emphasis on the teaching staff of the Departments of Physics of the University of Yaounde I; I am particularly grateful to **Pr. Luc Calvin Owono Owono, Pr. Jean-Marie Bienvenu NDJAKA, Pr. Timoléon Crépin KOFANE, Pr. Paul Woafo, Pr. Clement Tchawoua, Pr. Bernard Essimbi Zobo, Pr. Serge ZEKENG, Pr. Blaise Romeo NANA NBENDJO, Pr. Bonaventure NANA, Pr. Germaine DJUIDJE KENMOE, Pr. SAIDOU, Pr. Martin SIEWE SIEWE, Pr. Serge Guy NANA ENGO, Pr. Bruno LENTA** .

Many thanks to **Dr. Emmanuel FENDZI DONFACK**, for all our many fruitful exchanges on different aspects of physics. Without forgetting his availability and unconditional help.

I express my gratitude to **Dr. Eric TALA TEBUE, Dr. Zacharie DJOUFACK, Dr. Deschances TSOBGNI, Dr. Bertin DJOB, Dr. Hervé KAMDOUM, Dr. Jean Calvin SEUTCHE** and **Dr. Jean Paul DJIOKO** for their support in job search.

Special thanks go to my academic elders and older brothers **Stéphane Boris TABEU** and **Senghor TAGOUEGNI** for their fruitful and stimulating discussions during this work and concerning research questions in general.

My gratitude also goes to all my lab mates from the ANALOGICAL SIMULATION LAB under the supervision of **Pr. Aurélien KENFACK JIOTSA**, **Pr. Fernande FOTSA NGAFFO**, **Ibrahim AZEGHAP SIMO, Armaud TIKENG, Dr. Marcial BADUIDANA, Landry SILATCHOM, Junior MBAH NDEDA, Daniel MBANG, Stephane NOUPEYI, Jean Paul TEGUIA, Rommuald TATSITSA, Cedric NGONGANG, Steve SAHLEUHEU, Dr. Calin NKOUAGNOU**, for the sincere collaboration, solidarity, spirit of group and the uplifting debates that elucidated me.

My deepest gratitude goes to my family. I want to thank my siblings: **Frederick Arnaud TOUGUEUN NJIKE, Christian YAKAM NJIKE, Floriene YOTA NJIKE and Estelle TCHOUAMBIA NJIKE**, who have always appreciated me; I remember their encouragement whenever I broach the research questions. Thank you for the education you installed in me, for the affection, the tenderness, the support, the advice and above all for the immeasurable Love that you have always shown towards me. You always remind me that " *success comes at the end of the effort*". Find here the fruit of all these works Mom!

I must remember the blessings of the members of the great families **SA' TA TCHOUAMBIA** in general and in particular my brothers and sisters in blood, for their continuous love and support throughout my life. I feel blessed to be your son, and none of this would have been possible had it not been because of your unbending belief in me.

I especially acknowledge my friends **Roberto NZIAHA NGOUNOU, Duplex TIOMELA KEMDJO, Thiéry KAMGA, Loïc Steve ALONGAMO DJIFACK, Marianne ABEMGNIGNI, Stéphanie NGANOU** and **Dr. Guy Bertrand MBOU SOH** who have always kept a place for me in their prayers and have supported me throughout this work as well as during difficult times.

To all those who have contributed directly or indirectly to this work, and whose names do not appear on this page, do not feel forgotten, we are together!

To all of you, thank you.
Idriss Baudouin.

Abstract

This thesis focuses on the study of wireless transmission in a few electronic circuits featuring parity-time symmetry (PTS), which has its origins in non-Hermitian quantum systems. The particularity of this parity and time symmetry is the ability to vary the eigenmodes of the system from a real domain to a complex domain. This is why such systems offer the possibility of switching from real to complex eigenfrequencies by adjusting the balance gain/loss parameter, which is the resistance. By applying it to our circuits, we can determine the range of parameter values for which the natural frequencies are real. In the real phase when the circuit is oscillating, the study of the transmission by mutual induction between the source and the receiver shows that the transfer is efficient and reaches almost 100% for a high value of the resistance of the gain and loss cells of the circuit. The maximum distance obtained between the coils when the transfer is still efficient is around 1.5 m for coils with four turns, and this distance increases as the number of turns increases; this transfer is efficient for certain frequency peaks. This work has shown that electronic circuits based on time parity symmetry have good signal transmission power compared with standard electronic circuits. A generalised study, taking a large number of cells in the circuit, reveals that the frequencies at which the transfer is efficient increase with the number of cells. We therefore have a multitude of frequencies that can be used to transmit information from the source to the charge.

Keywords : Parity Time symmetry, wireless power transfer, multi cells, multi frequencies, non-Hermitian systems.

Résumé

Cette thèse est axée sur l'étude de la transmission sans fil dans plusieurs circuits électroniques présentant une symétrie parité-temps (PTS) qui tire ses origines dans les systèmes non-Hermitiens en quantique. La particularité de cette symétrie parité temps est de pouvoir varier les modes propres du système d'un domaine réel à un domaine complexe. C'est ainsi que de tels systèmes offrent la possibilité de passer des fréquences propres réelles aux fréquences complexes en jouant sur un paramètre de contrôle de la compensation en gain et en perte qui est la résistance. En l'appliquant à nos circuits nous parvenons à déterminer la gamme des valeurs des paramètres pour lesquelles les fréquences propres sont réelles. Dans la phase réelle où le circuit oscille, l'étude de la transmission par induction mutuelle entre la source et le récepteur montre que le transfert est efficace et atteint presque 100% pour une valeur élevée de la résistance des cellules de gain et perte du circuit. La distance maximale obtenue entre les bobines lorsque le transfert est encore efficace est d'environ 1,5 m pour les bobines à quatre spires, et cette distance augmente au fur et à mesure que le nombre de spires augmente . Ce transfert est efficient pour certains pics de fréquences. Ces travaux démontrent que les circuits électroniques basés sur la symétrie parité temps ont une bonne puissance de transmission du signal par rapport aux circuits électroniques standard. Une étude généralisée en prennant un nombre élevé de cellules dans le circuit révèle que les fréquences auxquelles le transfert est efficient augmentent en fonction du nombre de cellules. Nous disposons donc d'une multitude de fréquences pouvant être utilisées pour transmettre l'information de la source à la charge.

Mots clés : symétrie parité temps, puissance de transfer sans fil, multi cellules, multi fréquences, systèmes non-Hermitiens.

Contents

List of Tables

List of Figures

List of Abbreviations

WPT: Wireless Power Transfer;

PT: Parity Time;

PTS: Parity Time Symmetry;

KVL: Kirchhoff Voltage Law;

KCL: Kirchhoff Current Law;

EIT: Electromagnetically Induced Transparency;

AC: Alternating Current;

MOSFET: Metal Oxide Semiconductor Field Effect Transistor;

IPT: Inductive Power Transfer;

RF: Radio Frequency;

RFID: Radio Frequency Identification;

SCMR: Strongly Coupled Magnetic Resonance;

MPT: Microwave Power Transfer;

DC: Direct Curent;

RLC: Resistor-Inductor-Capacitor;

VNA: Vector Network Analyser;

LTSPICE: Linear Technology Simulation Program With Integrated Circuit Emphasis;

General Introduction

Wireless Power Transfer (WPT) is the process where electrical energy is transmitted from a power source to an electrical load across an air gap using induction coils. these coils produce an electromagnetic field which sends energy from a transmitter to a receiver. In contrast to wireless communication systems, the electromagnetic wave in WPT systems is used by the receiver to store energy in a battery or to power electronics. The first experiments on wireless power transfer were performed by the engineer Nikola Tesla at the end of the 19th century. As described in [1], he was able to transmit power with microwaves between two objects 48 km apart. Another of Tesla's experiments consisted in powering 200 bulbs without cables, from a power source located 40 km away. For these experiments, issues related to human and electrical safety were not considered. before the 21st century, research in WPT systems had waned, but the new millennium ushered in a resurgence of interest. This renewed motivation was driven by the development of power converters in that period, which allowed the use of frequency in the range of dozens of kHz and kW operations. This had not been possible previously. It is a rapidly developing field with a wide range of potential applications, including charging mobile devices, powering medical implants, and powering sensors in remote locations. Wireless transfer is positioned as the means of connection for future networks [2] in the fields of detection, signal processing and many others. In electronic, wireless transfer systems operate on the basis of capacitive coupling [3, 4], inductive coupling [5–7] or both together [8, 9].

Non-Hermitian systems were of no particular interest and were not studied by researchers because of the complexity of their eigenvalues. They were only interested in Hermitian systems that had real eigenvalues for analyse physical phenomena. Then, around 1998, Bender turned his attention to non-Hermitian systems and found a condition that they could meet in order to have real eigenvalues [10]. Parity-time (PT) symmetry is a concept from physics that describes systems that are invariant under both parity (spatial inversion) and time reversal. Since their study, non-Hermitian systems continue to expand their applications such as, unidirectional invisibility [11–14], single-mode lasing, loss-induced suppression and revival of lasing [15–18], electromagnetically induced transparency(EIT) [19–21], ultrasensitive sensors [22–27], transmission in mechanical systems [28, 29], wireless power transfer [30–33] and many more. The technology is growing with the design of more and more wireless interconnected objects [34]. Following these ideas, the challenge remains the perpetual search for new systems that allow to improve the transmission of informations between one transmitter and receivers. PT-symmetric

systems have been shown to have a number of unusual properties, including the ability to exhibit non-reciprocity (i.e., different behavior for forward and backward waves) and the ability to support localized modes in otherwise infinite systems.

In recent years, there has been a growing interest in the use of PT symmetry to design WPT systems. PT-symmetric systems have been shown to have a number of advantages over conventional systems in WPT, including:

- Increased robustness to misalignment and other disturbances.
- Higher power transfer efficiency.
- The ability to operate over longer distances.
- The ability to charge multiple devices simultaneously.

Another approach to realise PT-symmetric WPT systems is to use nonlinear gain elements. Nonlinear gain elements can be used to create PT-symmetric systems that are more efficient and easier to implement than systems based on resonant coils. PT-symmetric WPT systems are a promising new area of research with the potential to develop new and improved WPT systems. However, there are still a number of challenges that need to be addressed before PT-symmetric WPT systems can be commercialized. One challenge is that PT-symmetric systems can be unstable, and it is important to design systems that are stable and reliable. Another challenge is that PT-symmetric systems can be sensitive to noise and other disturbances. It is important to design systems that are robust to noise and other disturbances.

PT-symmetric WPT circuits can be realized using a variety of electronic components. Some common examples include:

- Coupled resonant coils: This is the most common approach to realise PT-symmetric WPT circuits. Two resonant coils are coupled together, and the coupling coefficient is slightly asymmetrical [35, 36]. This asymmetry breaks the PT symmetry of the system, but it also allows for non-reciprocity and the formation of localized modes.
- Nonlinear gain elements: Nonlinear gain elements can be used to create PT-symmetric systems that are more efficient and easier to implement than systems based on resonant coils [37]. Some common examples of nonlinear gain elements include transistors and diodes.
- Metamaterials: Metamaterials are artificially engineered materials that can exhibit unusual electromagnetic properties. Metamaterials can be used to create PT-symmetric systems with unique properties [38, 39], such as the ability to operate over long distances.

PT-Symmetric WPT systems have a number of advantages over conventional WPT systems, including:

- Increased robustness to misalignment and other disturbances: PT-symmetric WPT systems are more robust to misalignment and other disturbances than conventional WPT systems. This is because PT-symmetric systems can support localized modes, which are less sensitive to disturbances than the extended modes that are supported by conventional WPT systems.

- Higher power transfer efficiency: PT-symmetric WPT systems can achieve higher power transfer efficiency than conventional WPT systems. This is because PT-symmetric systems can amplify the power signal, which can compensate for losses in the system.

- The ability to operate over longer distances: PT-symmetric WPT systems can operate over longer distances than conventional WPT systems. This is because PT-symmetric systems can support localized modes, which can decay more slowly over distance than the extended modes that are supported by conventional WPT systems.

- The ability to charge multiple devices simultaneously: PT-symmetric WPT systems can be used to charge multiple devices simultaneously. This is because PT-symmetric systems can support multiple localized modes, each of which can be used to charge a different device.

Following these ideas, the challenge remains the perpetual search for new systems that allow to improve the transmission of informations between one transmitter and receivers. One challenge is that PT-symmetric systems can be unstable, and it is important to design systems that are stable and reliable. Another challenge is that PT-symmetric systems can be sensitive to noise and other disturbances. It is important to design systems that are robust to noise and other disturbances.

This thesis is organised into three chapters.

∗ **Chapter 1** presents some generalities on wireless transfer theory and the PT symmetry in non-hermitian systems; which allows us to review previous works in electronics.

∗ **Chapter 2** is devoted to the methodology. Emphasis is first placed on the description of the electronic systems proposed and established theirs dynamic equations of each system. Thereafter, the standard techniques of analysis (analytical, numerical and experimental simulation methods) are applied to the different proposed models to describe them.

∗ **Chapter 3** is devoted to the presentation and analysis of the results obtained. This chapter is structured as follows: we analyse the effect of non-Hermicity on the dispersive properties in a coupled RLC oscillators by harmonic voltage. This allows to evaluate the power of wireless transfer between the source and the load in each circuit.

This dissertation work ends with a general conclusion, where we summarize our main results which have been the subject of publications. However, after a deep analysis of the results presented, some perspectives are to be considered.

Chapter 1

Literature Review : Generalities of wireless power transfer and parity time symmetry systems.

1.1 Introduction

The work carried out in this thesis focuses on wireless power transfer in electrical circuits with parity and time symmetry. To carry out this study, it is important to review the literature on wireless transmission between devices and objects enabling them to communicate without a wired connection. We will then take a look at the history of non-Hermitian systems, which led to the development of PTS systems and their implementation in various fields of physics, ending with a look at electronics.

1.2 Fundamentals of Wireless power transfer

The concept of wireless power transfer for various sources and loads have evolved since the advent of electricity in the 19th century. The scientific breakthroughs of the French scientist André-Marie Ampère (1775– 1836) and English scientist Michael Faraday (1791–1867) at the beginning of this century laid down the foundation of electricity and electromagnetism. The Ampere's law, Faraday's law, and electromagnetism form the pillars of modern electrical engineering. Their work was further enhanced by Scottish scientist James Clerk Maxwell (1831–1879) who developed the well-known Maxwell's equations for electromagnetic fields and waves. These scientific principles became the tools for early WPT pioneers, such as Tesla, Hutin, and Leblanc [40–42], to explore WPT through the use of coupled alternating magnetic field.

Nikola Tesla shown in Fig.1.1, an early pioneer in wireless power transfer (WPT), was undoubtedly the most influential scientist in this field [43, 44].In 1891, he patented the well-known "Tesla coil" in which the concept of oscillation coupling was implemented, shown in Fig.1.2. His many inventions, including AC machines, AC power generation and transmission, radio transmitters and receivers, X-ray machines, and the world's first remote-controlled technology, have been used for over a century. Some of his inventions have been improved over time, but their basic concepts are still in use today.

Between Tesla's WPT research in the late 19th century and the mid-1980s, research in WPT continued, particularly in the field of medical implants. However, commercial

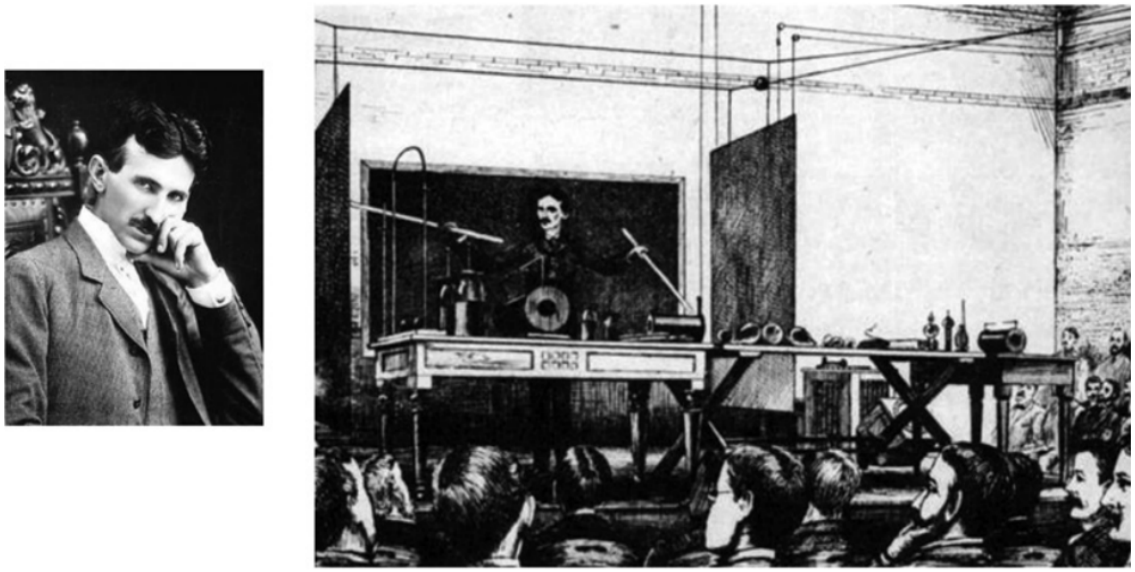

Figure 1.1: Nikola Tesla (1856–1943) and his experiment on WPT. Figure is taken from ref. [45]

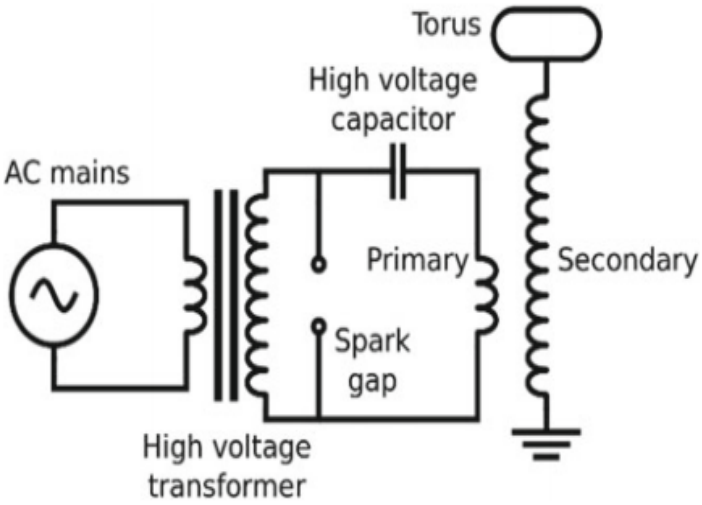

Figure 1.2: Schematic of the typical structure of a Tesla coil. Figure is taken from ref. [58]

applications of WPT were not widespread during this time. Tesla pointed out that WPT could occur through magnetic coupling at high frequency and under resonance conditions. To maintain high energy efficiency, WPT requires windings with low resistance at high-frequency operation and a high-frequency power source. While Litz wires have been available since the 1950s, high-frequency switching power electronics switches (namely power MOSFETS) did not become commercially available until the 1980s.

These historical developments of Litz wires and power electronics explain why research in magnetic resonance-based WPT took off for medical implants [46, 47] in the late 1980s and electric vehicles and inductive power [62, 63] pickups in the mid-1990s [48, 49, 61].

The dawn of the mobile phone era in the mid-1990s also prompted active research in wireless charging for portable electronics [50–55]. As shown in Fig.1.3, more and more loads are movable now and it has become important to provide seamless power to moving things such as electric transportation, robots, and electric airplanes. Currently, we mainly rely on electric cords and batteries to provide power to movables. As we notice daily, smartphones, tablets, and desktop computers should operate continuously even in the event of disconnection of utility power. The electric cord has a limited range and the battery has a limited duration; consequently, they inevitably accompany anxiety of range and duration. It is important to overcome this range and time limitation for movable things. This was the motivation for "mobile power electronics," a term the author (Dr Rim) coined in 2010. In this light, the motto of mobile power electronics can be said to be "to supply electric energy to all movable things freely."

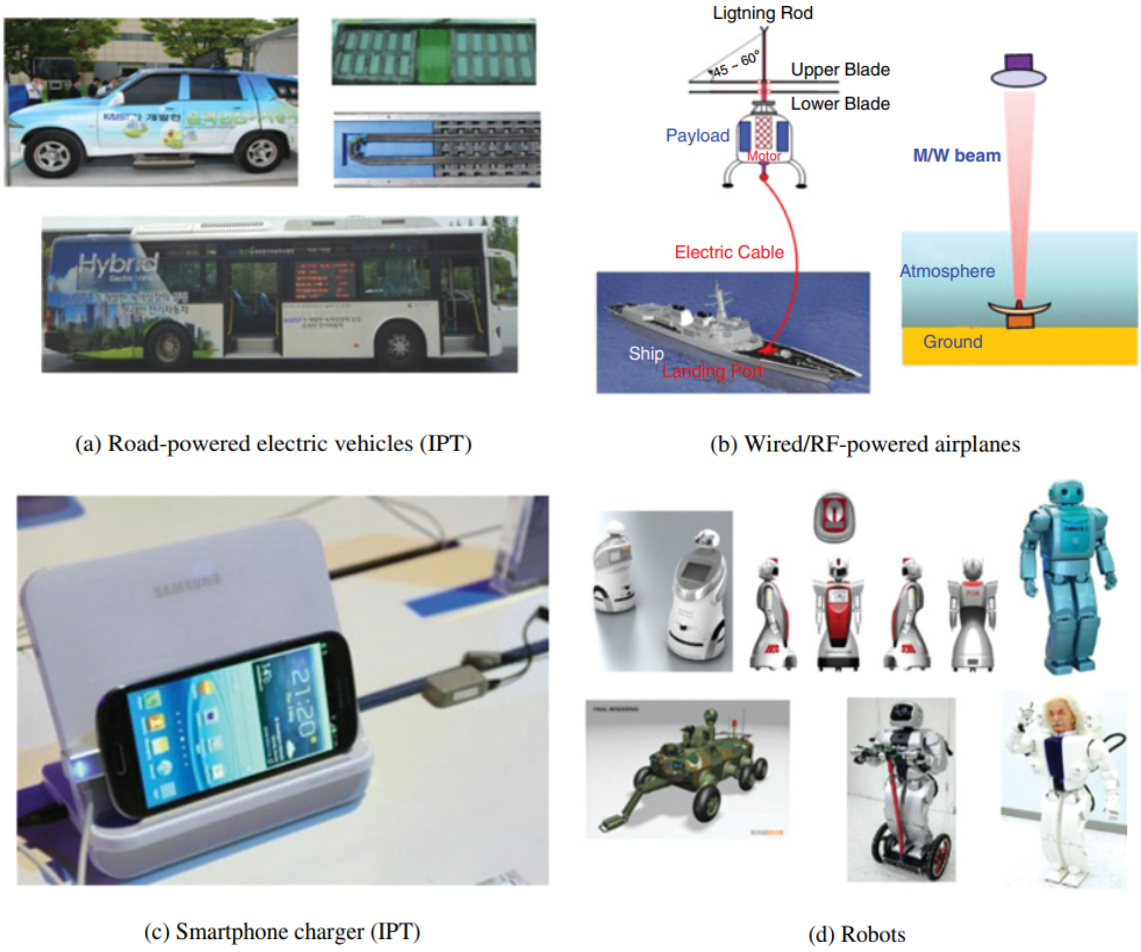

(a) Road-powered electric vehicles (IPT)

(b) Wired/RF-powered airplanes

(c) Smartphone charger (IPT)

(d) Robots

Figure 1.3: Examples of modern movable things that need seamless electric power. Figure is taken from ref. [45]

WPT technology is now a reality. We find this technology supported in commercial products such as electric toothbrushes, power mats for mobile phones and even chargers for electric vehicles. In 2017, 450 million units incorporating this capability were sold globally, primarily in smart phones, smart watches and small home appliances. This

figure represented a 75% increase on sales recorded the previous year. This significant increase is expected to continue in the near future. In fact, IHS Markit predicts that this market sector will grow to more than 2.2 billion units by 2023 [56]. This expansion will also have significant economic benefits: Navigant Research estimates that the revenue from wireless chargers will be close to 17.9 billion dollars by 2024 [57].

1.2.1 Properties and technology of wireless power transfer

1.2.2 Properties

The implementation of WPT applications varies widely. Therefore, WPT systems can be classified based on many criteria name as Direct contact, uni directional or bi-directional, gap between air and underwater or underground, low medium or high power, one or multiple transmitters and one or multiple receivers as shown in Fig.1.4.

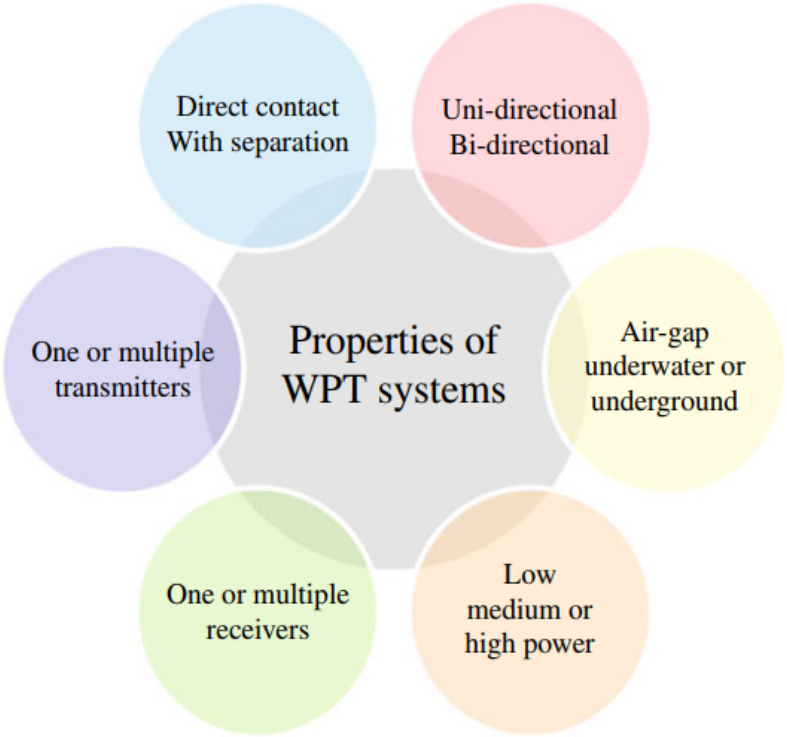

Figure 1.4: Main features of WPT systems. Figure is taken from ref. [59]

1.2.2.1 Transferred power

WPT systems comprise applications for transmitting low power (up to 1 kW), medium power (1–100 kW) and high power (more than 100 kW) [60]. The power requirement of the application greatly impacts on the system design. Thus, for low power applications, efficiency is not as crucial as in other kinds of systems. Instead, transferring the maximum power possible is usually the primary aim of low-power applications.

1.2.2.2 Uni-directional or bi-directional power transfer

According to this criterion, we can differentiate between WPT systems where the power transfer is always originated by a fixed element where a source is connected. This scheme corresponds to a uni-directional WPT. Alternatively, there are bi-directional systems where the load (a battery or a capacitor) occasionally provides energy to the source.

1.2.2.3 Gap

This term refers to the distance between the energy transmitter and the receiver. Although all WPT systems avoid cables between these two components, in some applications there must be a contact between them. This is the case with power mats. Alternatively, in some applications the transmitter and the receiver are separated by several centimeters or even meters [62–64].

1.2.2.4 Transmission with intermediate object

The Capacity to operate with intermediate objects in the gap between the power transmitter and the receiver. Due to the wavelength, some technologies cannot operate with intermediate objects, others suffer from a relevant degradation under the presence of these elements, whereas in other technologies the impact is not noticeable.

1.2.2.5 Number of transmitters

The most simple topology for a WPT system consists of one power transmitter and one power receiver. In order to extend the WPT spatial operability, several transmitters [65] can be deployed in a region in order to transfer power to a load. In this case, more than one transmitter can be activated simultaneously considering their power availability and the efficiency of the power transfer (e.g. their power resources when derived from renewable energy sources). On the other hand, the role of transferring power can be executed by a different transmitter in a different time interval. This could be appropriate for mobile loads.

1.2.2.6 Number of receivers

Although the usual topology for WPT systems considers just one receiver, there are some configurations designed to support multiple loads [65,66]. Thus, it is possible that multiple receivers can benefit from the power generated by one transmitter.

1.2.2.7 Stationary/Mobile receiver

In some applications, WPT must be able to handle the receiver being placed in a random position before the charge starts. This is the case for dynamic electric vehicle wireless charging.

1.2.2.8 Medium

Although most current WPT products operate with an air gap between the power transmitter and the receiver, this technology can also be applied in other mediums such as water [68], ground [9, 67] or biological tissue [6, 69]. The medium clearly impacts on the efficiency as it is responsible for the power transmission losses. For instance, the study carried out in [68] examined how the efficiency of the underwater WPT system is up to 5% lower than an air-gap system.

1.2.3 Technology

WPT technologies are classified into groups ranging from near-field to far-field, as shown in the figure1.5. In the near field, we have inductive, resonant and capacitive wireless energy transfer. There is an intermediate configuration, called strongly coupled magnetic resonance systems, which belongs to the intermediate operation between near-field and far-field technologies. It is important to know which group a WPT technology belongs to in order to analyse electrical systems correctly. Specifically, Maxwell's equation can be simplified by Kirchhoff's law for near-field operation, while RF analysis and optically-based equations are required for far-field operation.

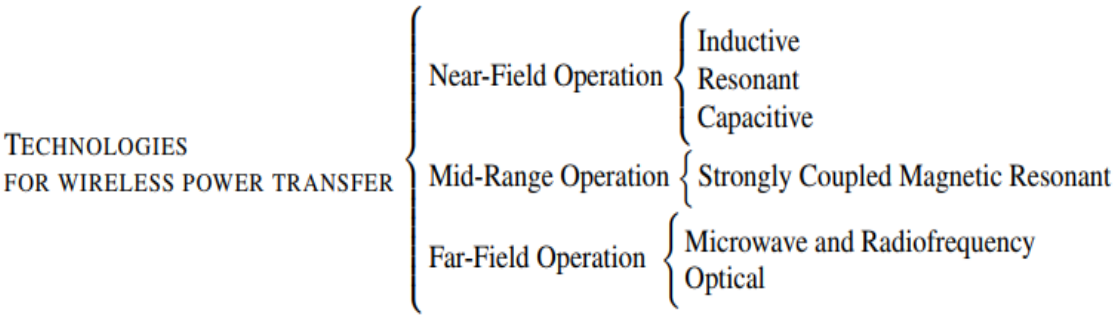

Figure 1.5: Classification of WPT technologies. Figure is taken from ref. [59]

1.2.3.1 Inductive WPT

Inductive WPT is realized with the magnetic field of the electromagnetic wave. The operation principle is explained by the interaction of the magnetic and electrical behaviour described by Ampère's Law and Faraday's Law [70, 71]. According to Ampère's Law, a current-carrying wire generates a magnetic field around it. The intensity of the magnetic field and its orientation depend on the topology of the wire. Specifically, Ampère's Law states that:

$$\oint \bar{H} dl = I \tag{1.1}$$

where $\bar{H}$ is the magnetic field intensity of the magnetic field generated by the electric current I and dl is the differential element of length along the path on which the current travels. As a consequence of this physical phenomenon, the frequency at which the intensity of the magnetic field varies is equal to the frequency of the current in the wire. Figure1.6 illustrates the magnetic field of some common structures employed in inductive wireless chargers. As shown, coils are able to concentrate the magnetic field around the area in which they are defined to a higher degree than a simple wire. As described by Ampère's Law, when a time-varying current passes through a coil, a time-varying current magnetic field is generated around this element. If that time-varying magnetic field traverses a different coil, a voltage (e_{ind}) is induced in its terminals. This effect is described by Faraday's Law as follows:

$$e_{ind} = -\frac{d\phi}{dt} \tag{1.2}$$

where ϕ is the flux of the magnetic field passing in the area limited by the coil.

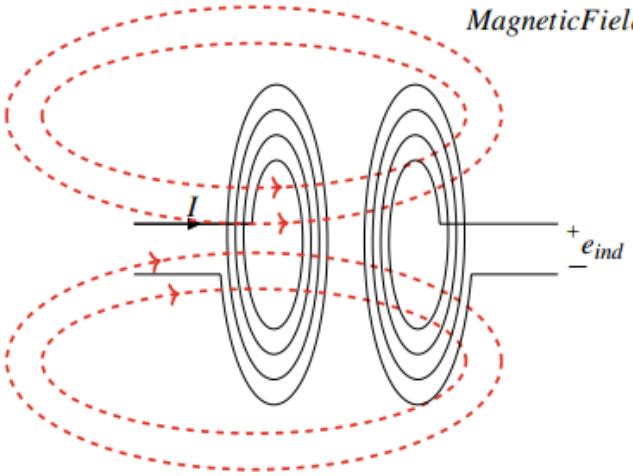

Figure 1.6: Illustration of induced voltage due to varying magnetic field. Figure is taken from ref. [59]

The combination of these two phenomena forms the basis of the inductive and other magnetic-based WPT technologies. Inductive WPT technology requires a pair of coils referred to as the primary and secondary coils. This is presented as a diagram in Fig1.7. In the primary coil, a time-varying current I_S must be produced by a generator. The magnetic field resulting from this must traverse the area of the secondary coil to which the load to be powered/charged (R_L) is connected. Between the generator and the primary coil, there are usually intermediate electronic components. Similarly, there are other electric systems between the secondary coil and the load. These additional elements are included to improve the wireless power transfer efficiency.

In general terms, we can state that the best approach is to produce an induced voltage that is as high as possible. As shown by Faraday's Law, the induced voltage is proportional to the rate of change of the flux traversing the secondary coil. This means that a coil

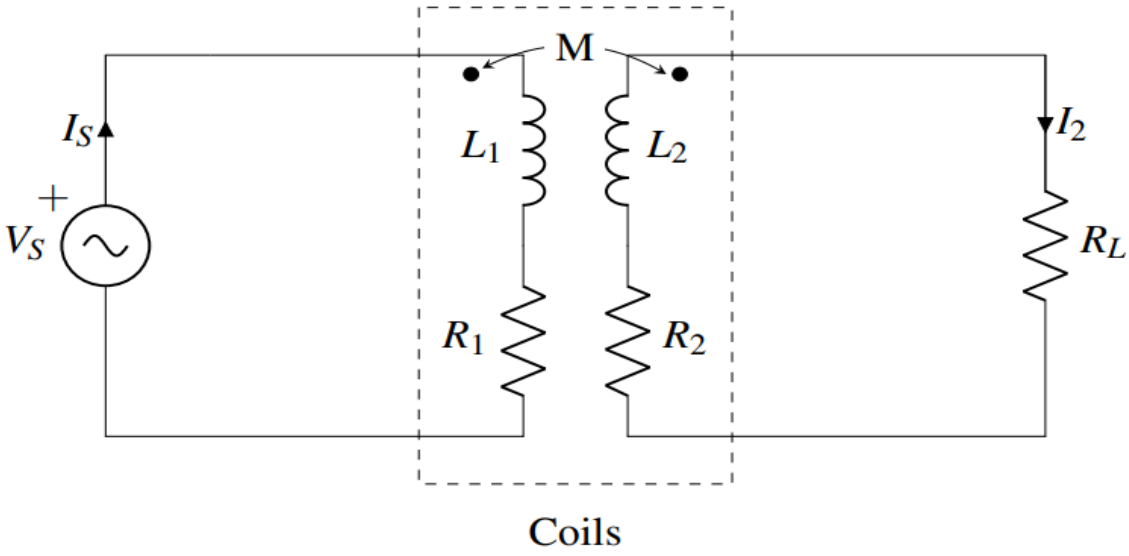

Figure 1.7: Equivalent circuit of inductive WPT. Figure is taken from ref. [59]

traversed by two magnetic fields with the same magnitude but different frequencies at two distinct moments will experience two different induced voltages. When the magnetic field passing through the coil is of the highest frequency, it will result in a higher induced voltage. Thus, the variation of magnetic flux in the secondary coil should preferably be as high as possible. Thus, it is of interest for an inductive-based WPT to hold these two conditions:

- Most of the magnetic field generated by the primary coil traverses the secondary coil.
- The frequency of the magnetic field involved in the WPT is as high as possible while allowing for a near-field operation.

The first condition initially implies that big coils are preferable on the secondary side, but the application imposes some limits for this component in terms of size, weight and cost. This restriction is clearly observed in biomedical applications. With regard to EV applications, there is a limit to the size of the coils because of the structures in which the WPT components must be inserted and the cost of the materials.Please note that WPT for EVs is not supported by inductive WPT but by advanced technologies based on this kind of magnetic WPT.

Considering that inductive WPT also benefits from a higher rate of flux change, the main strategy for enhancing the WPT in inductive systems is to increase the frequency of the electrical current in the primary coil. This will lead to an increase in the frequency of the magnetic field and, consequently, the rate of flux change is also increased. Power converters are part of the magnetic-based WPT systems in order to elevate the operational frequency. Radio Frequency Identification (RFID) and Qi are commercial technologies that are based on inductive WPT.

1.2.3.2 Magnetic Resonance WPT

Magnetic resonance or resonant WPT can be considered an improvement on inductive WPT in which the electrical system is forced to work under resonant conditions. To meet this requirement, the pair of coils is connected to structures composed of reactive elements such as capacitors or additional coils. These structures are referred to as the compensation networks. Figure1.8 shows the generic diagram of a resonant WPT system [72–74]. The most simple compensation topologies consist of a single capacitor, which may be connected to the primary and the secondary in series or in parallel. These networks are referred to as mono-resonant compensation topologies. Alternative, more complex compensation topologies are also an option. These are identified as multi-resonant compensation topologies.

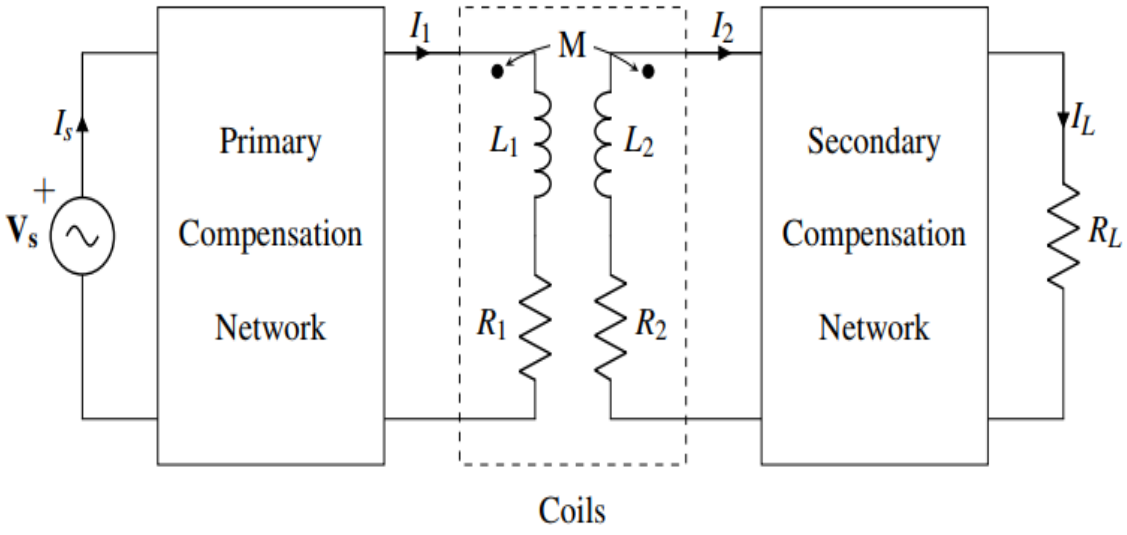

Figure 1.8: Generic diagram for magnetic resonance wireless chargers with compensation networks. Figure is taken from ref. [59]

1.2.3.3 Capacitive WPT

In contrast to the previous near-field WPT techniques, capacitive WPT is achieved by means of the electrical field. To work with a capacitive WPT, two metallic plates are inserted in the power emitter and the receiver. In each part, one plate is connected to each end of the conductors connecting the power source or the load as shown in Fig1.9.

The plates in each end of the emitter are parallel with the corresponding plates in the receiver. When the two pairs of plates are close enough, they act as two capacitors and, consequently, the electrical circuit is closed. The capacitors are identified as the forward and the return capacitors.

Under the circumstances described above, capacitive coupling takes place. Thus, an electric field is generated between the plates and, as a result, an electrical current is

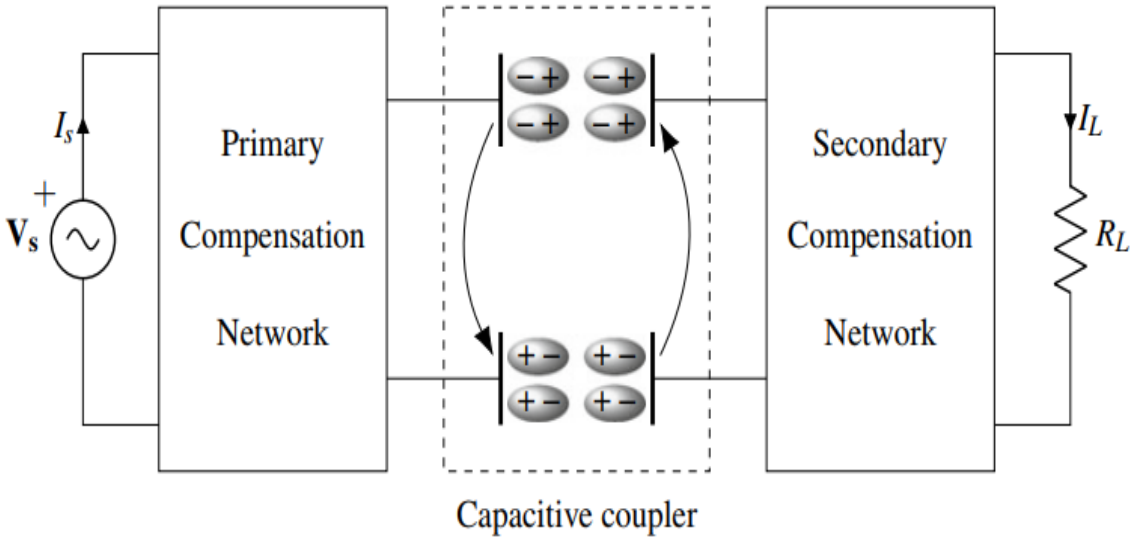

Figure 1.9: Generic diagram for capacitive wireless chargers with compensation networks. Figure is taken from ref. [59]

induced in the power receiver. Similarly to the magnetic-based WPT, the current induced in the power receiver is proportional to the rate of change of the electric field flux between the two pairs of plates. In order to increase this rate, the operational frequency is elevated from the power provided by the grid. Power converters are utilized for this purpose so that Vs is generated.

In contrast to magnetic-based techniques, capacitive WPT is able to transfer even with metallic objects [75]. The presence of these intermediate metallic objects does not greatly impact on the process as the losses are not relevant and the objects themselves do not even reach an excessive temperature in applications where capacitive WPT has been tested.

Another significant advantage lies in the fact that the electrical field is restricted to the region separating the two plates. As a result, the field of interest does not escape from this area, although this did occur with the magnetic field in the WPT techniques previously studied. At this stage, resonant technology seems to be developed enough to support a higher amount of power transfer [76].

1.2.3.4 Strongly Coupled Magnetic Resonance WPT

Strongly Coupled Magnetic Resonance(SCMR) or WPT based on magnetically coupled resonance are terms used indistinctly in the related literature. In contrast to the previous technologies, SCMR systems are considered midrange WPT as they do not fit perfectly in the near-field or the far-field operation. Although $L_{DEV} \ll \lambda$, the other two conditions put forward for near-field operation do not hold. In particular, on mid-range operations, it is also verified that $1 < d < 10L_{DEV}$ but the L_{DEV} is up to several times the distance separating the power source and the load.

The first relevant experiment involving SCMR technology was carried out by a group of researchers at the Massachusetts Institute of Technology in 2007. In this experiment, they successfully powered a light bulb without cables, with the power source located 2 m away from this component. The efficiency of the power transfer in this case was around 40%. This experiment established the main properties of SCMR circuits. They are:

- 4-coil topology. The most common configuration for SCMR circuits is a topology composed of four coupled coils: two in the power source (the driver and the transmitter) and two in the load (the receiver and the load). None of them is connected with conductors; instead they are magnetically coupled. The topology is illustrated in Fig1.10. This Figure also indicates the coupling coefficient between the coils.

- The intermediate coils are self-resonant. The transmitter and the receiver coils are used as self-resonant structures, meaning that the operational frequency of the system is set according to the free resonant frequency of these coils. This parameter is computed based on the parasitic capacitance of the intermediate coils. Taking into account the physical properties of the coils, the free resonant frequency is usually set in the interval from 100 kHz to 20 MHz.

- Compensation topologies in the driver and the load loops. The coils connected to the power source and to the load are a simple loop. As their parasitic capacitance is not relevant, it is necessary to incorporate lumped reactive components to ensure that the system works under resonant conditions.

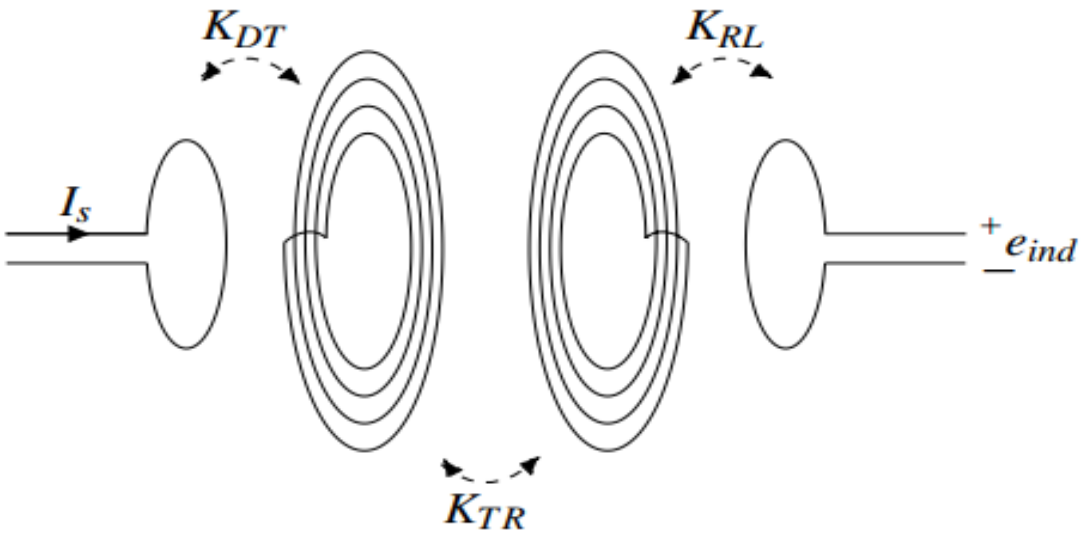

Figure 1.10: 4-coil topology in SCMR systems. Figure is taken from ref. [59]

The capacity of SCMR systems to function in the mid-range scenario depends on the 4-coil or indirect-link topology. To understand its properties, we can rely on an

equivalent two-coupled coil system. In this model, the coupling coefficient is simplified as $K_{DT} * K_{RL}/K_{TR}$, where K_{DT} is the coupling coefficient between the driver and the transmitter, K_{RL} is the coupling coefficient between the receiver and the load andK_{TR} is the coupling coefficient between the transmitter and the receiver. The coupling coefficient indicates how much of the magnetic flux of a coil is used by the other coupled coil to induce a voltage. For an efficient wireless power transfer, it is preferable to obtain coupling coefficients close to 1 while satisfying other system requirements such as the distance between the power source and the load. In general terms, the more separated two coupled coils are, the lower the coupling coefficient becomes.

If we focus on the equivalent coupling coefficient, we can observe that this parameter can be close to 1 even when the coupling coefficient between the transmitter and the receiver coils is low. This can be achieved by properly adjusting the other two coupling coefficients K_{DT} and K_{RL}. In fact, some control algorithms for SCMR systems dynamically alter the distance between the driver loop and the transmitter coil and, as a consequence, the coupling coefficient K_{DT} .

1.2.3.5 Microwave Power Transfer

Microwave Power Transfer (MPT) refers to WPT based on microwave to transfer energy in a far-field context. The procedure can also be extended to Radio-Frequency (RF) signals with minor modifications. In fact, sometimes MPT and RF power transmission are grouped into the wave-based WPT. The generic structure of a MPT is depicted in Fig1.11. From a high-voltage DC generator, a magnetron creates a microwave signal. The microwave is then sent through the antenna. The receiver processes the signal by means of a rectenna to convert the microwave signal to a DC signal. Finally, the DC signal is received by the power electronics device.

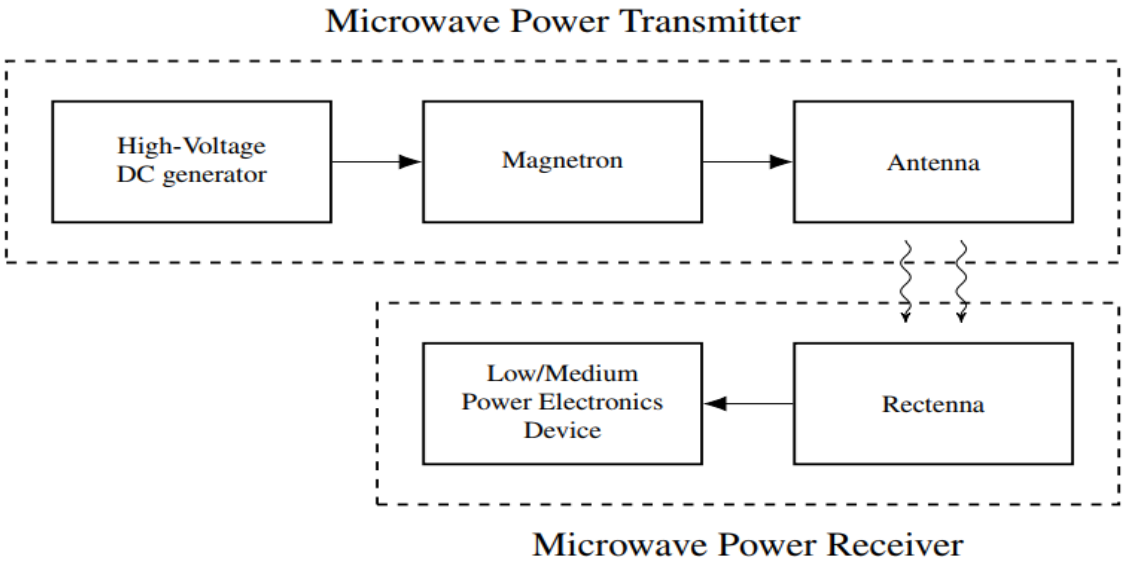

Figure 1.11: Generic diagram of a MPT system. Figure is taken from ref. [59]

As can be observed, the main elements of the MPT are:

- Magnetron. This is a vacuum tube that acts as an oscillator. From a DC excitation, the magnetron generates a microwave signal without any amplification. The frequency of the generated signal is related to the dimensions of the magnetron.

- Antenna. This corresponds to the electrical component that is able to generate an electromagnetic wave to travel to the receiver. The simplest antennas generate the signal in an isotropic way, that is, the signal has the same power in all the spatial directions. Alternatively, beam forming is possible with an array of antennas controlling the difference in the current phase [70].

- Rectenna. This stands for an antenna and a rectifying circuit built in the same component. It was designed by Charles Brown in 1960 to operate with a 2.45- GHz signal

1.2.3.6 Optical WPT

Optical WPT systems rely on electromagnetic waves with a frequency in the THz range for the power transfer. This type of wave requires the power transmitter and its receiver to be in the line-of-sight; that is, without any intermediate obstacles, as the wave cannot traverse them. If this condition holds, the gap can be up to several kilometres. This was the case with the first experiments on optical WPT. The first experiment with this technology consisted in powering a Mini Rover over a distance up to 280 m. The output power of the laser was 5 W whereas the power required by the vehicle was 1 W [2, 77]. Three years later, in 2003, another experiment was conducted by NASA. With a 1-kW laser beam, they were able to remotely power a 6-W drone [66, 78]. Other experiments with UAVs have been reported in the literature but the power and efficiency of the transfer were still reduced [77]. Moreover, this directivity can also bring an important benefit in that a controlled optical WPT does not interfere with other systems. However, nowadays electronics cannot easily adjust the direction of the beam, but this can be performed with passive elements (e.g. lens). Another clear disadvantage is the poor efficiency of these systems (around 25%) [79]. The progress on laser technology and photovoltaic cells could improve this metric in the near future.

A generic diagram of an optical WPT is shown in Fig1.12. According to this configuration, the laser diode in the transmitter is controlled by the current mode in the generator. A beam director serves to adjust the direction of the power transfer. In the receiver, a photovoltaic cell converts the received light into power with the corresponding power converters. The DC power is then used to power a load or a battery.

For low-power applications, optical WPT systems(specially in the infrared region) are safe to be used in human environments. This has prompted the commercialisation of optical WPT products for homes. Wi-Charge is an illustrative example of infrared optical WPT systems for low-power devices [79]. In its conventional configuration,the transmitter

is usually placed on the ceiling of a room. It is equipped with advanced electronics that can modify the beam so it can be aligned with the receiver. According to the specifications, they can charge up to 3 W in 1 km.

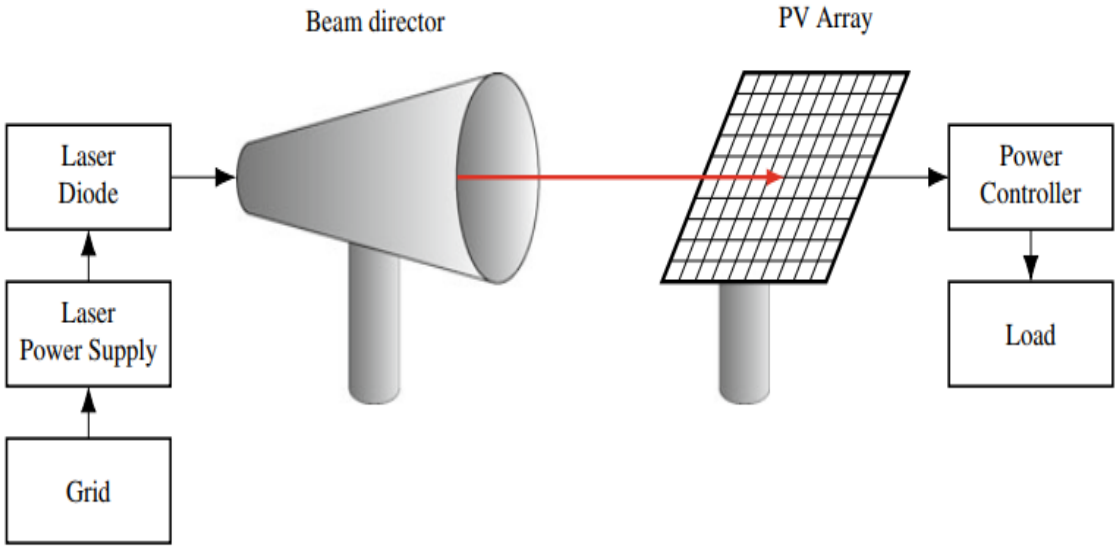

Figure 1.12: Generic diagram of a optical WPT system. Figure is taken from ref. [59]

1.3 Electronic circuit for adapting Magnetically Coupled Resonators for Wireless Power Transfer

The diagram of a wireless power system using magnetically coupled resonators is shown in figure1.13. The transmit antenna consists of a single-turn drive loop and a multi turn spiral coil. When the RF amplifier powers the drive loop, the resulting oscillating magnetic field excites the Tx coil which stores energy in the same manner as a discrete LC tank. Another way to think about this two-element transmitter is as a tuned step-up transformer, where the source is connected to the primary (the Tx loop) and the secondary (the Tx coil) is left open. The receive side functions in a similar manner, although a load replaces the power source and the system functions as a step-down transformer from the viewpoint of the receive coil.

The key interaction occurs between the two coils, each of which is a high-Q LCR tank resonator. Just as the loop and coil are magnetically coupled, the transmit and receive coils share a mutual inductance which is a function of the geometry of the coils and the distance between them. In order to gain an intuitive understanding of how magnetically coupled resonators can efficiently transfer energy back and forth, it is useful to recall the properties of coupled oscillating systems.

Consider the case of two pendulums connected by a spring, which is analogous to magnetically coupled RLC tanks [82]. In this classic physics example, the two pendulums

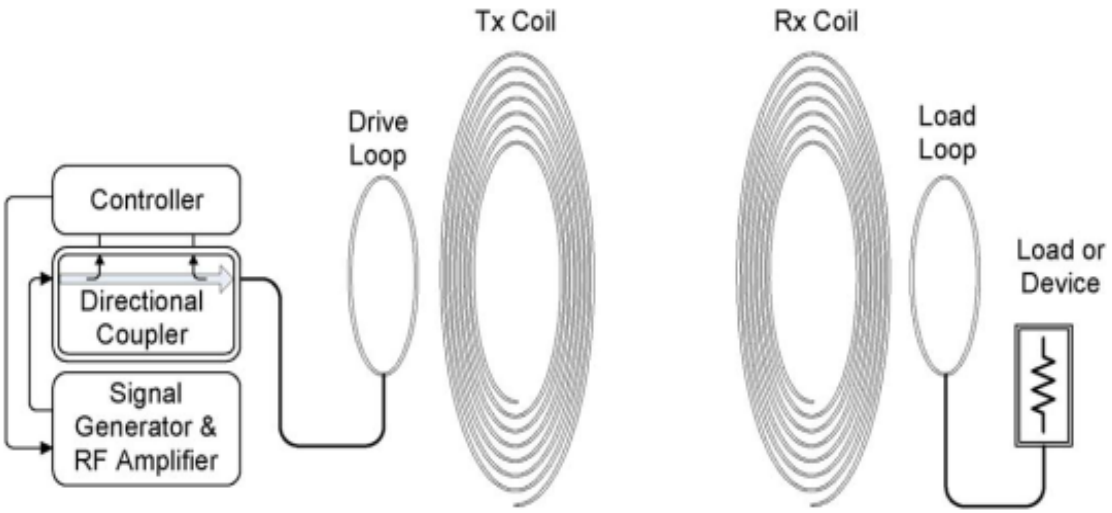

Figure 1.13: Sketch of the magnetically coupled resonant wireless power system consisting of an RF amplifier, on the left, capable of measuring the forward and reflected powers. A two-element transmitter, made of a single-turn drive loop and high-Q coil, wirelessly powers the receiver on the right. Figure is taken from ref. [81]

will form a single system which can oscillate in two modes, one of higher and one of lower frequency than the fundamental frequency of an individual pendulum. Furthermore, the frequency separation of the two modes is dependent on the stiffness (or coupling) of the spring. As this stiffness decreases, the degree of frequency separation (referred to as frequency splitting) also decreases until the two modes converge to the fundamental frequency of a single pendulum. This indicates that, when driving coupled resonators, there can be more than one mode or tuned frequency. This also means that the resonant frequency of the system will change as a function of the coupling, and in the case of the wireless power system, coupling is dependent on the distance between the transmit and receive coils.

The magnetically coupled resonator system can be represented in terms of lumped circuit elements (R, L, and C). Fig1.14 shows a straightforward circuit diagram that can be used for hand analysis or for SPICE simulations. The schematic consists of four resonant circuits, linked magnetically by coupling coefficients k_{12}, k_{23}, and k_{34}. Starting from the left, the drive loop is excited by a source with finite output impedance R_{source}. A simple one-turn drive loop can be modeled as an inductor (L_1) with parasitic resistance R_{p1}. A capacitor (C_1) is added to make the drive loop resonant at the frequency of interest. The transmit coil consists of a multiturn air core spiral inductor (L_2), with parasitic resistance (R_{p2}). The geometry of the Tx coil determines its self-capacitance, which is represented as C_2. Inductors L_1 and L_2 are connected with coupling coefficient k_{12}; the receive side is defined similarly. Finally, the transmitter and receiver coils are linked by coupling coefficient k_{23}. A typical implementation of the system would have the drive loop and Tx coil built into a single device such that k_{12} would be fixed. Similarly,

k_{34} would also be fixed. Thus, k_{23} is the remaining uncontrolled value, which varies as a function of the distances between the transmitter and receiver.

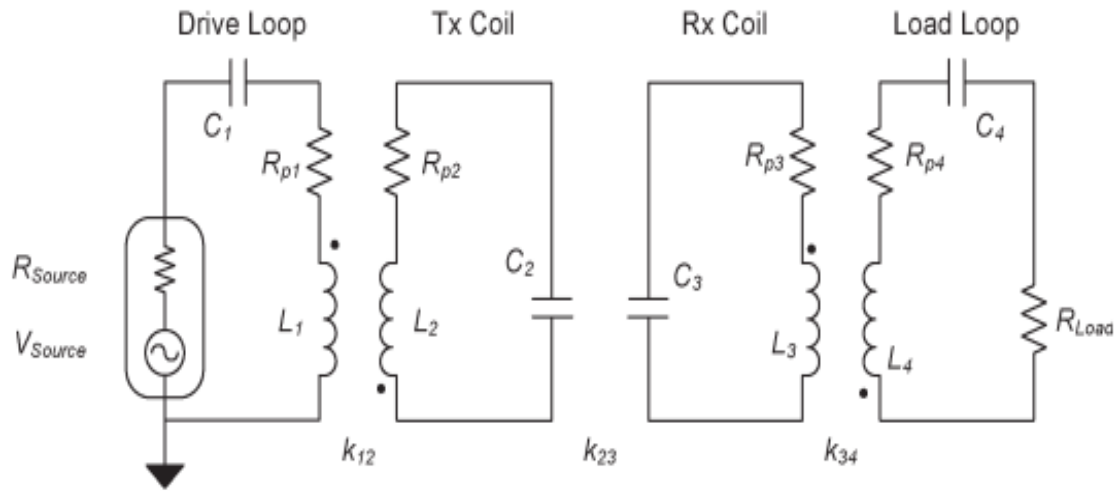

Figure 1.14: Equivalent circuit model of the wireless power system. Each of the four antenna elements is modeled as series resonators, which are linked by mutual inductances via coupling coefficients.. Figure is taken from ref. [81]

This circuit model provides a convenient reference for analysis of the transfer characteristics of a magnetically coupled resonator system. For the sake of simplicity, the cross-coupling terms (k_{13}, k_{24}, and k_{14}) are neglected in the following analysis. Section V-A provides a detailed comparison of the accuracy tradeoffs between the simplified model (Fig1.14) and complete model (which includes cross-coupling) versus measured system performance. Next, we return to the simplified model, where Kirchhoff's voltage law (KVL) can be applied to determine the currents in each resonant circuit in eq.1.3, where the coupling coefficient is defined in eq.1.4

$$\begin{aligned} &I_1\left(R_{Source}+R_{p1}+j\omega L_1+\tfrac{1}{j\omega C_1}\right)+j\omega I_2 M_{12}=V_s \\ &I_2\left(R_{p2}+j\omega L_2+\tfrac{1}{j\omega C_2}\right)+j\omega\left(I_1 M_{12}-I_3 M_{23}\right)=0 \\ &I_3\left(R_{p3}+j\omega L_3+\tfrac{1}{j\omega C_3}\right)+j\omega\left(I_4 M_{23}-I_2 M_{23}\right)=0 \\ &I_4\left(R_{Load}+j\omega L_4+\tfrac{1}{j\omega C_4}\right)+j\omega I_3 M_{34}=0 \end{aligned} \tag{1.3}$$

$$k_{xy}=\frac{M_{xy}}{\sqrt{L_x L_y}} \qquad 0\le k_{xy}\le 1. \tag{1.4}$$

These four KVL equations are simultaneously solved for the voltage across the load resistor and yield eq.1.5, with the substitution in eq.1.6. The system transfer function eq.1.5 is plotted in Fig1.15 for the circuit values shown in Table 1.1. This plot shows S_{21} magnitude as a function of frequency and coupling coefficient k_{23}. For consistency, power transfer will be represented in terms of linear magnitude scattering parameters ($|S_{21}|$),

which is important experimentally since it can be measured with a vector network analyzer (VNA) for later comparison. The entire wireless power-transfer apparatus can be viewed as a two-port network (one port being the input, fed by the source, and the other being the output, feeding the load). Using eq.1.5, one can calculate the equivalent S_{21} scattering parameter using [83,84], which results in In Fig1.15, frequency splitting is clearly visible as the value of k_{23} is increased. A SPICE simulation reveals that, indeed, the lower frequency mode of the two coils is in phase, while the higher frequency mode is 180° out of phase. As the coupling between the coils decreases, the frequency separation also decreases until the two modes converge at fo. This point is called the critical coupling point and represents the farthest distance at which maximum power efficiency is still achievable (since k_{23} is proportional to $1/distance3$). When k_{23} is greater than $k_{critical}$, the system is said to be overcoupled, and operating at either resonance will result in maximum power-transfer efficiency. Conversely, when k_{23} is less than kcritical, the system is undercoupled, and the amount of power delivered to the load begins to fall off precipitously with distance. The red dashed box outlined in Fig. 3 encloses the "magic regime" where near-constant efficiency versus distance can be achieved if the correct frequency is selected. This is dramatically different from typical far- or near-field systems where efficiency drops off rapidly with distance.

$$\frac{V_L}{V_S} = \frac{i\omega^3 k_{12}k_{23}k_{34}L_2L_3\sqrt{L_1L_4}R_{load}}{(k_{12}^2k_{34}^2L_1L_2L_3L_4\omega^4 + Z_1Z_2Z_3Z_4 + \omega^2(k_{12}^2L_1L_2Z_3Z_4 + k_{23}^2L_2L_3Z_1Z_4 + k_{34}^2L_3L_4Z_1Z_2))} \tag{1.5}$$

$$\begin{aligned} Z_1 &= R_{p1} + R_{Source} + j\omega L_1 - j/(\omega C1) \\ Z_2 &= R_{p2} + j\omega L_2 - j/(\omega C2) \\ Z_3 &= R_{p3} + j\omega L_3 - j/(\omega C3) \\ Z_4 &= R_{p4} + R_{Load} + j\omega L_4 - j/(\omega C4) \end{aligned} \tag{1.6}$$

$$S_{21} = 2\frac{V_{Load}}{V_{Source}}\left(\frac{R_{Souce}}{R_{Load}}\right)^{1/2} \tag{1.7}$$

The frequency splitting is further investigated in Fig1.16, which shows the calculated and measured magnitudes for each mode of the system as a function of distance (left) along with the resonant frequency of each mode as a function of distance (right). Here, the derivative of the transfer function is taken with respect to ω and set to zero to calculate the maximum magnitude for a given distance. The discontinuity in the prediction of the high frequency branch occurs when the two modes begin to merge near the critical coupling point. This results in a non zero slope for the peaks of the smaller high-frequency mode, and thus, the derivative does not reach zero. Here, the circuit model plus Neumann's formula shows a good prediction of the performance of the wireless power system. The magnitude versus frequency plot in Fig. 10 shows a noticeable underprediction for the high-frequency mode at small distances.

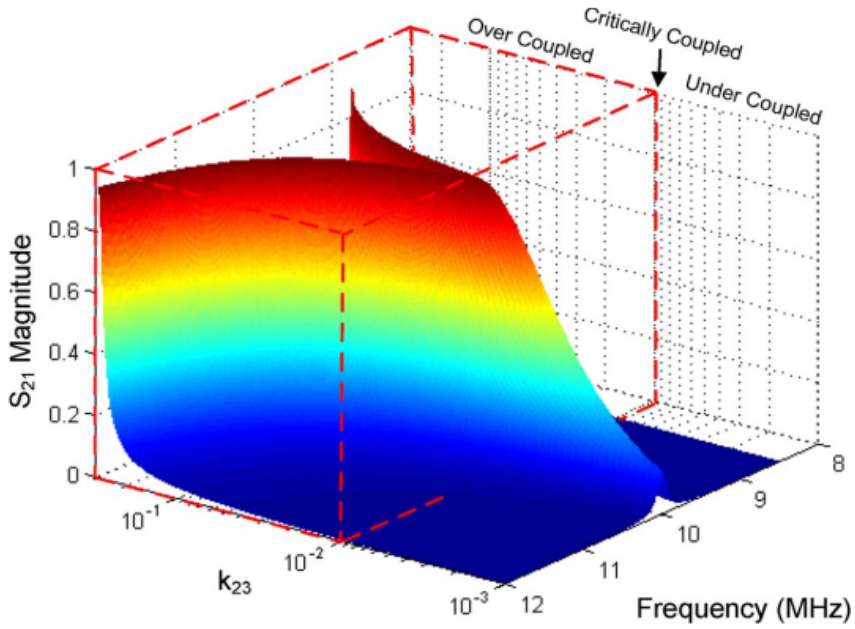

Figure 1.15: S_{21} magnitude as a function of frequency and transmitter-to-receiver coupling k_{23} for the simplified circuit model given the values in Table1.1. The highlighted red volume is the overcoupled regime, where frequency splitting occurs and transfer efficiency can be maintained independent of distance if the correct frequency is chosen. Figure is taken from ref. [81]

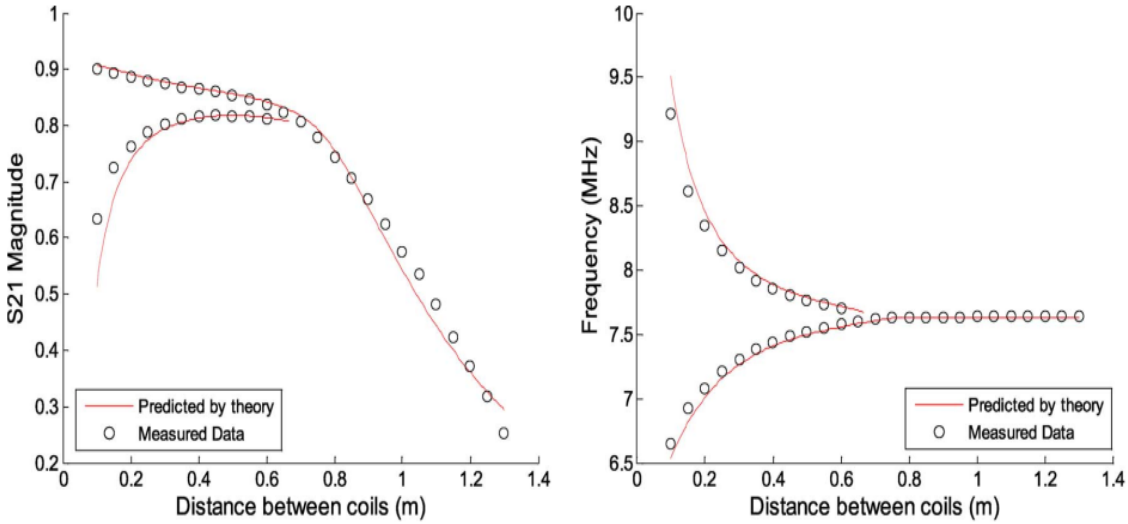

Figure 1.16: Calculated and measured frequency splitting values plotted as a function of distance. The S_{21} magnitude of the two modes is shown on the left, and the frequency of the two modes is shown on the right. Figure is taken from ref. [81]

Parameter	Value
R_{Source},R_{Load}	50Ω
L_1, L_4	1.0uH
R_{p1},R_{p4}	0.25Ω
C_1,C_4	235pF
k_{12},k_{34}	0.10
L_2,L_3	20.0uH
C_2,C_3	12.6pF
R_{p2},R_{p3}	1.0Ω
k_{23}	0.0001 to 0.30
f_0	10MHz
Frequency	8MHz to 12MHz

Table 1.1: Circuit values used to evaluate simplified model.Table is taken from ref. [81].

1.4 Parity time symmetry systems

Non-Hermitian systems are quantum systems whose Hamiltonians are not Hermitian. In other words, their Hamiltonians do not satisfy the condition H† = H, where H† is the Hermitian conjugate of H. This means that the eigenvalues of non-Hermitian Hamiltonians can be complex, which has a number of important consequences for the behavior of these systems. The study of non-Hermitian systems dates back to the early days of quantum mechanics.

In 1926, Erwin Schrödinger published a paper on the quantization of the harmonic oscillator [85], in which he showed that the Hamiltonian for the harmonic oscillator is non-Hermitian if the oscillator is subjected to a time-dependent force. In the 1940s and 1950s, there was a renewed interest in non-Hermitian systems, particularly in the context of scattering theory. This is because the scattering matrix [86], which describes the scattering of particles by a potential, is non-Hermitian. In the 1960s and 1970s, there was a growing interest in the application of non-Hermitian systems to a variety of fields, including optics, condensed matter physics, and nuclear physics. This is because non-Hermitian systems can exhibit a number of unusual properties [92–97], such as non-reciprocity and the ability to support localized modes.

In recent years, there has been a resurgence of interest in non-Hermitian systems [87, 88], particularly in the context of parity-time (PT) symmetry [10, 89–91]. PT symmetry is a symmetry that combines parity (reflection) and time reversal. PT-symmetric systems have been shown to exhibit a number of remarkable properties, such as the ability to support real-valued eigenvalues and the ability to amplify signals. Whether for linear or non-linear systems, the concept of PT -symmetry has opened up new avenues for intriguing phenomena such as double refraction [98], optical solitons [99,100], Bloch oscillations [101], spectral singularities [102, 103], non-linearity induced PT -symmetry breaking [104, 105], power oscillations and phase singularities [106], PT S wave chaos [107], perfect optical absorption [108,109], unidirectional invisibility [110,121], Talbot effect [111], defect states [112], loss-induced suppression and revival of lasing [113], thresholdless PT -symmetry breaking [114, 121], resonant mode conversion [115], optical tunneling [116], asymmetric chirality [117], directional lasing [118], polarization mode conversion [119], wireless power transmission [120,122,123], etc. In light of diverse applications of PTS systems, this thesis will restrict its scope to the field of PT -symmetry in electronics.

1.4.1 Basis of PT symmetry

Parity (P) and Time-reversal (T) transformations are fundamental symmetry operations in physics. Mathematically, they are defined by their actions on physical variables such as position, momentum and time parameter t. P is a linear operator defined by a spatial inversion of the system. In a one dimensional system, this corresponds to the reflection $x \to -x$ across one spatial axis. Any physical quantity dependent on odd powers of x or

its derivatives such as momentum p_x are inverted as well. In quantum theory, P operates on the position operator $\hat{x}$ and the momentum operator $\hat{p}$ as follows [87]:

$$P : (j,\, \hat{x},\, \hat{p}) \to (j,\, -\hat{x},\, -\hat{p})\,. \tag{1.8}$$

Therefore, the simplest representation of P in two dimensions is given by

$$P = \sigma_{\mathbf{x}} = \begin{pmatrix} 0 & 1 \\ 1 & 0 \end{pmatrix}. \tag{1.9}$$

T on the other hand is an anti-linear operator (that is complex conjugation) which reverses the time $t \to -t$. Any physical quantity dependent on odd powers of t such as momentum is reversed. In the context of wave theories, the T operator is equivalent to the transformation $i \to -i$. So, T has the effect to change the sign of quantum mechanics operators as follows:

$$T : (j,\, \hat{x},\, \hat{p}) \to (-j,\, \hat{x},\, -\hat{p}) \tag{1.10}$$

Hence, in two dimensions the T operator is defined as

$$T = \begin{pmatrix} 1 & 0 \\ 0 & 1 \end{pmatrix} \mathcal{K}, \tag{1.11}$$

where $\mathcal{K}$ denotes the complex conjugate operation. Another property is that the square of both P and T is the identity operator ($P^2 = T^2 = 1$) and the two reflection operators commute with each other.

$$[P; T] = PT - TP = 0, \tag{1.12}$$

therefore, the PT operator performs the following transformation :

$$PT : (j,\, \hat{x},\, \hat{p}) \to (-j,\, -\hat{x},\, -\hat{p})\,. \tag{1.13}$$

1.4.2 PT symmetry operator

While systems invariant under parity P or time-reversal T transformations or both have been thoroughly studied, there has also been much interest in systems which do not obey P or T symmetries separately but which respect the combined PT symmetry. A system is said to be PT symmetric if the Hamiltonian H which is described it, in addition to obey $H = H^{PT}$ [124, 125], commutes with a joint PT operator, that is,

$$[H; PT] = HPT - TPH = 0, \tag{1.14}$$

To better understand, if we consider a simple Hamiltonian H expressed in the form of position and momentum operator $H = p^2 + V(r)$ where $V(r)$ represents a potential, for a

real value of $V(r)$, H is Hermitian, (i.e. $H = H^{\dagger}$, where † denotes the adjoint, conjugate transpose, operation) and holds entirely real eigenvalues. The PT -symmetric condition on the Hamiltonian H requires that the potential should satisfies the relation: $V(r) = V^{*}(r)$ implying that the real and imaginary parts of the complex potential be even and odd function of space, respectively: $\Re(V(r)) = \Re(V(-r))$ and $\Im(V(r)) = -\Im(V(-r))$.

In general, non-Hermitian Hamiltonians are used to describe phenomenology of many physical dissipative systems. Then, a PTS system can be constructed by adding parity-symmetric, balanced energy gain/loss elements to a conservative, symmetric system. Due to these elements the system is non-conservative, but the balanced gain and loss can result in net energy conservation of the solutions to the system. As the degree of the balanced gain/loss γ that controls the non-Hermiticity [126] is increased, the solutions can undergo a sudden transition from net conservation (the exact phase) to net non-conservation (the broken phase); this spontaneous PT symmetry breaking is one of the fundamental properties of PT symmetric systems. For low but non-zero γ, the spectrum can be entirely real with H and PT sharing the same eigenvectors, that is $[H; PT] = 0$; the system is in the exact phase. However, as γ is increased, past a critical point γ_{PT} , the eigenvectors of H cease to be eigenvectors of PT , that is, $[H; PT] \neq 0$, and the spectrum becomes complex; the system is in the broken phase. The critical point is known in the literature as an Exceptional point (EP) [98] and its presence in PT S systems have special significance for many technological applications ranging from non-reciprocal devices [127, 128] to ultra-sensitive measurement devices [120, 122, 123, 129–131].

1.4.3 Electronic systems

The advent of PT systems in electronic circuits not only promises a new generation of electronic structures and devices, but also provides a platform for the detailed investigation of many new concepts in a framework of readily available experimental configurations. A first example was the demonstration in [132] that a pair of coupled LRC circuits, one with amplification and the other with equivalent attenuation, is the simplest experimental realisation of a PT symmetric system. One of the most convenient advantages of an electronic approach is that, at least in the low frequency domain, where the wavelength is significantly greater than the dimensions of the circuit, all spatial symmetry considerations can be reduced to a matter of network topology defined through the application of Kirchoff's laws. Physical symmetry is irrelevant as long as the network has the desired node topology and the connecting elements are appropriately valued. Analogous to the familiar case of a PT -symmetric potential, the parity operation is equivalent to the interchange of labels corresponding to pairs of associated circuit components. The set up of the so-called PT-dimer is depicted in Fig1.17(a). The loss is simply generated with a resistance R whereas gain is introduced via negative resistance $-R$. Figure 1.17(b) illustrates how an ideal linear amplifier can be configured to achieve negative resistance.

Figure1.18 shows the PTsymmetric dimer, the simplest configuration with a non trivial

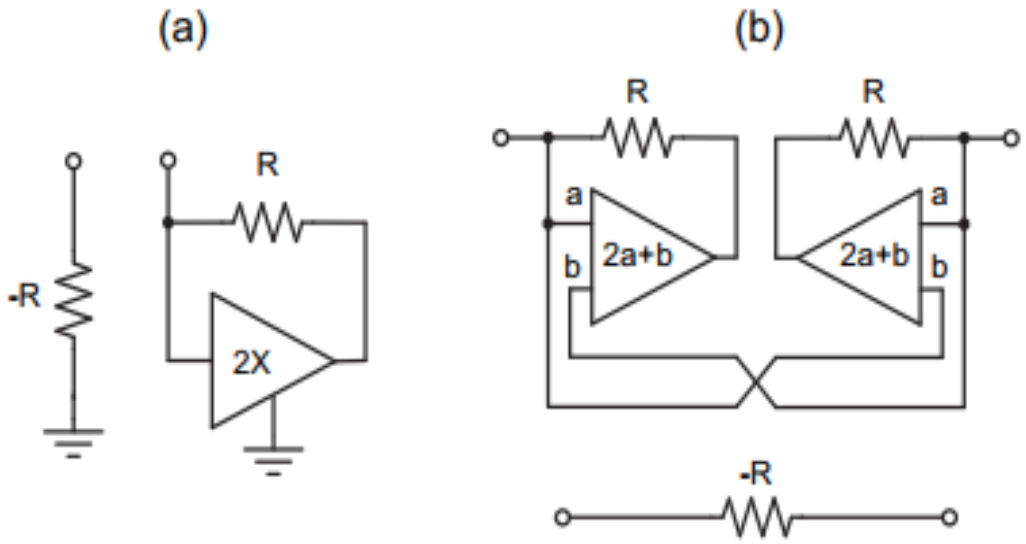

Figure 1.17: Two negative impedance converters with their equivalents. (a) A ground referenced negative resistance node. (b) A floating, two-terminal negative resistance. Figure is taken from ref. [132]

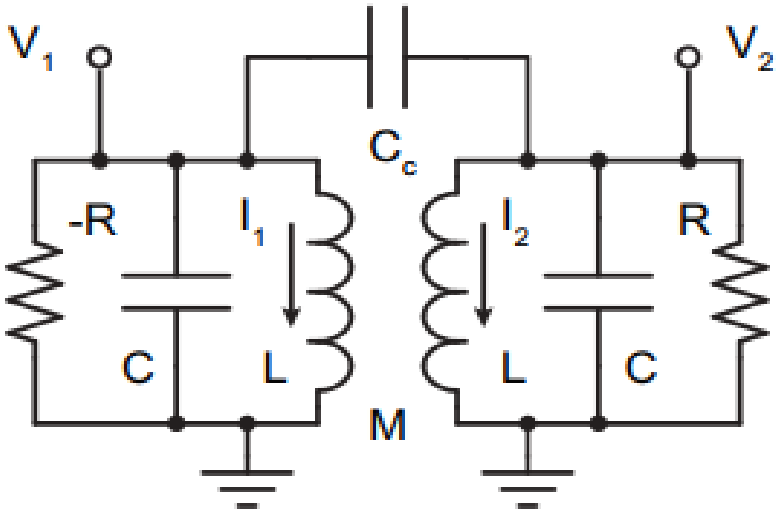

Figure 1.18: Schematic of the PT -symmetric electronic dimer. Both mutual inductance coupling and capacitive coupling are included for generality. Figure is taken from ref. [132]

(more than one mode) pseudo Hermitian spectrum. Both capacitive and mutual inductive coupling are included for generality, although the experimental results presented throughout this work are exclusively one or the other. The gain side on the left of Fig1.18 is indicated by $-R$ and was implemented using the configuration of Fig1.17(a). The loss on the right is achieved with a conventional resistance of the same value, resulting in the gain/loss parameter $\gamma = R^{-1}\sqrt{L/C}$ for this system. Kirchoff's laws for the dimer with both mutual inductance coupling and capacitive coupling between the oscillators are given for the gain (Eq.1.15) and loss side (Eq.1.16).

$$V_1 = i\omega\left(LI_1 + MI_2\right) \qquad I_1 - \frac{V_1}{R} + i\omega C V_1 + i\omega C_c\left(V_1 - V_2\right) = 0 \tag{1.15}$$

$$V_2 = i\omega\left(LI_2 + MI_1\right) \qquad I_2 + \frac{V_2}{R} + i\omega C V_2 + i\omega C_c\left(V_2 - V_1\right) = 0 \tag{1.16}$$

Eliminating the currents from the relations, scaling frequency and time by $\omega_0 = \sqrt{L/C}$, and taking $\mu = M/L$ and $c = C_c/C$ gives the matrix equation:

$$\begin{pmatrix} \frac{1}{\omega(1-\mu^2)} - \omega\left(1+c\right) - i\gamma & \omega c - \frac{\mu}{\omega(1-\mu^2)} \\ \omega c - \frac{\mu}{\omega(1-\mu^2)} & \frac{1}{\omega(1-\mu^2)} - \omega\left(1+c\right) + i\gamma \end{pmatrix} \begin{pmatrix} V_1 \\ V_2 \end{pmatrix} = 0 \tag{1.17}$$

At this point, it is obvious that the system is PT symmetric: swapping the indices and changing the sign of i leaves the equations unchanged. This linear, homogeneous system has four normal mode frequencies, as required to fulfill any arbitrary initial condition for voltage and current, given by

$$\omega_{1,2} = \pm\frac{\sqrt{\gamma_c^2 - \gamma^2} + \sqrt{\gamma_{PT}^2 - \gamma^2}}{2\sqrt{1+2c}}; \qquad \omega_{3,4} = \pm\frac{\sqrt{\gamma_c^2 - \gamma^2} - \sqrt{\gamma_{PT}^2 - \gamma^2}}{2\sqrt{1+2c}}; \tag{1.18}$$

with the PT symmetry breaking point identified as

$$\gamma_{PT} = \left|\frac{1}{\sqrt{1-\mu}} - \sqrt{\frac{1+2c}{1+\mu}}\right|; \tag{1.19}$$

and the upper critical point by

$$\gamma_c = \frac{1}{\sqrt{1-\mu}} + \sqrt{\frac{1+2c}{1+\mu}}. \tag{1.20}$$

The given forms explicitly show all of the relationships among the critical points and the real and imaginary parts of the frequencies. The exact phase, $0 < \gamma < \gamma_{PT}$, is characterized by four purely real eigenfrequencies coming in two pairs of positive $\omega_1, \omega_3 > 0$ and negative $\omega_2, \omega_4 < 0$ values, while in the broken phase below the upper critical point, $\gamma_{PT} < \gamma < \gamma_c$ the eigenfrequencies are coming in complex conjugate pairs with non-vanishing real parts, and above γ_c, as two purely imaginary complex conjugate pairs. The broken phase of the PT dimer is unstable, in that it is ultimately dominated by an exponentially growing mode. The normal modes in the exact phase are characterized by equal magnitudes for the voltage oscillations in the gain and loss sides, which in the $+\omega$, real part convention allowed by the real eigenfrequencies, are given by

$$\begin{pmatrix} V_1 \\ V_2 \end{pmatrix}_{\pm} = \frac{1}{\sqrt{2}} \begin{pmatrix} 1 \\ -\exp\left(i\phi_{\pm}\right) \end{pmatrix} \tag{1.21}$$

with a phase $i\phi_{\pm}$ of the loss side

$$\phi_{\pm} = \frac{\pi}{2} - \tan^{-1}\left[\frac{1}{\gamma}\left(\frac{1}{(1-\mu^2)\,\omega_{\pm}} - (1+c)\,\omega_{\pm}\right)\right]. \tag{1.22}$$

As the gain/loss parameter traverses the exact region, $0 < \gamma < \gamma_{PT}$, the phase progresses from the in- and out-of-phase configuration of a Hamiltonian coupled oscillator, to a mode coalescence at γ_{PT} with $\phi_{\pm} \sim \pi/2$ with the real frequency

$$\omega_{+} = \omega_{-} = \left[\left(1-\mu^2\right)(1+c)\right]^{-1/4}. \tag{1.23}$$

Examination of the inductor currents,

$$\begin{pmatrix} I_1 \\ I_2 \end{pmatrix}_{\pm} = \begin{pmatrix} \frac{1}{1-\mu^2} & -\frac{\mu}{1-\mu^2} \\ -\frac{\mu}{1-\mu^2} & \frac{1}{1-\mu^2} \end{pmatrix} \begin{pmatrix} V_1 \\ V_2 \end{pmatrix}_{\pm} \tag{1.24}$$

reveal phase shifts, relative to the corresponding voltages, that advance on the gain side and retard on the loss side within either mode. This is as required for the net transfer of electrical energy from the gain side to the loss side as the gain/loss parameter increases. This evolutionary behavior is helpful in understanding the spectral and dynamical behavior of the dimer.

An alternate analysis of the dimer is also accomplished by recasting Kirchoff's laws, Eqs.1.15 and Eq.1.16 into a "rate equation" form by making use of a Liouvillian formalism

$$\frac{d\Psi}{d\tau} = L\Psi; \quad L = \begin{pmatrix} 0 & 0 & 1 & 0 \\ 0 & 0 & 0 & 1 \\ -\alpha\beta & \alpha\zeta & (1+c)\,\gamma & c\gamma \\ \alpha\zeta & -\alpha\beta & -c\gamma & -(1+c)\,\gamma \end{pmatrix} \tag{1.25}$$

where $\alpha = 1/(1-\mu^2)$,$\beta = 1 + c\,(1+\mu)$, $\zeta = c + \mu\,(1+c)$ and $\Psi \equiv (Q_1;\, Q_2;\, Q_3)^T$ with $Q_n = CV_n$. This formulation opens new exciting directions for applications of generalized PT -mechanics [97] as it can be interpreted as a Schrödinger equation with non-Hermitian effective Hamiltonian $H_{eff} = i\mathcal{L}$. This Hamiltonian is symmetric with respect to generalized P_0T_0 transformations, i.e. $[P_0T_0;\, H_{eff}] = 0$, where

$$P_0 = \begin{pmatrix} \sigma_{\mathbf{x}} & 0 \\ 0 & \sigma_{\mathbf{x}} \end{pmatrix}; \qquad T_0 = \begin{pmatrix} \mathbf{I} & 0 \\ 0 & -\mathbf{I} \end{pmatrix} \mathcal{K} \tag{1.26}$$

and $\sigma_{\mathbf{x}}$ is the Pauli matrix, $\mathbf{1}$ is the 2x2 identity matrix, and $\mathcal{K}$ denotes the operation of complex conjugation. By a similarity transformation $\mathcal{R}$ [29],

$$R = \begin{pmatrix} \frac{2i(b+d)}{1+\sqrt{1+2c}} & -\frac{2i(b+d)}{1+\sqrt{1+2c}} & \frac{-1-2c+\sqrt{1+2c}}{c} & \frac{-1-2c+\sqrt{1+2c}}{c} \\ \frac{i\left(-1-2c+\sqrt{1+2c}\right)(b-d)}{c} & \frac{i\left(-1-2c+\sqrt{1+2c}\right)(b-d)}{c} & \frac{2}{1+\sqrt{1+2c}} & -\frac{2}{1+\sqrt{1+2c}} \\ \frac{i\left(1+2c-\sqrt{1+2c}\right)(b-d)}{c} & \frac{i\left(1+2c-\sqrt{1+2c}\right)(b-d)}{c} & \frac{2}{1+\sqrt{1+2c}} & -\frac{2}{1+\sqrt{1+2c}} \\ \frac{2i(b+d)}{1+\sqrt{1+2c}} & -\frac{2i(b+d)}{1+\sqrt{1+2c}} & \frac{1+2c-\sqrt{1+2c}}{c} & \frac{1+2c-\sqrt{1+2c}}{c} \end{pmatrix} \tag{1.27}$$

$H_{eff} = R^{-1}HR$ can be related to a transposition symmetric, PT-symmetric Hamiltonian $H = H^T = PH^\dagger P$, $T = \mathcal{K}$ where $P = RP_0R^{-1}$. The matrix H is then

$$H = \begin{pmatrix} 0 & b+ir & d+ir & 0 \\ b+ir & 0 & 0 & d-ir \\ d+ir & 0 & 0 & d-ir \\ 0 & d-ir & d-ir & 0 \end{pmatrix} \tag{1.28}$$

where $b = \sqrt{\alpha\left(\beta + \sqrt{\beta^2-\zeta^2}\right)/2}$, $d = \sqrt{\alpha\left(\beta - \sqrt{\beta^2-\zeta^2}\right)/2}$ and $r = \frac{1}{2}\sqrt{1+2c}\gamma$.

The frequencies and normal modes within this framework are identical to Eqs.1.18 and Eqs.1.24. These normal mode properties can be measured in our electronic dimer by simultaneous observation of the node voltages V_1 and V_2 of Fig.1.17 2. The set-up allows detailed analysis for gain/loss parameters γ on either side of the PT-phase transition point. In the exact phase, time series samples are captured with the dimer slightly unbalanced to marginally oscillate the mode of interest. Beyond the critical point, a transient sample is obtained dominated by the exponentially growing mode.

In Fig.1.19 we report measurements for the dimer frequencies (left) and inter-component phases (right) compared with the theoretical expressions, Eq.1.18 and Eq.1.22 respectively, for the values $\mu = 0.2$ and $c = 0$. The PT symmetry imposes the condition that the magnitude of the two voltage components are equal to one-another in the exact phase. This property is also experimentally observed. For $\gamma = 0$, the phases corresponding to the symmetric and antisymmetric combination are $\phi_- =$ and $\phi_+ = \pi$, respectively. When γ is subsequently increased and the system is below the PT threshold, the eigenstates are not orthogonal and their phases can be anywhere (depending on $\gamma = \gamma_{PT}$) in the interval $[0;\pi]$. The value of phase difference at the spontaneous PT-symmetric breaking point $\gamma = \gamma_{PT}$ can be calculated analytically and it is given by the expression:

$$\phi_{PT}(\mu) = \arccos\left(\frac{\sqrt{1-\sqrt{1-\mu^2}}}{\sqrt{1+\sqrt{1-\mu^2}}}\right) \tag{1.29}$$

We note that in the limit of $\mu \to 0$ we get $\phi_{PT} = \pi/2$, corresponding to a "circular" polarization of the eigenmode. The opposite limit of $\mu \to 1$ results to $\phi_{PT} = 0$ corresponding to "linear" polarization.

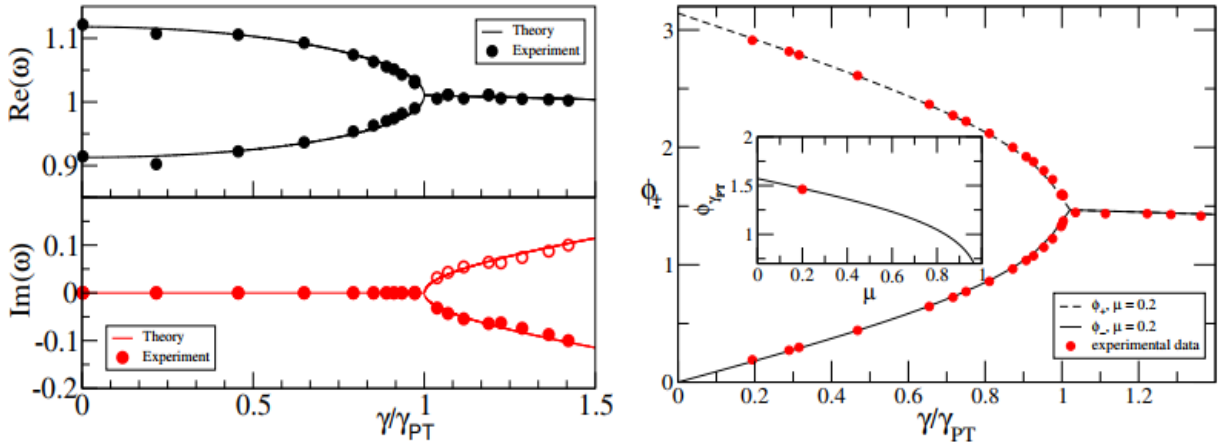

Figure 1.19: (Left) Parametric evolution of the experimentally measured eigenfrequencies, vs. the normalized gain/loss parameter $\gamma = \gamma_{PT}$. A comparison with the theoretical results of Eq.1.18, indicates an excellent agreement. In all cases, we show only the $\mathrm{Re}(\omega_l) > 0$ eigenfrequencies. The open circles in the lower panel are reflections of the experimental data (lower curve) with respect to the $\mathrm{Im}(\omega) = 0$ axis. (Right) Parametric evolution of the phase difference $\phi_{\pm}$. Symbols correspond to experimental data while the lines indicate the theoretical results of from Eq.1.24. The theoretical $\phi_{PT}(\mu)$ is shown in the inset. Figure is taken from ref. [131]

1.4.3.1 PT dimer dynamics

The signatures of PT -symmetry and the transition from the exact phase to the broken phase are similarly reflected in the temporal behavior of our system. Eq.1.24 can be solved either analytically or via direct numerical integration in order to obtain the temporal behavior of the capacitor charge $Q_n(\tau)$ and the displacement current $I_n(\tau)$ in each of the two circuits of the PT -symmetric dimer. As an example of the dimer state evolution, we consider an initial displacement current in one of the circuits with all other dynamical variables zero.

In Fig.1.20 we present some typical measurements for the temporal behavior of circuit voltages along with the corresponding numerical result. We consider a dimer configuration with $\mu = 0.2$ and $c = 0$ (i.e. inductive coupling only). In the left panel of Fig.1.20a, we show $V_1(\tau)$ and $V_2(\tau)$ for an initial condition having $I_1(0) = 1.2mA$ with all other dynamical variables zero. The right panel shows the same data as a Lissajiou plot, with the initial condition trajectory leaving the origin with V_1 decreasing, and V_2 stationary. Agreement between the experiment (circles) and the simulations (lines) is observed, illustrating that, in spite of the presence of dissipative elements and nonorthogonal states, the beat superposition associated with real frequencies occurs. There is, however, a subtle distinction: Since energy is not conserved, the beat is asymmetric between the gain side and the loss side nodal times, with oscillatory activity spending more time between gain side nodal points as energy grows to a significantly larger size before decaying and growing between the loss side nodal points. However, unlike traditional coupled-oscillator beats,

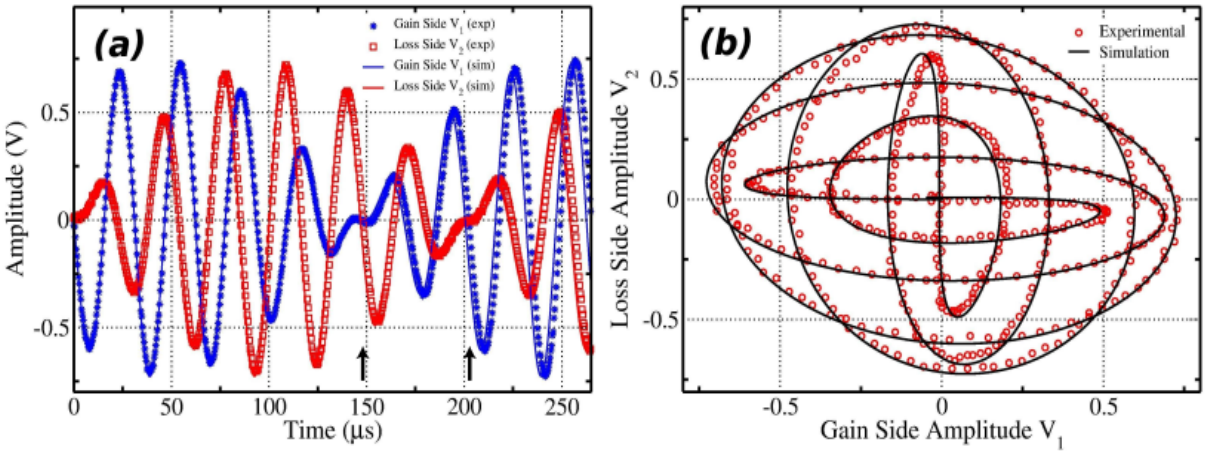

Figure 1.20: (a) Gain and loss side voltages vs. time compared to the simulation. (b) Gain vs. loss side Lissajous figure for one beat period. At $t = 0$ an initial current was imposed in the gain side inductor with all other dynamical variables zero. Note that the end of the beat (indicated by the arrow near $200\mu s$) is preceded by a similar point where both voltages pass through zero (indicated by the arrow near $150\mu s$) with V_2 decreasing, and V_1 stationary. This corresponds to the complementary initial condition starting from the loss side, and illustrates an asymmetric time between the beat nodal points of oscillatory activity in the two oscillators of the dimer. Figure is taken from ref. [131]

instead of "slashing" between both sides during the course of the beats, a growth and decay energy dance occurs with both sides more or less equally represented except in the vicinity of the nodal points. This behavior is a direct result of the non-orthogonal phase relationships that become more pronounced as $\gamma \to \gamma_{PT}$. A Hamiltonian dimer would exhibit a perfect half-beat offset between the left and right voltage beat envelopes.

1.5 Conclusion

In this chapter, we have done a review of the literature on the genesis of transfer, based on Tesla's work, as well as different modes of wireless transmission in some branches of physics. Since our work focuses on electronics, we presented an example of a study carried out by Alexandre Sample on an electrical circuit. In the second part of this chapter, we focused on the basics of PT-symmetric systems, as well as a study of the analysis of eigenfrequencies and circuit dynamics. In the next chapter, the electronic circuits that will be studied have the PTS characteristic compared with standard electronic circuit and then. After that, we will study wireless transmission inside these circuits.

Chapter 2

Methodology

2.1 Introduction

In the previous chapter, we have discussed about the generality of wireless transmission systems used to interconnect different devices. The investigation made on this chapter focuses on the mathematical modelling and simulations of wireless transmission in PT symmetry electronic systems. We start by recalling some fundamentals. The second section presents different models. After the description of the electronic cells coupling by mutual induction, the study gives different electronic circuits and presents the methods and analogical simulation used to obtain some results.

2.2 Description, modeling of different circuits

2.2.1 The RLC parallel oscillator

As the circuits we propose are essentially based on the known parallel RLC oscillators (Fig2.1) coupled together (dimer) or via neutral LC cells (trimer, quadrimer,...), it is appropriate to briefly highlight their characteristics. To obtain the characteristic equation and eigenmodes of this circuit, we can use the state variable method to obtain a system of first order differential equation governing the capacitor voltage and inductor current.

- **State variable analysis**

Let us establish the equation governing the dynamic of the circuit in Fig2.1. The voltage considered at the terminals of the circuit is the one delivered at the terminals of the capacitor.

Applying the KCL at the central node of this circuit, the following equation is obtained.

$$\frac{v_c}{R} + i_L + C\frac{dv_c}{dt} = 0 \tag{2.1}$$

Expressing $\frac{dv_c}{dt}$ in eq(2.1) gives:

$$\frac{dv_c}{dt} = -\frac{1}{CR}v_c - \frac{1}{C}i_L \tag{2.2}$$

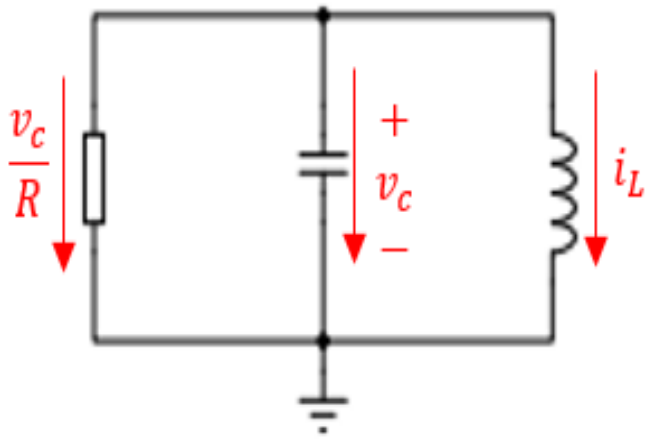

Figure 2.1: Normal tree of the source free RLC oscillator. Representation of the voltage across the capacitor and the current through the inductor and the resistor.

Now let's apply the KVL to express the inductor current as function of the capacitor voltage.

$$\frac{di_L}{dt} = \frac{1}{L} v_c \tag{2.3}$$

From eq.(2.2) and eq.(2.3), we obtain the following system of differential equation of first order.

$$\begin{cases} \frac{dv_c}{dt} = -\frac{1}{CR} v_c - \frac{1}{C} i_L \\ \frac{di_L}{dt} = \frac{1}{L} v_c \end{cases} \tag{2.4}$$

To obtain the characteristic equation, we express the eq.(2.4) using the matrix notation to obtain the Liouvilliam formalism as follow:

$$\frac{d\Psi}{dt} = M\Psi; \tag{2.5}$$

where $\Psi(t) = [v_c \ i_L]^T$ is the eigenvector and T denoted the transpose operator. The solutions of eq.(2.5)is assumed to be of the form $e^{\omega t}$. the eigenvalues is constructed as

$$(M - \omega I)\,\psi = 0; \tag{2.6}$$

where I is the 2×2 identity matrix, λ_k with $k = 1, 2$ are the eigenvalues of 2×2 matrix M that is given by

$$M = \begin{pmatrix} -\frac{1}{RC} & -\frac{1}{C} \\ \frac{1}{L} & 0 \end{pmatrix} \tag{2.7}$$

Solving eq.(2.6) we obtain the characteristic equation of eigenvalues as follows:

$$\omega^2 + \frac{1}{RC}\omega + \frac{1}{LC} = 0 \tag{2.8}$$

- **Anzat method analysis**

Let us consider the equations obtained in eq.(2.2) and eq.(2.3). We derive eq.(2.2) and obtain the follow equation.

$$\frac{d^2v_c}{dt^2} = -\frac{1}{CR}\frac{dv_c}{dt} - \frac{1}{C}\frac{di_L}{dt} \tag{2.9}$$

Eq.(2.3) into eq.(2.9), we obtain de final second order differential equation describing the dynamic of the parallel RLC cell as

$$\frac{d^2v_c}{dt^2} + \frac{1}{CR}\frac{dv_c}{dt} + \frac{1}{LC}v_c = 0 \tag{2.10}$$

The equation obtained is governed by the capacitor voltage of the circuit. it can be obtained also according to the charge $q(t)$ of the capacitor $v_c(t) = \frac{1}{C}q(t)$ then the following relation

$$\frac{d^2q}{dt^2} + \frac{1}{CR}\frac{dq}{dt} + \frac{1}{LC}q = 0 \tag{2.11}$$

or we use the current i_L and the voltage v_c across the inductor are linked by $v_c(t) = L\frac{di}{dt}$ into eq.(2.2). Hence, the circuit is governed by the following second order differential equation

$$\frac{d^2i_L}{dt^2} + \frac{1}{CR}\frac{di_L}{dt} + \frac{1}{LC}i_L = 0 \tag{2.12}$$

Considering that the voltage of eq.(2.10), the charge of eq.(2.11) or the current of eq.(2.12) oscillate according to $v_c = V_0e^{j\omega t}$, $q = Q_0e^{j\omega t}$ and $i_L = I_0e^{j\omega t}$ respectively, we find the same characteristic equation obtained in eq.(2.8).

In the frequency domain, we assume $\tau = \omega_0 t$ where $\omega_0^2 LC = 1$. eq.(2.10), eq.(2.11) and eq.(2.12) become

$$\frac{d^2v_c}{d\tau^2} + \gamma\frac{dv_c}{d\tau} + v_c = 0; \tag{2.13}$$

$$\frac{d^2q}{d\tau^2} + \gamma\frac{dq}{d\tau} + q = 0 \tag{2.14}$$

and

$$\frac{d^2i_L}{d\tau^2} + \gamma\frac{di_L}{d\tau} + i_L = 0 \tag{2.15}$$

where $\gamma = \frac{1}{R}\sqrt{\frac{L}{C}}$ and these equations oscillate according to $v_c = V_0e^{j\omega t}$, $q = Q_0e^{j\omega t}$ and $i_L = I_0e^{j\omega t}$ respectively with $j^2 = -1$.

2.2.2 RLC Dimer

The RLC dimer presented in figure 2.2 consists of two RLC osillators (Fig**??**) coupling by mutual induction between the two coils of cells. The first cell is made of a negative resistance $(-R)$ and generates amplified oscillations (Gain cell) while the second one is made of a positive resistance and generates attenuated oscillations (loss cell). This amplification and attenuation allows the compensation of the oscillations of circuit and

gives it the configuration of a PTS system.

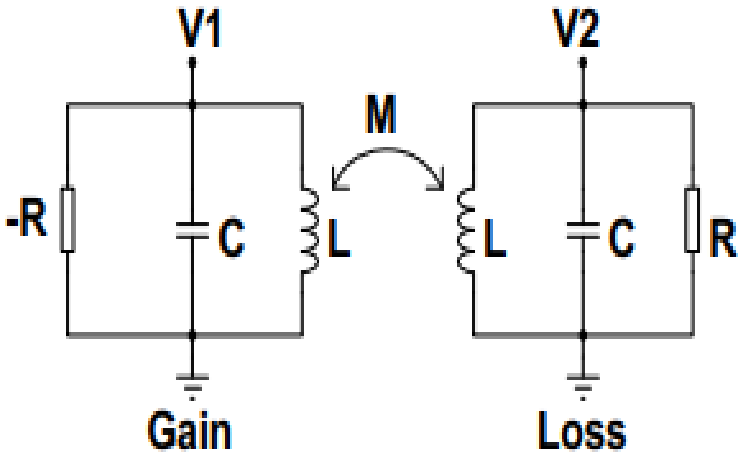

Figure 2.2: Electronic circuit of parallel RLC dimer: The two cells are coupled by mutual induction between the two coils.

Applying the KCL and KVL of each cell, we obtain the systems of equations as follows

$$\begin{cases} I^1_{-R} + I^1_C + I^1_L = 0 \\ I^2_R + I^2_C + I^2_L = 0 \end{cases} \tag{2.16}$$

$$\begin{cases} v_1 = L\frac{dI^1_L}{dt} + M\frac{dI^2_L}{dt} \\ v_2 = M\frac{dI^1_L}{dt} + L\frac{dI^2_L}{dt} \end{cases} \tag{2.17}$$

where $I^i_R = (-1)^i \frac{v_i}{R}$; $I^i_C = C\frac{dv_i}{dt}$; $i = 1, 2$.

Deriving eq.(2.16) with respect to time taking into account eq.(2.17), the system of coupled equations that describes the dynamic of circuit is given as

$$\begin{cases} \frac{d^2v_1}{dt^2} - \frac{1}{CR}\frac{dv_1}{dt} + \frac{1}{C}\left(\frac{L}{L^2-M^2}\right) v_1 - \frac{1}{C}\left(\frac{M}{L^2-M^2}\right) v_2 = 0 \\ \frac{1}{CR}\frac{dv_2}{dt} + \frac{d^2v_2}{dt^2} - \frac{1}{C}\left(\frac{M}{L^2-M^2}\right) v_1 + \frac{1}{C}\left(\frac{L}{L^2-M^2}\right) v_2 = 0 \end{cases} \tag{2.18}$$

To work in the frequency domain, the transition from the time space to the frequency space is done via the relation $\tau = \omega_0 t$; Then eq.(2.18) becomes

$$\begin{cases} \frac{d^2v_1}{d\tau^2} - \gamma\frac{dv_1}{d\tau} + \alpha v_1 - \alpha\mu v_2 = 0 \\ \gamma\frac{dv_2}{d\tau} + \frac{d^2v_2}{d\tau^2} - \alpha\mu v_1 + \alpha v_2 = 0 \end{cases} \tag{2.19}$$

where $\gamma = \frac{1}{R}\sqrt{\frac{L}{C}}$; $\mu = \frac{M}{L}$; $\alpha = \frac{1}{1-\mu^2}$

2.2.3 RLC Trimer

The RLC trimer shown in fig2.3 is consisted of three RLC oscillators. The gain cell with an amplification is generated by a negative resistance $(-R)$, and the loss cell with an attenuation is introduced by a positive resistance (R). An oscillator consisting of inductor

L and capacitor C (LC oscillator) is placed between the gain cell and the loss cell. This LC oscillator is also called a neutral cell or a conservative cell. The three cells are coupled by mutual induction between the coils. in order words, The RLC trimer is built by inserting one conservative cell inside the RLC dimer. It should be noted here that we only consider the coupling between neighboring cells of first rank. Applying KCL and KVL on this

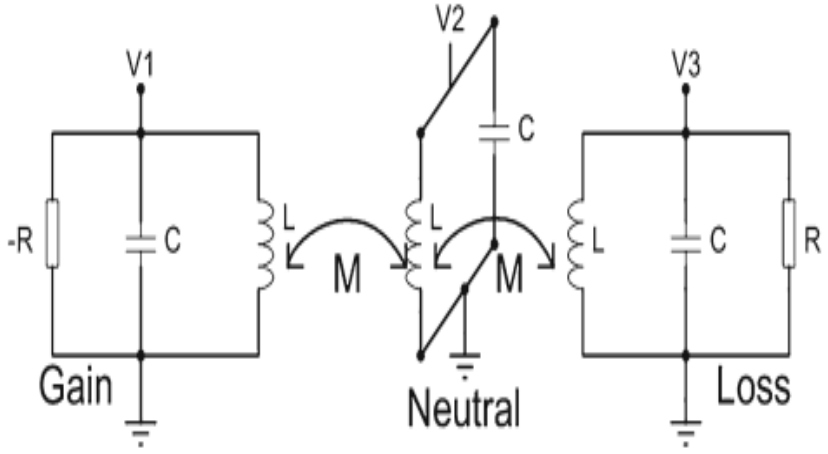

Figure 2.3: Electronic circuit of parallel RLC trimer: Each cell is coupled by mutual induction by the nearest neighboring cell.

circuit, we obtain the following equations

$$\begin{cases} I^1_{-R} + I^1_C + I^1_L = 0 \\ I^3_R + I^3_C + I^3_L = 0 \end{cases} \tag{2.20}$$

$$\begin{cases} v_1 = L\frac{dI^1_L}{dt} + M\frac{dI^2_L}{dt} \\ v_2 = M\frac{dI^1_L}{dt} + L\frac{dI^2_L}{dt} + M\frac{dI^3_L}{dt} \\ v_3 = M\frac{dI^2_L}{dt} + L\frac{dI^3_L}{dt} \end{cases} \tag{2.21}$$

In the neutral cell, we have

$$u_C + u_L = 0 \tag{2.22}$$

where $I^1_{-R} = -\frac{v_1}{R}$; $I^3_R = \frac{v_3}{R}$; $I^i_C = C\frac{dv_i}{dt}$; $(i = 1, 2, 3)$.

By combining eq.(2.20), eq.(2.21) and eq.(2.22) as in the previous case of RLC dimer, we obtain the following system of coupled second order differential equations describing the dynamic of the voltage circuit in the frequency domain.

$$\begin{cases} \frac{d^2v_1}{d\tau^2} - \gamma\frac{dv_1}{d\tau} + (1-\mu^2)\,\varepsilon v_1 - \mu\varepsilon v_2 + \mu^2\varepsilon v_3 = 0 \\ \frac{d^2v_2}{d\tau^2} - \mu\varepsilon v_1 + \varepsilon v_2 - \mu\varepsilon v_3 = 0 \\ \frac{d^2v_3}{d\tau^2} + \gamma\frac{dv_3}{d\tau} + \mu^2\varepsilon v_1 - \mu\varepsilon v_2 + (1-\mu^2)\,\varepsilon v_3 = 0 \end{cases} \tag{2.23}$$

where $\gamma = \frac{1}{R}\sqrt{\frac{L}{C}}$; $\mu = \frac{M}{L}$; $\varepsilon = \frac{1}{1-2\mu^2}$

2.2.4 RLC Quadrimer

Let us analyse the circuit having four cells. This circuit is based on the RLC dimer where two neutral cells are inserted between the gain and the loss cell. We also take into account the coupling between the first nearest neighboring cells. The circuit that illustrates this model is presented in figure 2.4 The KCL and KVL give for this circuit

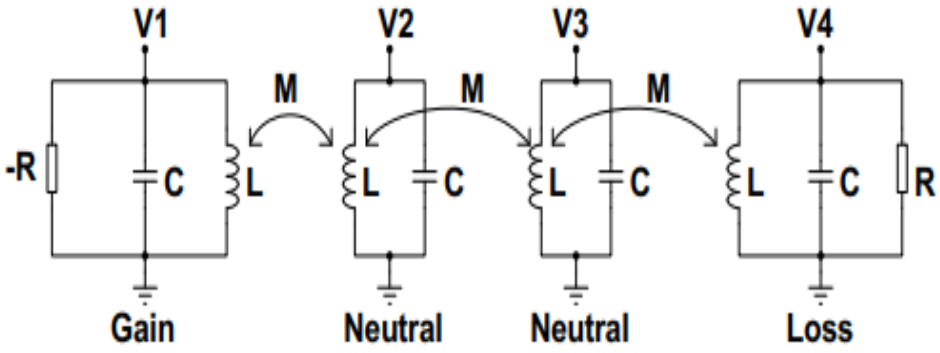

Figure 2.4: Electronic circuit of parallel RLC quadrimer: Each cell is coupled by mutual induction by the nearest neighboring cell.

the following equations.

$$\begin{cases} I^1_{-R} + I^1_C + I^1_L = 0 \\ I^4_R + I^4_C + I^4_L = 0 \end{cases} \tag{2.24}$$

$$\begin{cases} v_1 = L\frac{dI^1_L}{dt} + M\frac{dI^2_L}{dt} \\ v_2 = M\frac{dI^1_L}{dt} + L\frac{dI^2_L}{dt} + M\frac{dI^3_L}{dt} \\ v_3 = M\frac{dI^2_L}{dt} + L\frac{dI^3_L}{dt} + M\frac{dI^4_L}{dt} \\ v_3 = M\frac{dI^3_L}{dt} + L\frac{dI^4_L}{dt} \end{cases} \tag{2.25}$$

In each neutral cell, we have

$$u_C + u_L = 0 \tag{2.26}$$

where $I^1_{-R} = -\frac{v_1}{R}$; $I^4_R = \frac{v_4}{R}$; $I^i_C = C\frac{dv_i}{dt}$; $(i = 1, ..., 4)$.

Analyzing eq.(2.25), the extraction of the terms of different currents gives voluminous expressions. In order to have easy to handle equations, the establishment of the differential equations governing the circuit is better in inductor current than in capacitor voltage. Let i_1, i_2, i_3 and i_4 the inductor current in the four cells respectively, we derive eq.(2.26) with respect to time so, eq.(2.24) and eq.(2.26) give

$$\begin{cases} C\frac{dv_1}{dt} - \frac{v_1}{R} + i_1 = 0 \\ \frac{dv_2}{dt} + \frac{1}{C}i_2 = 0 \\ \frac{dv_3}{dt} + \frac{1}{C}i_3 = 0 \\ C\frac{dv_4}{dt} + \frac{v_4}{R} + i_4 = 0 \end{cases} \tag{2.27}$$

By inserting the different voltages of eq.(2.25) in the eq.(2.27), the differential equation system of the RLC quadrimer is given by the following equation

$$\begin{cases} \frac{d^2i_1}{dt^2} + \mu\frac{d^2i_2}{dt^2} - \frac{1}{RC}\frac{di_1}{dt} - \frac{\mu}{RC}\frac{di_2}{dt} + \frac{1}{LC}i_1 = 0 \\ \mu\frac{d^2i_1}{dt^2} + \frac{d^2i_2}{dt^2} + \mu\frac{d^2i_3}{dt^2} + \frac{1}{LC}i_2 = 0 \\ \mu\frac{d^2i_2}{dt^2} + \frac{d^2i_3}{dt^2} + \mu\frac{d^2i_4}{dt^2} + \frac{1}{LC}i_3 = 0 \\ \mu\frac{d^2i_3}{dt^2} + \frac{d^2i_4}{dt^2} + \frac{\mu}{RC}\frac{di_3}{dt} + \frac{1}{RC}\frac{di_4}{dt} + \frac{1}{LC}i_4 = 0 \end{cases} \tag{2.28}$$

where $\mu = \frac{M}{L}$. In the frequency domain according to $\tau = \omega_0 t$ with $\omega_0^2 LC = 1$, we have

$$\begin{cases} \frac{d^2i_1}{d\tau^2} + \mu\frac{d^2i_2}{d\tau^2} - \gamma\frac{di_1}{d\tau} - \mu\gamma\frac{di_2}{d\tau} + i_1 = 0 \\ \mu\frac{d^2i_1}{d\tau^2} + \frac{d^2i_2}{d\tau^2} + \mu\frac{d^2i_3}{d\tau^2} + i_2 = 0 \\ \mu\frac{d^2i_2}{d\tau^2} + \frac{d^2i_3}{d\tau^2} + \mu\frac{d^2i_4}{d\tau^2} + i_3 = 0 \\ \mu\frac{d^2i_3}{d\tau^2} + \frac{d^2i_4}{d\tau^2} + \mu\gamma\frac{di_3}{dt} + \gamma\frac{di_4}{dt} + i_4 = 0 \end{cases} \tag{2.29}$$

2.2.5 RLC n-mer

In the previous sections, we have presented the circuits of RLC dimer, RLC trimer and RLC quadrimer which are all parity time symmetric models. We notice that, by introducing the neutrals cells (RLC trimer and RLC quadrimer) between the gain cell and the loss cell, there is a balance of the gain and loss parameter. We propose a generalized model called $n - mer$ (n cells) including k ($k = 0...n-2$) conservatives cells between the gain cell and the loss cell. The model of this generalized circuit is presented in the following figure

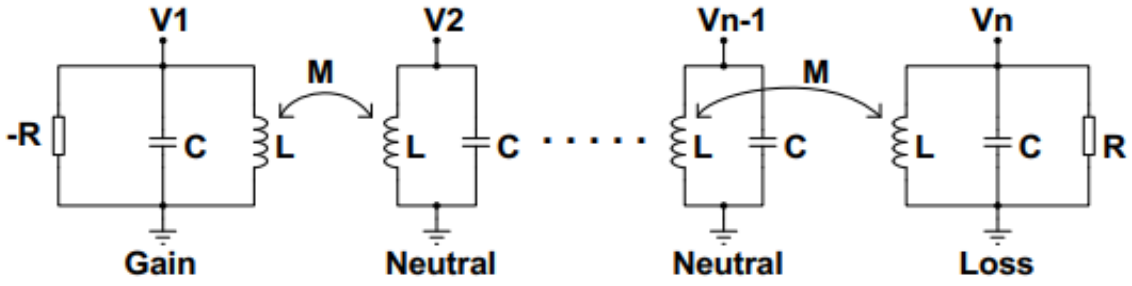

Figure 2.5: Electronic circuit of parallel RLC $n - mer$: Each cell is coupled by mutual induction by the nearest neighboring cell.

Some cases (ten first cases) are listed in the following table

The generalized circuit equation system is obtained by proceeding in the same way in the case of RLC quadrimer. We obtain n second order differential equations coupled by

Number of cells (n)	Number of neutral cells (k)	Name
2	0	RLC dimer
3	1	RLC trimer
4	2	RLC quadrimer
5	3	RLC pentamer
6	4	RLC hexamer
7	5	RLC heptamer
8	6	RLC octamer
9	7	RLC nonamer
10	8	RLC decamer

Table 2.1: Nomenclature of the first ten circuits with their number of cells and the number of conservatives cells to be inserted between the gain cell and loss cell to model them.

the mutual induction parameter μ as follows

$$\begin{cases} \frac{d^2}{d\tau^2}i_1(\tau) + \mu\frac{d^2}{d\tau^2}i_2(\tau) - \gamma\frac{d}{d\tau}i_1(\tau) - \mu\gamma\frac{d}{d\tau}i_2(\tau) + i_1(\tau) = 0 \\ . \\ . \\ \frac{d^2}{d\tau^2}i_j(\tau) + \mu\frac{d^2}{d\tau^2}i_{j-1}(\tau) + \mu\frac{d^2}{d\tau^2}i_{j+1}(\tau) + i_j(\tau) = 0 \\ . \\ . \\ \frac{d^2}{d\tau^2}i_n(\tau) + \mu\frac{d^2}{d\tau^2}i_{n-1}(\tau) + \gamma\frac{d}{d\tau}i_n(\tau) + \mu\gamma\frac{d}{d\tau}i_{n-1}(\tau) + i_n(\tau) = 0 \end{cases} \tag{2.30}$$

where $j = 2....n-1$; $\mu = \frac{M}{L}$; $\tau = \omega_0 t$; $\omega_0^2 LC = 1$ and $\gamma = \frac{1}{R}\sqrt{\frac{L}{C}}$.

2.3 Study of the eigenmodes of some models

In the previous section, we showed that by using Kirchhoff's laws, it can easily establish the various differential equations governing our different circuits. In this section, we present the eigenvalues of the first three circuits (RLC dimer, RLC trimer and RLC quadrimer) and the generalized eigenvalues matrix of $n-mer$ on the basic of the differential equations systems obtained previously. As these systems are non-Hermitian, two resoltion methods are use to obtain the eigenvalues of each model. The first is to consider that the variable of differential equations oscillates according to $x(\tau) = X_0 e^{j\omega\tau}$ where $x(\tau)$ is the dimensionless voltage capacitor $v(\tau)$, inductor current $i(\tau)$ or charge of capacitor $q(\tau)$. The second method is to put the system of differential equations into the form of the Schrödinger equation in order to obtain the $\mathcal{H}$ non-Hermitian Hamiltonian matrix. Then, the eigenvalues are obtained by solving the following equation:

$$(\mathcal{H} - \omega I) = 0 \tag{2.31}$$

Both methods lead to the same result.

2.3.1 RLC Dimer

The system governing the RLC dimer given in eq.(2.19) takes the following form according to the Liouvillian formalism:

$$\frac{d\Psi}{d\tau} = \mathcal{L}\Psi, \qquad \mathcal{L} = \begin{pmatrix} 0 & 0 & 1 & 0 \\ 0 & 0 & 0 & 1 \\ -\alpha & \alpha\mu & \gamma & 0 \\ \alpha\mu & -\alpha & 0 & -\gamma \end{pmatrix} \tag{2.32}$$

where $\Psi \equiv \begin{pmatrix} v_1 & v_2 & \dot{v}_1 & \dot{v}_2 \end{pmatrix}^T$, v_k and $\dot{v}_k$ correspond to the voltage across the capacitor and the current flowing through it per capacitive unit in the kth oscillator (the subscripts 1, 2 denote the gain cell and loss cell respectively), $\tau = \omega_0 t$, the gain-loss parameter(or non-Hermiticity) $\gamma = R^{-1}\sqrt{LC^{-1}}$, the coupling strength characterized by the rescaled mutual inductance $\mu = ML^{-1}$, $\omega_0 = (LC)^{-1}$, and all (angular) frequencies are measured in units of ω_0. The effective Hamiltonian can be written as $H_eff = i\mathcal{L}(H_{eff}\Psi = i\partial_\tau\Psi)$, which is non-Hermitian ($H^\dagger_{eff} \neq H_{eff}$) and symmetric with respect to the PT transformation, namely $[\mathcal{PT}, H_{eff}] = 0$, with

$$\mathcal{P} = \begin{pmatrix} \sigma_{\mathbf{x}} & 0 \\ 0 & \sigma_{\mathbf{x}} \end{pmatrix} \quad and \quad \mathcal{T} = \begin{pmatrix} \mathbf{I} & 0 \\ 0 & -\mathbf{I} \end{pmatrix} k \tag{2.33}$$

where $\sigma_x = \begin{pmatrix} 0 & 1 \\ 1 & 0 \end{pmatrix}$ and k conducts the operation of complex conjugation. These operations in conjunction leave the system unaltered. The system has four eigenvalues or eigenfrequencies, which can be derived from the secular equation as

$$\omega_{1,2} = \pm\frac{\sqrt{2}}{2}\frac{\sqrt{(\mu^2-1)\left(-\eta^2\mu^2+\eta^2-2+\sqrt{\eta^4\mu^4-2\,\eta^4\mu^2+\eta^4+4\,\eta^2\mu^2-4\,\eta^2+4\,\mu^2}\right)}}{\mu^2-1} \tag{2.34}$$

$$\omega_{3,4} = \pm\frac{1}{2}\frac{\sqrt{-(2\,\mu^2-2)\left(\eta^2\mu^2-\eta^2+\sqrt{\eta^4\mu^4-2\,\eta^4\mu^2+\eta^4+4\,\eta^2\mu^2-4\,\eta^2+4\,\mu^2}+2\right)}}{\mu^2-1} \tag{2.35}$$

2.3.2 RLC Trimer

The RLC trimer is governed by the system of differential equations of eq.(2.23). The voltage capacitor of each cell oscillates according to $V_j = V_{0j}e^{i\omega\tau}$, inserting this equation, its eigenvalues matrix can be obtained as:

$$\begin{pmatrix} -\omega^2 - i\omega\gamma + 1 & -\mu\omega^2 - i\omega\mu\gamma & 0 \\ -\omega^2\mu & -\omega^2 + 1 & -\omega^2\mu \\ 0 & -\mu\omega^2 + i\omega\mu\gamma & -\omega^2 + i\omega\gamma + 1 \end{pmatrix} \tag{2.36}$$

and its characteristic equation is given by the following equation:

$$(2\mu^2 - 1)\omega^6 + (2\gamma^2\mu^2 - \gamma^2 - 2\mu^2 + 3)\omega^4 + (\gamma^2 - 3)\omega^2 + 1 = 0 \tag{2.37}$$

By solving this characteristic equation, we obtain six eigenvalues of the system given by:

$$\omega_{1,2} = \pm \begin{pmatrix} \frac{1}{6}\frac{(-108DA^2+36CBA+12A\sqrt{3}\sqrt{27A^2D^2-18ABCD+4AC^3+4B^3D-B^2C^2-8B^3})^{1/3}}{A} \\ -\frac{2}{3}\frac{3AC-B^2}{A(-108DA^2+36CBA+12A\sqrt{3}\sqrt{27A^2D^2-18ABCD+4AC^3+4B^3D-B^2C^2-8B^3})^{1/3}} - \frac{1}{3}\frac{B}{A} \end{pmatrix} \tag{2.38}$$

$$\omega_{3,4} = \pm \begin{pmatrix} -\frac{1}{12}\frac{(-108DA^2+36CBA+12A\sqrt{3}\sqrt{27A^2D^2-18ABCD+4AC^3+4B^3D-B^2C^2-8B^3})^{1/3}}{A} \\ -\frac{1}{3}\frac{3AC-B^2}{A(-108DA^2+36CBA+12A\sqrt{3}\sqrt{27A^2D^2-18ABCD+4AC^3+4B^3D-B^2C^2-8B^3})^{1/3}} - \frac{1}{3}\frac{B}{A} \\ +i\frac{1}{2}\sqrt{3}\begin{pmatrix} \frac{1}{6}\frac{(-108DA^2+36CBA+12A\sqrt{3}\sqrt{27A^2D^2-18ABCD+4AC^3+4B^3D-B^2C^2-8B^3})^{1/3}}{A} \\ +-\frac{2}{3}\frac{3AC-B^2}{A(-108DA^2+36CBA+12A\sqrt{3}\sqrt{27A^2D^2-18ABCD+4AC^3+4B^3D-B^2C^2-8B^3})^{1/3}} \end{pmatrix} \end{pmatrix} \tag{2.39}$$

$$\omega_{5,6} = \pm \begin{pmatrix} -\frac{1}{12}\frac{(-108DA^2+36CBA+12A\sqrt{3}\sqrt{27A^2D^2-18ABCD+4AC^3+4B^3D-B^2C^2-8B^3})^{1/3}}{A} \\ -\frac{1}{3}\frac{3AC-B^2}{A(-108DA^2+36CBA+12A\sqrt{3}\sqrt{27A^2D^2-18ABCD+4AC^3+4B^3D-B^2C^2-8B^3})^{1/3}} - \frac{1}{3}\frac{B}{A} \\ -i\frac{1}{2}\sqrt{3}\begin{pmatrix} \frac{1}{6}\frac{(-108DA^2+36CBA+12A\sqrt{3}\sqrt{27A^2D^2-18ABCD+4AC^3+4B^3D-B^2C^2-8B^3})^{1/3}}{A} \\ +-\frac{2}{3}\frac{3AC-B^2}{A(-108DA^2+36CBA+12A\sqrt{3}\sqrt{27A^2D^2-18ABCD+4AC^3+4B^3D-B^2C^2-8B^3})^{1/3}} \end{pmatrix} \end{pmatrix} \tag{2.40}$$

where $A = (2\mu^2 - 1)$; $B = ((2\mu^2 - 1)\gamma^2 - 2\mu^2 + 3)$; $C = (\gamma^2 - 3)$ and $D = 1$ are coefficients of eq.(2.38), eq.(2.39) and eq.(2.40)

2.3.3 RLC Quadrimer

The RLC quadrimer is governed by the system of current differential equations given in eq.(2.29). The current inductor of each cell oscillates according to $i_k = I_{0k}e^{j\omega\tau}$ where $j^2 = -1$ is the complex number and $k = 1, 2, 3, 4$. This gives the following 4×4 eigenvalue matrix.

$$\begin{pmatrix} -\omega^2 - i\omega\gamma + 1 & -\mu\omega^2 - i\omega\mu\gamma & 0 & 0 \\ -\omega^2\mu & -\omega^2 + 1 & -\omega^2\mu & 0 \\ 0 & -\omega^2\mu & -\omega^2 + 1 & -\omega^2\mu \\ 0 & 0 & -\mu\omega^2 + i\omega\mu\gamma & -\omega^2 + i\omega\gamma + 1 \end{pmatrix} \tag{2.41}$$

The determinant of this matrix leads to the following characteristic equation:

$$\begin{aligned} &(\mu^4 - 3\mu^2 + 1)\,\omega^8 + (\gamma^2\,(\mu^4 - 3\mu^2 + 1) + 6\mu^2 - 4)\,\omega^6 \\ &+ (2\gamma^2\,(\mu^2 - 1) - 3\mu^2 + 6)\,\omega^4 + (\gamma^2 - 4)\,\omega^2 + 1 = 0 \end{aligned} \tag{2.42}$$

This characteristic equation has 8 solutions representing the eigenvalues of the quadrimer circuit.

2.3.4 RLC n-mer

The equation governing the RLC $n - mer$ circuit is given by eq.(2.30). The general eigenvalue matrix after using the ansatz $i_k = I_{0k}e^{j\omega\tau}$ is given by the following equation:

$$M = \begin{pmatrix} -\omega^2 - i\omega\gamma + 1 & -\mu\omega^2 - i\omega\mu\gamma & 0 & . & . & 0 \\ -\omega^2\mu & -\omega^2 + 1 & -\omega^2\mu & . & . & . \\ 0 & . & . & . & . & . \\ . & . & . & . & . & 0 \\ . & . & . & -\omega^2\mu & -\omega^2 + 1 & -\omega^2\mu \\ 0 & . & . & 0 & -\mu\omega^2 + i\omega\mu\gamma & -\omega^2 + i\omega\gamma + 1 \end{pmatrix} \tag{2.43}$$

This matrix generates all the cases of different circuits from the RLC dimer to circuits with n neutral cells. The degree of the characteristic polynomial of this matrix is $2n$. Given that the degree of this polynomial becomes increasingly important from the RLC

pentamer (n=5) onwards, analytical resolution becomes tedious. For this reason, the eigenvalues are obtained numerically by using matlab and Runge kutta method. For each case, we obtain $2n$ eigenvalues.

2.4 Wireless Power Transfer analysis

2.4.1 Wireless power transfer formalism

The wireless power transfer is supported by an electromagnetic wave travelling from the power emitter to the power receiver. In WPT systems, the electromagnetic field is exclusively generated to transfer power. Conversely, energy harvesting techniques make use of the electromagnetic waves generated to transfer information to acquire energy to power devices. Thus, energy harvesting techniques are restricted to the requirements imposed by the information transfer, which are not present in WPT technologies. Figure 2.6 illustrates the generic diagram of a WPT system.

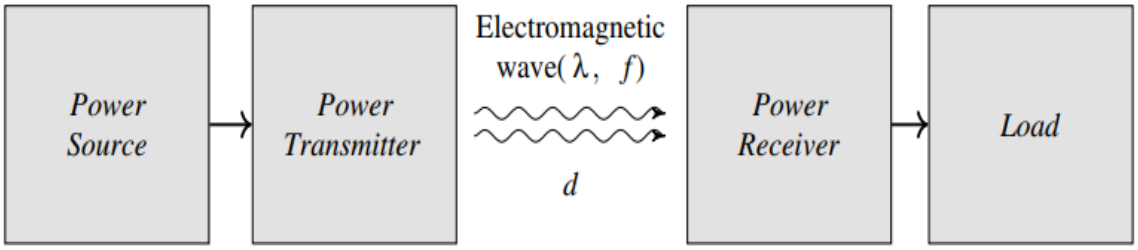

Figure 2.6: Generic diagram of a Wireless power transfer system.

The transmitter and the receiver are separated a distance d, usually referred to as the gap. Electromagnetic waves are characterized by their wavelength λ or their frequency f . The core part of an inductive WPT system is the magnetically coupled windings, which can be modeled with two coupled inductors, as shown in Fig.2.7 where V_S, V_L, R_S and R_L are the voltage source, the voltage load, the resistor in series with the source and the charge respectively.

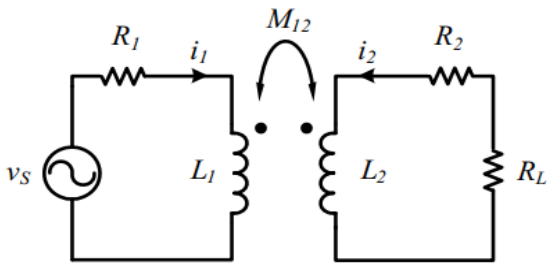

Figure 2.7: The coupled inductors.

The corresponding circuit equations are given by:

$$V_S = (R_1 + j\omega L_1)i_1 + j\omega M_{12} i_2 \tag{2.44}$$

$$j\omega M_{12} i_1 + (R_2 + R_L + j\omega L_2)i_2 = 0 \tag{2.45}$$

$$V_L = R_L i_2 \tag{2.46}$$

Combining eq.(2.44), eq.(2.45) and eq.(2.46),the transfer function is obtained by evaluating V_L/V_S given by the following equation:

$$\frac{V_L}{V_S} = \frac{jR_L\omega M_{12}}{L_1L_2\omega^2 - jL_1R_2\omega - jL_1R_L\omega - jL_2R_1\omega - M_{12}^2\omega^2 - R_1R_2 - R_1R_L} \tag{2.47}$$

For consistency, power transfer will be represented in terms of linear magnitude scattering parameters(S parameter) ($|S_{21}|$), which is important experimentally since it can be measured with a vector network analyser (VNA) for later comparison. The entire wireless power-transfer apparatus can be viewed as a two-port network (one port being the input, fed by the source, and the other being the output, feeding the load). One can calculate the equivalent S_{21} scattering parameter by:

$$S_{21} = 2\frac{V_{Load}}{V_{Source}}\left(\frac{R_{Source}}{R_{Load}}\right)^{\frac{1}{2}} \tag{2.48}$$

We then apply the same approach to evaluate the S parameter of our different circuits. The voltage source V_S is connected in series with resistor R_S on the gain cell, and the load R_L is connected to the loss cell.

2.4.2 RLC Dimer

The circuit diagram showing wireless power transfer in the RLC dimer is given below:

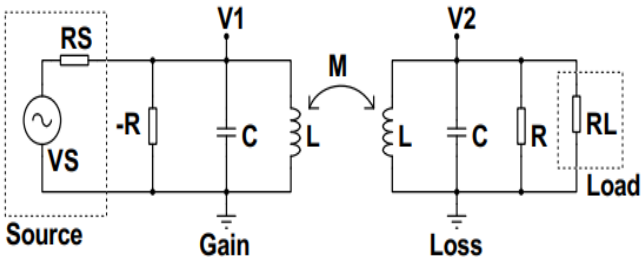

Figure 2.8: Electronic circuit for wireless power transfer in the RLC dimer.

Applying KLV and KCV to Fig.2.8, the following equations are obtained:

$$\begin{cases} \frac{V_1 - V_S}{R_S} + Y_1 V_1 + i_1 = 0 \\ V_1 = Z_l i_1 + j\omega M_{12} i_2 \\ V_2 = Z_l i_2 + j\omega M_{12} i_1 \\ Y_2 V_2 + i_2 = 0 \end{cases} ; \quad \begin{cases} Z_l = jL\omega \\ Z_c = \frac{1}{jC\omega} \\ Y_1 = \frac{1}{Z_c} - \frac{1}{R} \\ Y_2 = \frac{1}{R} + \frac{1}{Z_c} + \frac{1}{R_l} \\ R_L = R_{Load} \\ R_S = R_{Source} \end{cases} \tag{2.49}$$

Combining the equations of eq.(2.49) leads to the following transfer function:

$$\frac{V_L}{V_S} = \frac{i\,\omega\,M_{12}}{{M_{12}}^2 R_s\,Y_1\,Y_2\,\omega^2 + {M_{12}}^2 Y_2\,\omega^2 + R_s\,Y_1\,Y_2\,{Z_l}^2 + R_s\,Y_1\,Z_l + R_s\,Y_2\,Z_l + Y_2\,{Z_l}^2 + R_s + Z_l} \tag{2.50}$$

The mutual induction coupling between coils L_x and L_y is given by $k_{xy} = \frac{M_{xy}}{\sqrt{L_x L_y}}$; $x, y = 1, 2$. By replacing in eq.(2.50), the transfer function becomes:

$$\frac{V_L}{V_S} = \frac{j\omega k_{12}\sqrt{L_1 L_2}}{\left(\begin{array}{l} L_1 L_2 R_s Y_1 Y_2 {k_{12}}^2 \omega^2 + L_1 L_2 Y_2 {k_{12}}^2 \omega^2 + R_s Y_1 Y_2 {Z_l}^2 \\ + R_s Y_1 Z_l + R_s Y_2 Z_l + Y_2 {Z_l}^2 + R_s + Z_l \end{array} \right)} \tag{2.51}$$

2.4.3 RLC Trimer

The circuit diagram showing wireless power transfer in the RLC trimer is given below: Using KLV and KCV on Fig.2.9, the following equations are obtained:

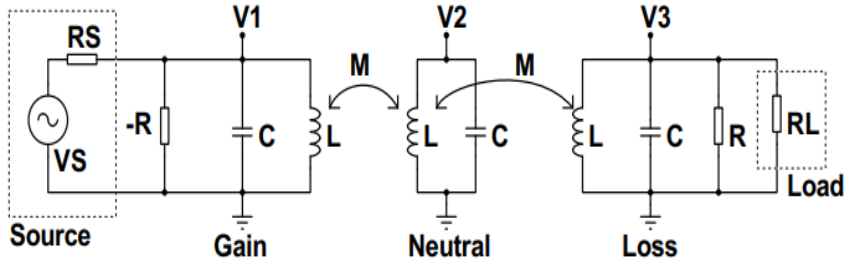

Figure 2.9: Electronic circuit for wireless power transfer in the RLC trimer.

$$\begin{cases} \frac{V_1 - V_s}{R_s} + Y_1 V_1 + i_1 = 0 \\ V_1 = Z_l i_1 + j\omega M_{12} i_2 \\ Z_e i_2 + j\omega M_{12} i_1 + j\omega M_{23} i_3 = 0 \\ V_3 = Z_l i_3 + j\omega M_{23} i_2 \\ Y_2 V_3 + i_3 = 0 \end{cases} \tag{2.52}$$

with

$$k_{xy} = \frac{M_{xy}}{\sqrt{L_x L_y}}, \ x, y = 1, 2 \, or \, 3 \tag{2.53}$$

By introducing eq.(2.53) into eq.(2.52) and combining them, we obtain the transfer function of eq.(2.54) giving the relationship between the signal on the receiver and the source.

$$\frac{V_l}{V_s} = \frac{\omega^2 k_{12} k_{23} L_2 \sqrt{L_1 L_3}}{\left(\begin{array}{l} L_1 L_2 R_s Y_1 Y_2 Z_l {k_{12}}^2 \omega^2 + L_2 L_3 R_s Y_1 Y_2 Z_l {k_{23}}^2 \omega^2 + L_1 L_2 R_s Y_1 {k_{12}}^2 \omega^2 \\ + L_1 L_2 Y_2 Z_l {k_{12}}^2 \omega^2 + L_2 L_3 R_s Y_2 {k_{23}}^2 \omega^2 + L_2 L_3 Y_2 Z_l {k_{23}}^2 \omega^2 + L_1 L_2 {k_{12}}^2 \omega^2 \\ + R_s Y_1 Y_2 Z_e {Z_l}^2 + R_s Y_1 Z_e Z_l + R_s Y_2 Z_e Z_l + Y_2 Z_e {Z_l}^2 + R_s Z_e + Z_e Z_l \end{array} \right)} \tag{2.54}$$

where

$$\begin{cases} Z_l = jL\omega \\ Z_c = \frac{1}{jC\omega} \\ Z_e = Z_l + Z_c \\ Y_1 = \frac{1}{Z_c} - \frac{1}{R} \\ Y_2 = \frac{1}{R} + \frac{1}{Z_c} + \frac{1}{R_l} \end{cases} \tag{2.55}$$

2.4.4 RLC Quadrimer

The diagram of wireless power transfer in the RLC quadrimer is shown in the following figure. Applying Kirchhoff's laws to this circuit gives the following equations:

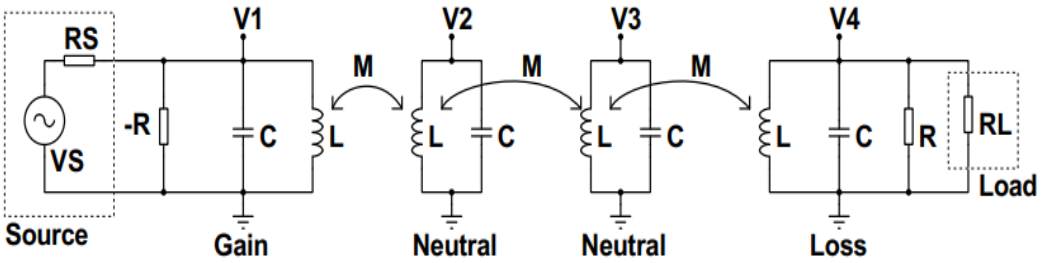

Figure 2.10: Electronic circuit for wireless power transfer in the RLC quadrimer.

$$\begin{cases} \frac{V_1 - V_s}{R_s} + Y_1 V_1 + i_1 = 0 \\ V_1 = Z_l i_1 + j\omega M_{12} i_2 \\ Z_e i_2 + j\omega M_{12} i_1 + j\omega M_{23} i_3 = 0 \\ Z_e i_3 + j\omega M_{23} i_2 + j\omega M_{34} i_4 = 0 \\ V_4 = Z_l i_4 + j\omega M_{34} i_3 \\ Y_2 V_4 + i_4 = 0 \end{cases} \tag{2.56}$$

with

$$k_{xy} = \frac{M_{xy}}{\sqrt{L_x L_y}}, \; x, y = 1, 2, 3 \, or \, 4 \tag{2.57}$$

By combinige eq.(2.56) and eq.(2.57), the tranfer function of RLC quadrimer is as follows:

$$\frac{V_l}{V_s} = \frac{-j\,\omega^3 k_{12}\sqrt{L_1 L_2}k_{23}\sqrt{L_2 L_3}k_{34}\sqrt{L_3 L_4}}{\left(\begin{array}{l}(L_1 L_2 L_3 L_4 R_s Y_1 Y_2 {k_{12}}^2 {k_{34}}^2 + L_1 L_2 L_3 L_4 Y_2 {k_{12}}^2 {k_{34}}^2)\omega^4 \\ +(+L_1 L_2 R_s Y_1 Y_2 Z e Z_l {k_{12}}^2 + L_2 L_3 R_s Y_1 Y_2 {Z_l}^2 {k_{23}}^2 + L_3 L_4 R_s Y_1 Y_2 Z e Z_l {k_{34}}^2 \\ +L_1 L_2 R_s Y_1 Z e {k_{12}}^2 + L_1 L_2 Y_2 Z e Z_l {k_{12}}^2 + L_2 L_3 R_s Y_1 Z_l {k_{23}}^2 \\ +L_2 L_3 R_s Y_2 Z_l {k_{23}}^2 + L_2 L_3 Y_2 {Z_l}^2 {k_{23}}^2 + L_3 L_4 R_s Y_2 Z e {k_{34}}^2 + L_3 L_4 Y_2 Z e Z_l {k_{34}}^2 \\ +L_1 L_2 Z e {k_{12}}^2 + L_2 L_3 R_s {k_{23}}^2 + L_2 L_3 Z_l {k_{23}}^2)\omega^2 + R_s Y_1 Y_2 Z e^2 {Z_l}^2 \\ +R_s Y_1 Z e^2 Z_l + R_s Y_2 Z e^2 Z_l + Y_2 Z e^2 {Z_l}^2 + R_s Z e^2 + Z e^2 Z_l\end{array}\right)} \tag{2.58}$$

2.4.5 RLC n-mer

In the preceding sections, we described the transfer function of the RLC dimer, trimer and quadrimer. the généralization of these circuits to order n is shown in the figure below. The Kirchhoff's laws applied to this circuit lea to the following equations:

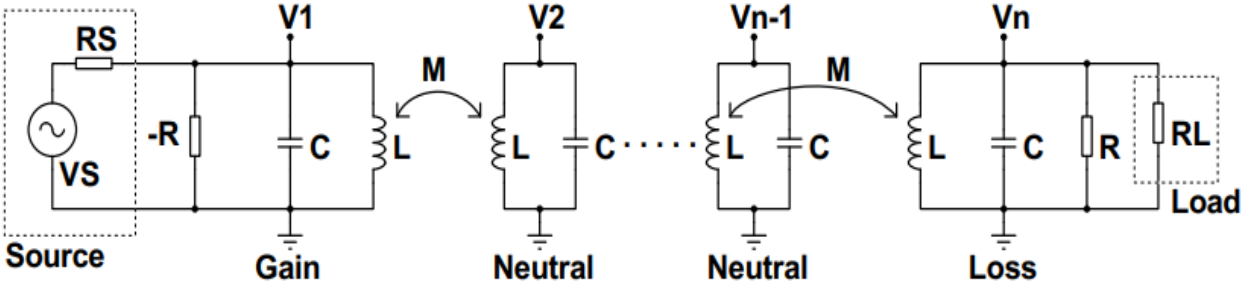

Figure 2.11: Electronic circuit for wireless power transfer in the RLC $n-mer$.

$$\begin{cases} \frac{V_1 - V_S}{R_S} - Y_1 V_1 + i_1 = 0 \\ V_1 = Z_l i_1 + j\omega M_{12} i_2 \\ . \\ . \\ Z_e i_k + j\omega M_{k-1,k} i_{k-1} + j\omega M_{k,k+1} i_{k+1} = 0 \\ . \\ . \\ V_n = Z_l i_n + j\omega M_{n-1,n} i_{n-1} \\ Y_2 V_n + i_n = 0 \end{cases} \tag{2.59}$$

with $k = 2....n-1$ and

$$\begin{cases} Z_l = jL\omega \\ Z_c = \frac{1}{jC\omega} \\ Z_e = Z_l + Z_c \\ Y_1 = \frac{1}{Z_c} \\ Y_2 = \frac{1}{R} + \frac{1}{Z_c} + \frac{1}{R_l} \\ R_L = R_{Load} \\ R_S = R_{Source} \end{cases} \tag{2.60}$$

In the same way, we can easily determine the transfer function of the circuit as a function of the number of neutral cells.

2.5 Numerical method

Analytical solving methods provide qualitative solutions to equations. As the complexity of these equations increases, it becomes difficult to obtain solutions analytically. Numerical methods are then used. In this thesis, we have used two numerical resolution methods:

- The root method for solving higher-degree characteristic equations.
- To study the dynamic evolution of our circuits, we used the Runge Kutta 4th-order algorithm

Thus, to plot analytical and numerical solutions, different syntaxes predefined in Matlab (version 2016: R2016b(9.1.0.441655)) or Maple (version 18.00) source programs and subroutines have been used on HP ProBook(Intel core i5; 2.40 GHz; RAM: 6 GHz; Windows 64 bits).

2.6 Analogical simulation

As our work is based on electronic circuits, an experimental study is necessary in order to compare the analytical and numerical results with the experimental results of the circuits

developed. As we did not have sufficient resources to carry out an experimental study, we limited ourselves to analogical simulations. In this thesis, the electronic simulation method used is based on the LTspice XVII software, in which we designed our various circuits.

LTspice® is a powerful, fast, and free SPICE simulator software, schematic capture and waveform viewer with enhancements and models for improving the simulation of analog circuits. Its graphical schematic capture interface allows you to probe schematics and produce simulation results, which can be explored further through the built-in waveform viewer.

2.7 Conclusion

In this chapter, we have presented the fundamental formulas for studying electronic circuits; then the different models and the equations governing their dynamics have been established. Analytical methods have enabled us to present the eigenvalues of our various non-Hermitian systems. As our work is focused on the study of wireless power transmission, we carried out a study to determine the transfer function of our different circuits. We conclude with a presentation of the different numerical methods used to obtain alternative solutions, and the analogical simulation method used. In the next chapter, the different solutions obtained in this chapter will be analysed.

Chapter 3

Results and Discussions

3.1 Introduction

This chapter is mainly based on the results obtained during our research work. These results focus on the characterization, dynamic evolution and wireless power transmission in electronic circuits exhibiting parity time symmetry. The first circuit is a RLC dimer, the second is the RLC trimer and the third is the RLC quadrimer where each time we have a balance gain and loss between cells. Following these analysis, we compare our results with existing results in the literature in order show the efficiency of parity time symmetry electronic systems compared to simple electronic systems. Thereafter, we generalise the study of wireless power transmission on a chain of n cells where the gain-loss balance is always respected.

3.2 Eigenmodes analysis

3.2.1 RLC Dimer

In the RLC dimer dispersion relations given in eq.(2.34) and eq.(2.35), solving for the small square root leads to the following phase transitions:

$$\gamma_{th1,2} = \frac{\sqrt{\left(2\mu^2 - 2\right)\left(-1 \pm \sqrt{-\mu^2 + 1}\right)}}{1 - \mu^2} \tag{3.1}$$

with $0 \leq \mu \leq 1$. The curve of these equations is shown in Fig.(3.1). Each curve represents the transition threshold (called γ_{th}) between two phase of system. The eigenmodes have three phase: the first phase is real where all eigenmodes are purely real (i.e. $\Im(\omega) = 0$). This phase is limited by the first transition threshold γ_{th1}. After the first phase, the system enter to the complex phase where the real and imaginary part of eigenmodes exist. This phase is limited by the second transition threshold γ_{th2}. After the second transition, the system enter to the imaginary phase where all the eigenmodes are purely imaginary (i.e. $\Re(\omega) = 0$).

Figure (3.2) show the evolution of eigenmodes of RLC dimer. At both transitions, we observe the second order exceptional point where two eigenmodes coalesce. when we

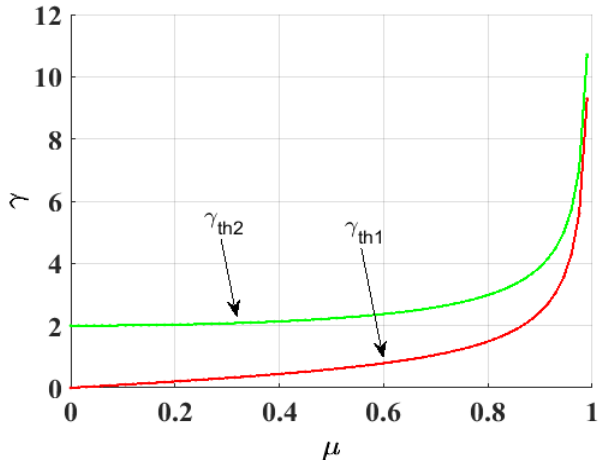

Figure 3.1: Phase transition thresholds of RLC dimer. The red curve is the first transition threshold between the real phase and the complex phase. The green curve is the transition threshold between the complex and the imaginary phase.

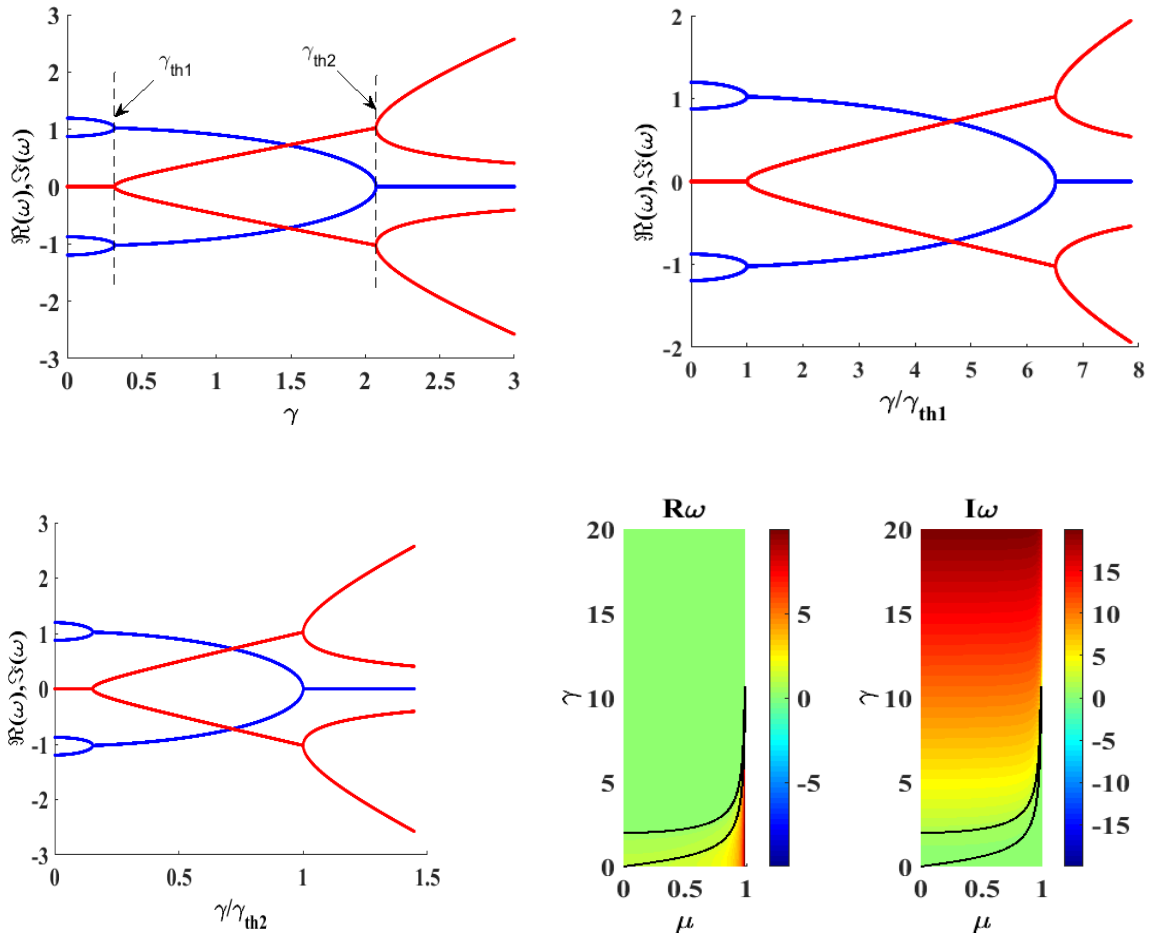

Figure 3.2: Eigenmodes of RLC dimer: (a) : The real part (blue line) and the imaginary part (red line) of eigenmodes for ($\mu = 0.3$) ; (b) : γ is scaled relative to γ_{th1} ; (c) : γ is scaled relative to γ_{th2} ; (d): Summary of eigenvalues in three dimensions.

scale relative to γ_{th}, the transition is reached at $\gamma/\gamma_{th} = 1$. Before the first transition, all eigenmodes are real (exact phase), the circuit can oscillate. After the first transition the system enter to the complex phase where oscillations grow exponentially leading to the destruction of the system (broken phase). Figure 3.2(d) show the evolution of eigenmodes in three dimensions.

3.2.2 RLC Trimer

The eigenvalues given in eq.(2.38), eq.(2.39) and eq.(2.40) have phase transitions at the value $\gamma = \gamma_{th}$. Phase transitions are obtained by solving the expression under the square root $27\,A^2D^2 - 18\,ABC\,(D) + 4\,AC^3 + 4\,B^3\,(D) - B^2C^2 = 0$. Coefficients A, B, C and D are given as $A = (2\mu^2 - 1)$; $B = ((2\mu^2 - 1)\gamma^2 - 2\mu^2 + 3)$; $C = (\gamma^2 - 3)$ and $D = 1$. Solving this equation yields four solutions whose real and imaginary parts are

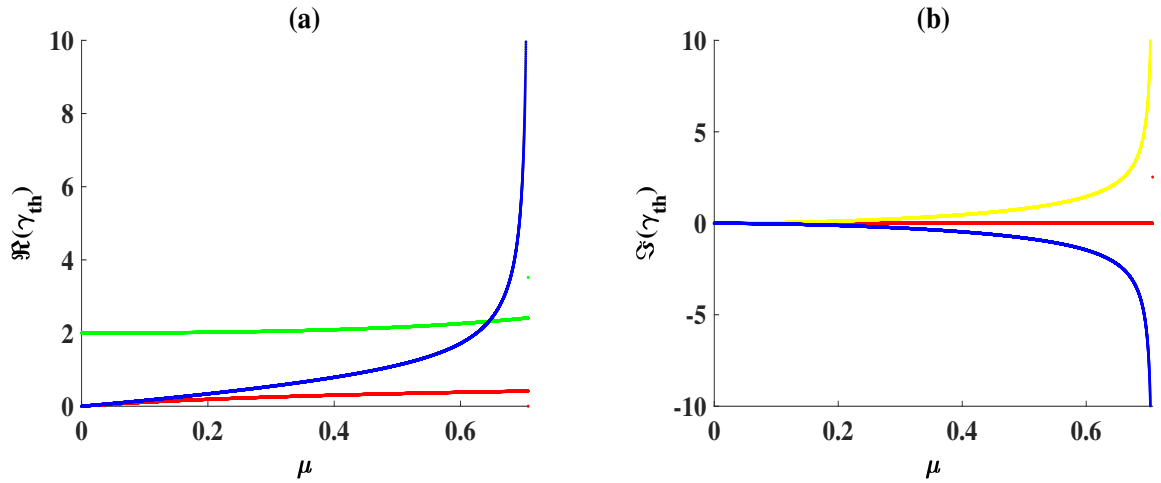

Figure 3.3: Evolution of the different transition of system. (a): Real part of transition. (b): Imaginary part of transition.

shown in Fig. 3.3(a) and (b), respectively. Analysis of these figures shows that, among the four transitions, two are real (red and green). These two transitions limit the three domains observed on the eigenvalue curves given in Fig.3.4. This coupling highlights two exceptional points of order two. Before the first transition, the eigenvalues are real (exact phase) and the system shows oscillations. After this transition, in the other two domains, the eigenvalues become complex (broken phase) and the oscillations of the system vary exponentially.

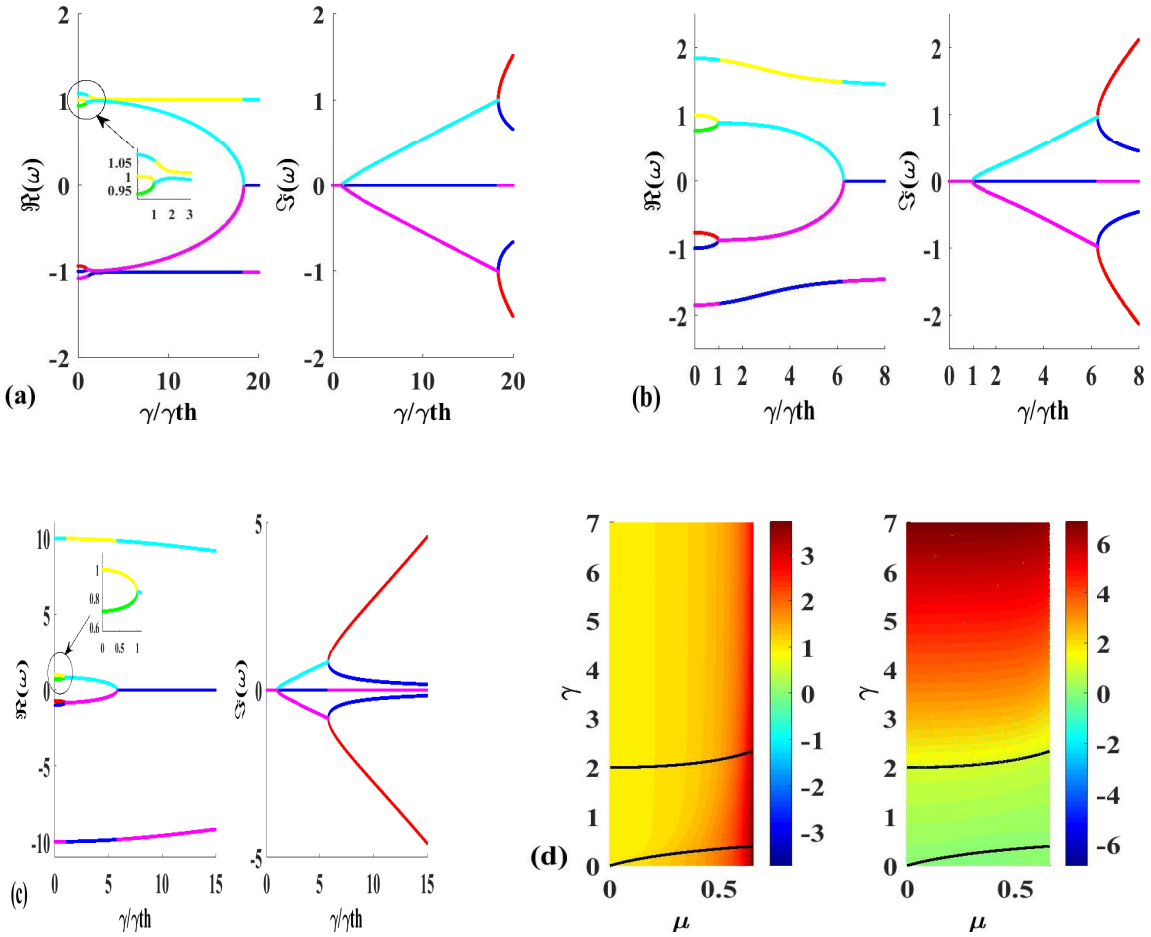

Figure 3.4: Evolution of the Eigenmodes: (a) : The real domain is very small and the three frequencies are close ($\mu = 0.1$) ; (b) : One of the three eigenvalues moves away from the other two ($\mu = 0.5$) ; (c) : The real domain is almost constant and the third eigenvalue moves away more and more from the two others which remain close ($\mu = 0.7$) ; (d): Summary of eigenvalues in three dimensions.

3.2.3 RLC Quadrimer

Let us analyse the quadrimer circuit whose the characteristic equation is presented in eq.(2.42). Solving this equation, the circuit present eight complex eigenvalues (four negatives eigenvalues symmetrical to the four positives) where $0 < \mu < \frac{\sqrt{5}-1}{2}$. In this interval, when $\mu \neq 0.39$, the eight eigenmodes have a same behaviour. For example, let us take the case of $\mu = 0.3$. The eigenmodes present three regions separated by two special points which are the second order exceptional points (two eigenmodes coalesce) (Fig.3.5(a)). Before the first transition, the eigenmodes are purely real. This region is compare to the exact phase where the system present oscillations. Between two transitions and after the second transition, the eigenmodes are complex. We enter to the broken phase where the oscillations of system grow exponentially. When $\mu = 0.39$, the system present the same behaviour but, a particular point appears after the first transition where the eigenmodes are purely real (Fig.3.5(b)). At this point, three among the four positive eigenvalues

coalesce (same to the negatives eigenvalues). We observe the existence of third order exceptional point in the system. In general, the increase of conservative cells between the gain and the loss cell preserves all characteristics of PTS systems. In the next section, we will analyse the transmission of the signal from the source to the load in the general circuit.

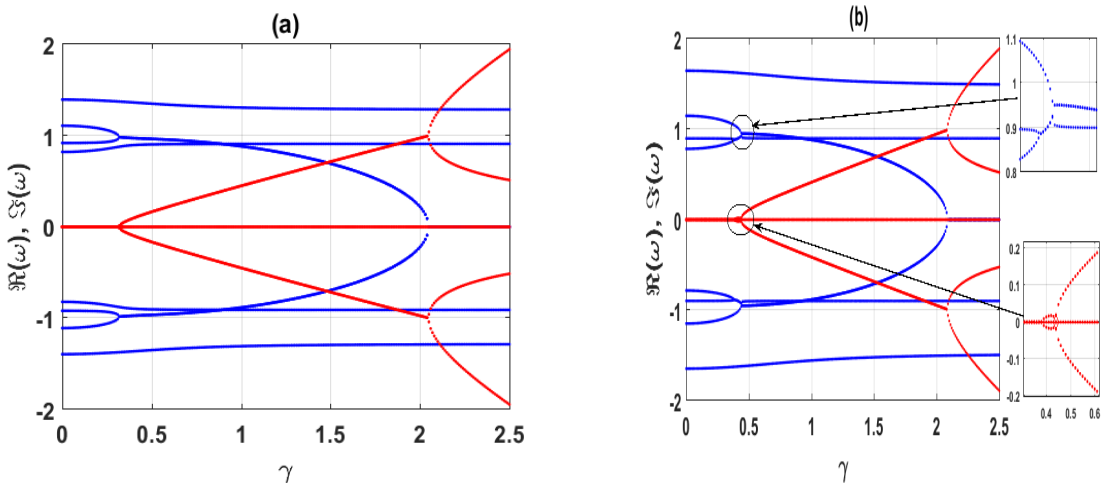

Figure 3.5: Dispersion diagram of real and imaginary part of eigenmodes versus Gain/Loss parameter for some values of coupling parameter μ : (a):$\mu = 0.3$; (b) : $\mu = 0.39$. The blue curves are the real parts and the red curves are the imaginary part.

We can see that non-Hermitian parity time symmetric systems exhibit, under certain conditions, the behaviour of Hermitian systems, which have always been of particular interest in the study of physical phenomena because they have real eigenvalues. In the following, we present the dynamic behaviour of our different models.

3.3 Dynamic evolution

3.3.1 RLC Dimer

The system of differential equations obtained in eq.(2.19) describes the dynamic of the RLC dimer circuit. Solving these equations, we obtain the behavior of the voltages V_1 and V_2 over time in each domain shown in Fig 3.6. In the exact phase where the eigenfrequencies are real, the circuit exhibits oscillations (Fig.(3.6(a),(b)). After this phase, the circuit enter into the broken phase (Fig.3.6(c)). From then, the oscillations of the circuit increase exponentially, leading to saturation or even destruction of the circuit. The curves in the first column are obtained with Matlab and those in the second column with the electronic simulation software LTspice. The theoretical frequency (f_{theo}) obtained with Matlab is identical to that obtained by analogical simulation with LTspice (f_{exp}).

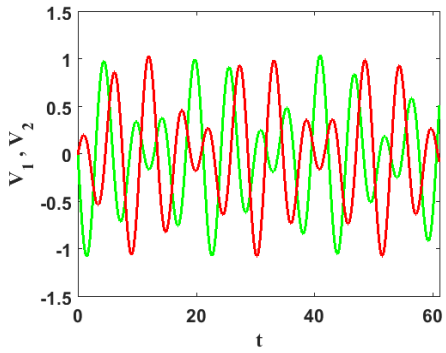
1.5
1
0.5
0
-0.5
-1
-1.5
0
20
40
60
t
V1 , V2

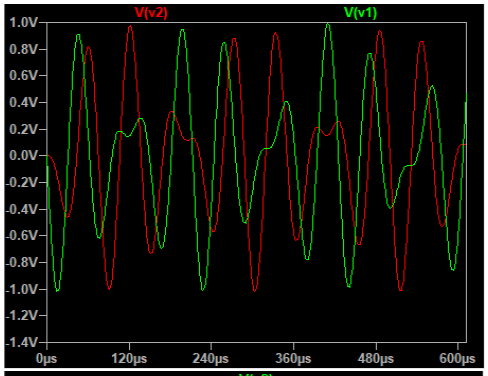
V(v2)
V(v1)
1.0V
0.8V
0.6V
0.4V
0.2V
0.0V
-0.2V
-0.4V
-0.6V
-0.8V
-1.0V
-1.2V
-1.4V
0µs
120µs
240µs
360µs
480µs
600µs

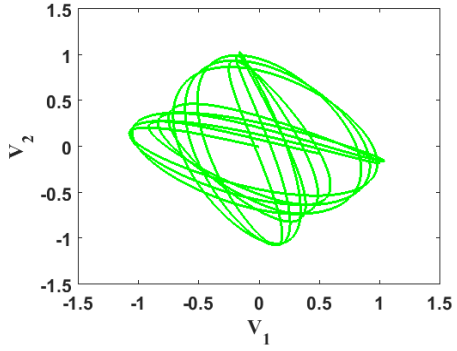
1.5
1
0.5
0
-0.5
-1
-1.5
-1.5
-1
-0.5
0
0.5
1
1.5
V1
V2

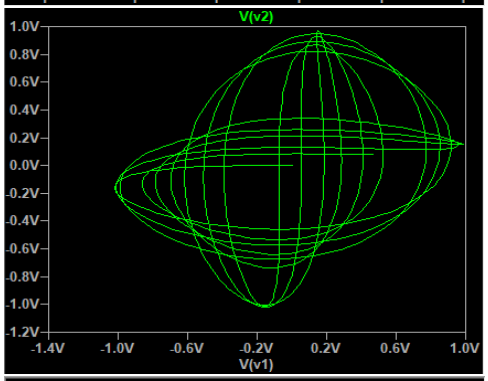
V(v2)
1.0V
0.8V
0.6V
0.4V
0.2V
0.0V
-0.2V
-0.4V
-0.6V
-0.8V
-1.0V
-1.2V
-1.4V
-1.0V
-0.6V
-0.2V
0.2V
0.6V
1.0V
V(v1)

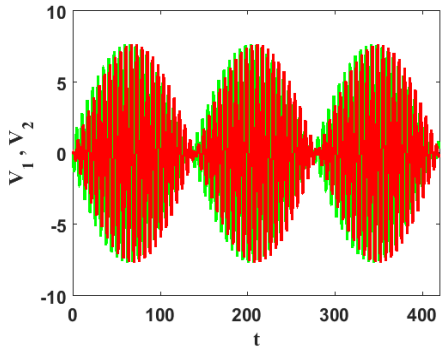
10
5
0
-5
-10
0
100
200
300
400
t
V1 , V2

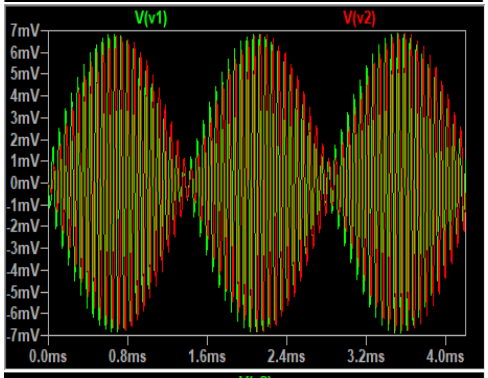
V(v1)
V(v2)
7mV
6mV
5mV
4mV
3mV
2mV
1mV
0mV
-1mV
-2mV
-3mV
-4mV
-5mV
-6mV
-7mV
0.0ms
0.8ms
1.6ms
2.4ms
3.2ms
4.0ms

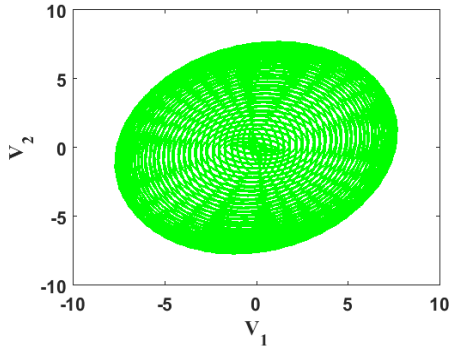
10
5
0
-5
-10
-10
-5
0
5
10
V1
V2

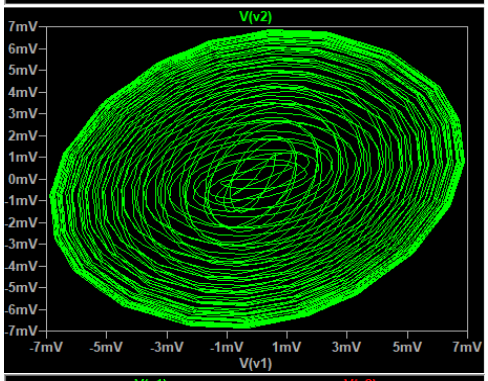
V(v2)
7mV
6mV
5mV
4mV
3mV
2mV
1mV
0mV
-1mV
-2mV
-3mV
-4mV
-5mV
-6mV
-7mV
-7mV
-5mV
-3mV
-1mV
1mV
3mV
5mV
7mV
V(v1)

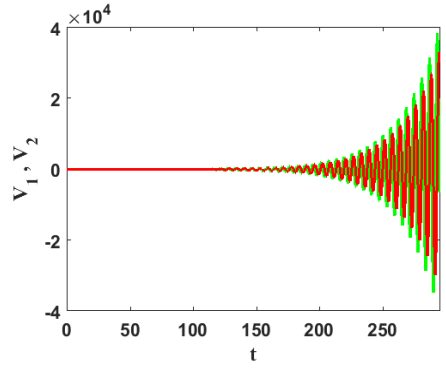
×10^4
4
2
0
-2
-4
0
50
100
150
200
250
t
V1 , V2

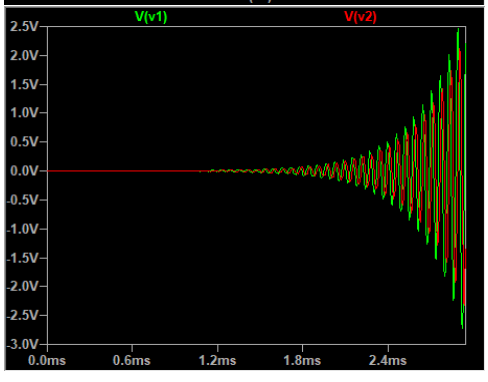
V(v1)
V(v2)
2.5V
2.0V
1.5V
1.0V
0.5V
0.0V
-0.5V
-1.0V
-1.5V
-2.0V
-2.5V
-3.0V
0.0ms
0.6ms
1.2ms
1.8ms
2.4ms

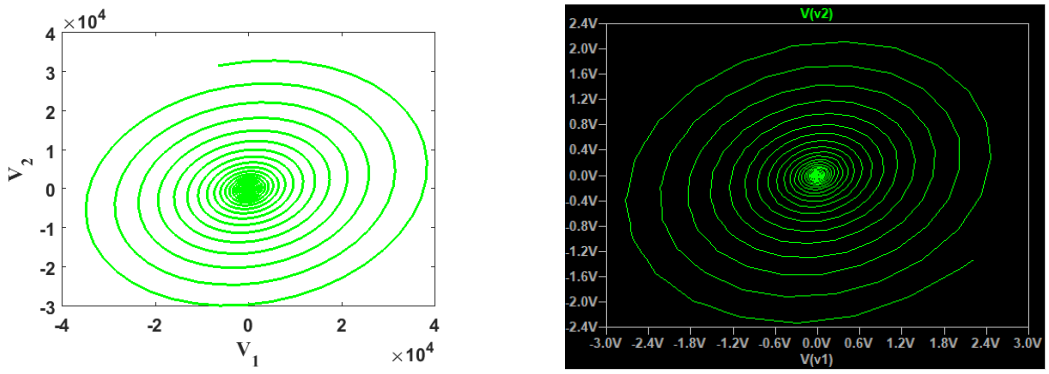

Figure 3.6: First column: Real voltage dynamic across the loss and the gain cells obtained from the numerical simulation at (a):$\frac{\gamma}{\gamma_{PT}} = 0.25\,(25\%)$ ($f_{theo} = 4.90kHz$, $R = 10.25k\Omega$, $f_{\exp} = 4.91kHz$) ; (b):$\frac{\gamma}{\gamma_{PT}} = 0.99\,(99\%)$ ($f_{theo} = 714Hz$, $R = 3.17k\Omega$, $f_{\exp} = 714Hz$) and (c):$\frac{\gamma}{\gamma_{PT}} = 0.102\,(102\%)$ ($f_{theo} = 1.01kHz$, $R = 3.08k\Omega$, $f_{exp} = 1.02kHz$). Second column: Experimental verification by simulation in LTspice respectively.

3.3.2 RLC Trimer

Solving the system eq.(2.23) yields the time solutions $V_i(t)$ shown in Fig 3.7. In the first domain where the eigenvalues are real (i.e. $\Im(\omega) = 0$), as we approach the transition, the system goes from simple oscillations in Fig.3.7(a) to Rabi oscillations in Fig.3.7(b). After this transition, the eigenvalues become complex (i.e. $\Im(\omega) \neq 0$). As a consequence, the oscillations grow exponentially in Fig.3.7(c). The curves in the first column are obtained with Matlab and those in the second column with the electronic simulation software LTspice. The theoretical frequency (f_{theo}) obtained with Matlab is identical to that obtained by analogical simulation with LTspice (f_{exp}).

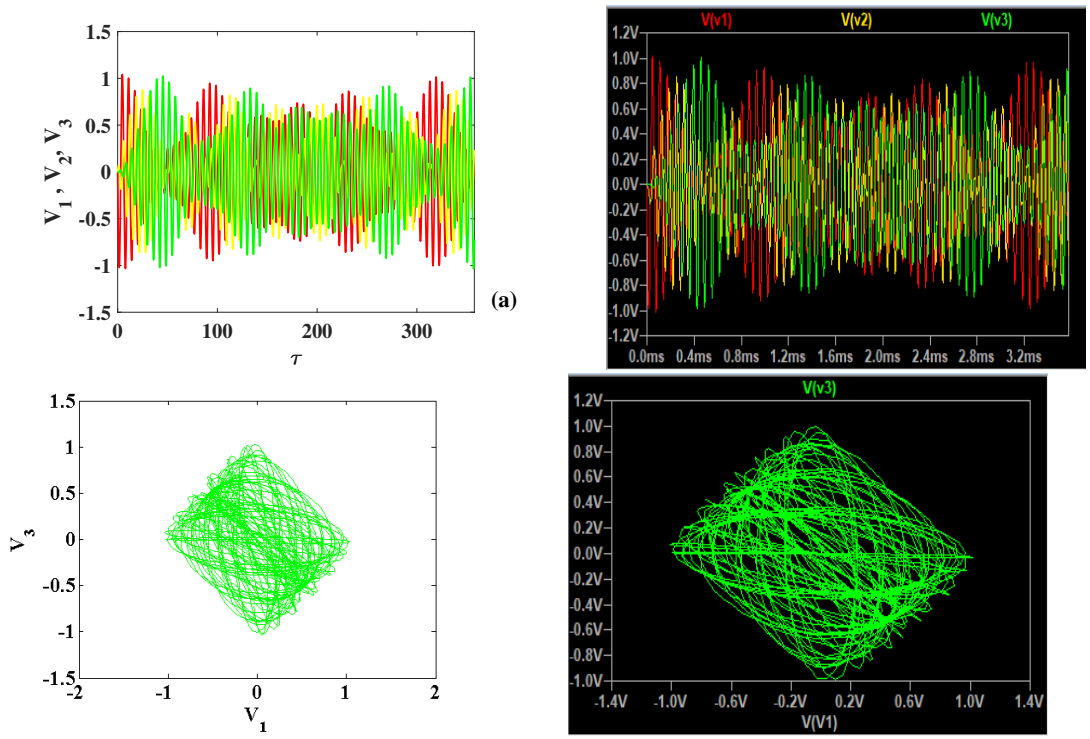

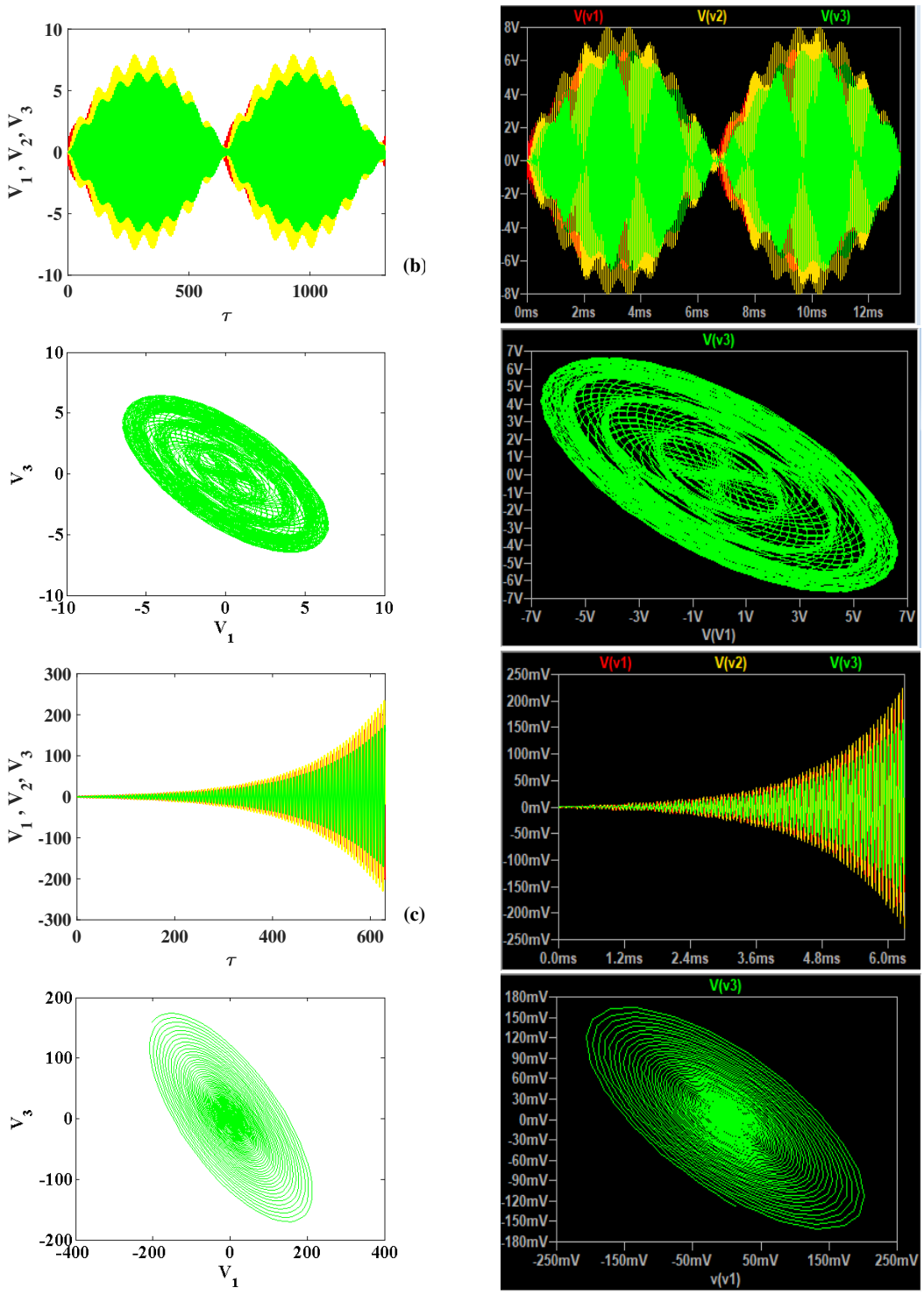

Figure 3.7: First column: Real voltage dynamic across the loss, neutral and the gain cells obtained from the numerical simulation at (a):$\frac{\gamma}{\gamma_{PT}} = 0.25\,(25\%)$ ($f_{theo} = 2.23kHz$, $R = 36.6k\Omega$, $f_{\exp} = 2.23kHz$) ; (b):$\frac{\gamma}{\gamma_{PT}} = 0.99\,(99\%)$ ($f_{theo} = 1.37kHz$, $R = 9.25k\Omega$, $f_{\exp} = 1.73kHz$) and (c):$\frac{\gamma}{\gamma_{PT}} = 0.102\,(102\%)$ ($f_{theo} = 1.26kHz$, $R = 8.97k\Omega$, $f_{exp} = 1.29kHz$). Second column: Experimental verification by simulation in LTspice respectively.

3.3.3 RLC Quadrimer

Like the RLC dimer and RLC trimer, the RLC quadrimer circuit has a exact phase where eigenfrequencies are real and broken phase where the eigenfrequencies become complex. The behaviour of the oscillations is identical in the different phases as in the two previous cases. The study of wireless transfer that follows will be carried out in the exact phase of different circuits where the system has real eigenvalues and the broken phase where eigenvalues are complex.

3.4 Wireless power transfer

Using the transfer function given in eq.(2.54), the S parameter function established in eq.(2.48) gives the results shown in the following figure.

3.4.1 RLC Dimer

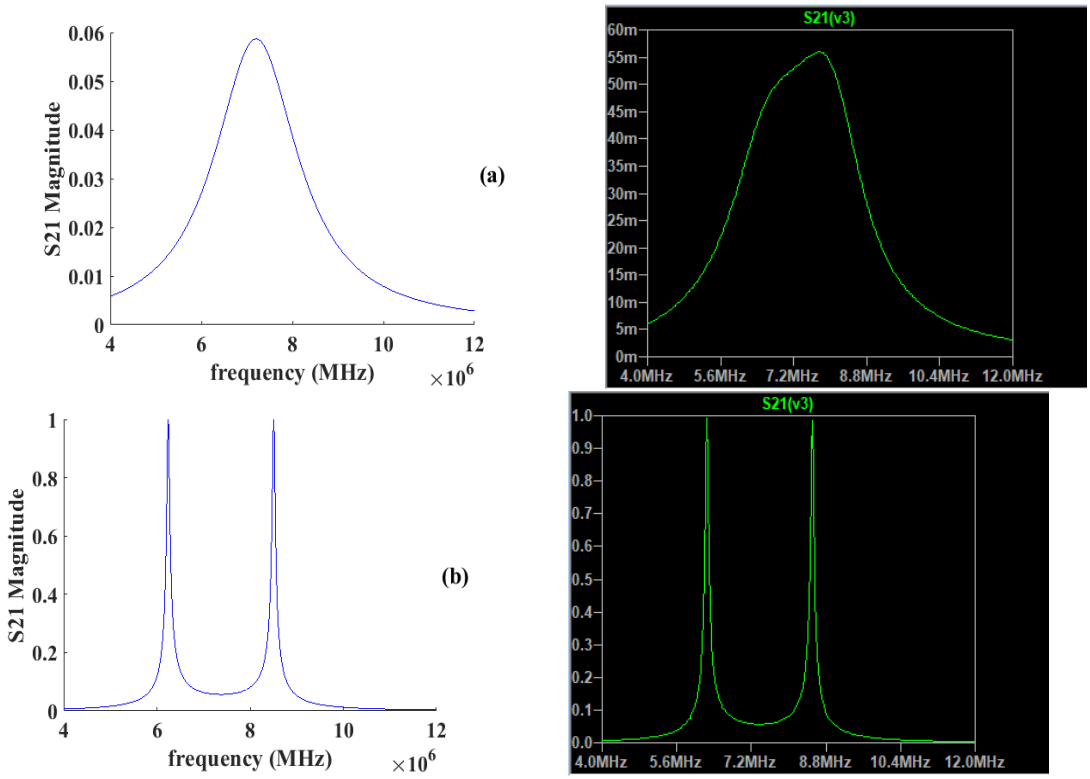

Figure 3.8: Evolution of S_{21} as a function of frequency, the left graphs are the matlab curves and the right graphs are the LT curve: (a): complex domain ($R = 1\Omega$) ; (b): Real domain ($R = 10k\Omega$).

Figure 3.8 presents the magnitude of power transfer function between the source and charge in the RLC dimer circuit. We observe that, in the complex domain where the eigenfrequencies are complex(fig.3.8(a)), the transfer is not efficient. when the value of R

is taken to the exact phase where the circuit oscillates, the transfer function is efficient (fig.3.8(b)).

3.4.2 RLC Trimer

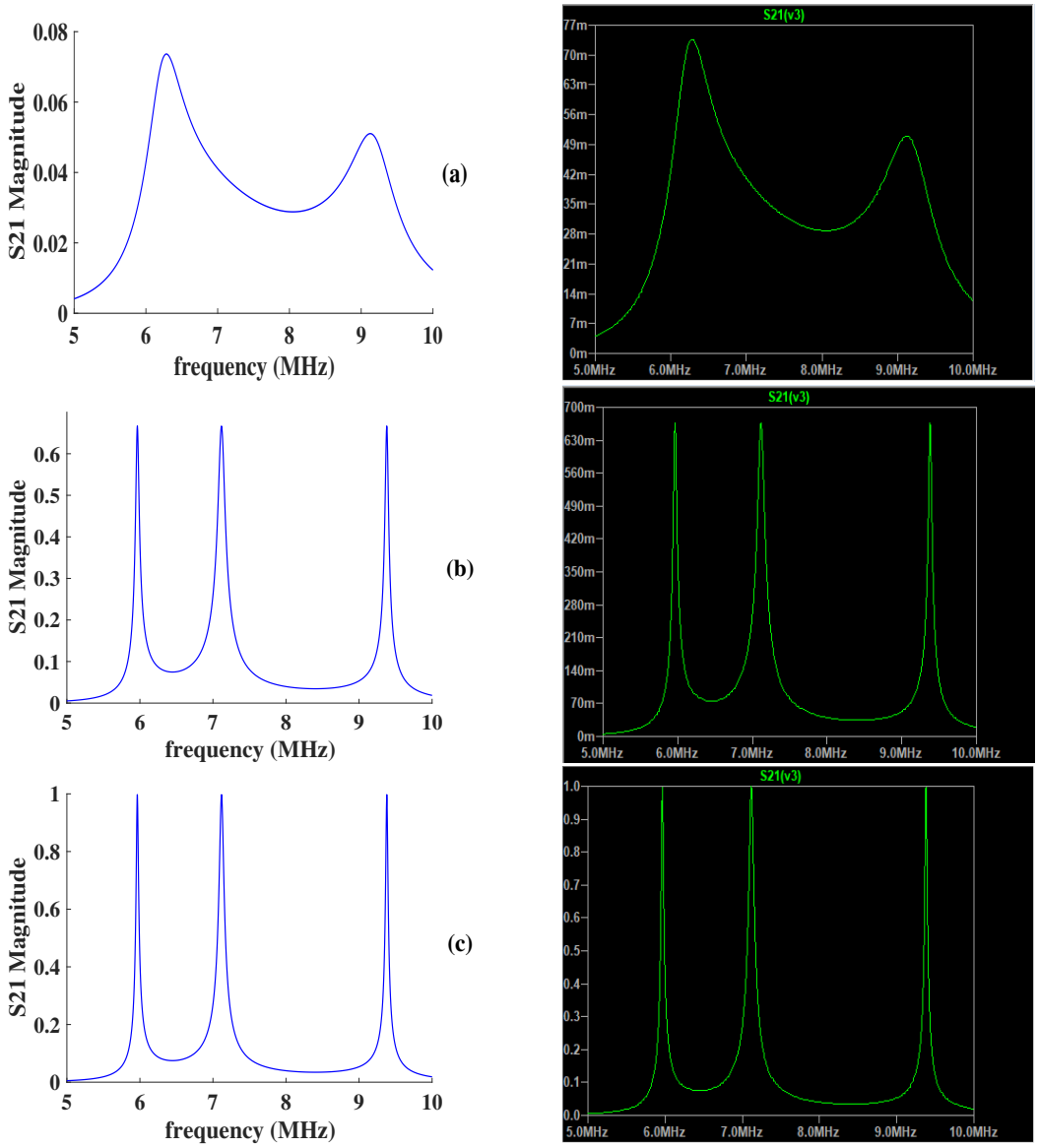

Figure 3.9: Evolution of S_{21} as a function of frequency, the left graphs are the matlab curves and the right graphs are the LT curve: (a): complex domain having two eigenvalues with real positive part ($R = 1\Omega$) ; (b): Real domain a little far from the first transition ($R = 50\Omega$) ; (c): Real domain very far from the first transition ($R = 10k\Omega$).

These curves are obtained with the following values $C = 50nF$; $L = 10nH$; and $R_s = R_l = 50\Omega$. The frequency is $f = \frac{1}{2\pi\sqrt{5\times10^{-16}}} = 7.1176MHz$. The mutual induction coupling value we use is $k_{12} = k_{23} = \mu = 0.3$.

As the value of the gain-loss parameter (R) increases, the system moves from the complex domain after the second transition to the real domain. Fig.(3.9) shows the

evolution of the parameter S_{21} as a function of frequency in the different eigenvalue phases. The system changes from one peak with a low transfer coefficient to three peaks with a high transfer coefficient. These peaks indicate the frequencies at which the transmission is maximum. The troughs between the peaks characterize the frequency ranges at which the transmission is low. In each range, the number of frequencies is related to the number of positive real part eigenvalues. In the complex domain after the second transition, we have a single frequency. Between the two transitions, the system has two frequencies in Fig. 3.9(a) related to the two eigenvalues of this domain. In the real domain, the system has three eigenvalues with positive real part which correspond to the three selective frequencies Fig. 3.9(b) for which the transfer becomes more efficient. When we are close to the beginning of the real domain in Fig. 3.9(c) (when the value of R is high), we reach full efficiency (100%).

For a fixed value of R, Fig.3.10 presents the transfer function for different values of the mutual induction coupling ($0.0001 \leq \mu \leq 0.5$). Each curve represents the transfer parameter as a function of frequency for a value of μ. The higher the value of the mutual induction coupling, the more efficient the transfer. When this coupling parameter is low, the distance between the coils is large and the transfer is low.

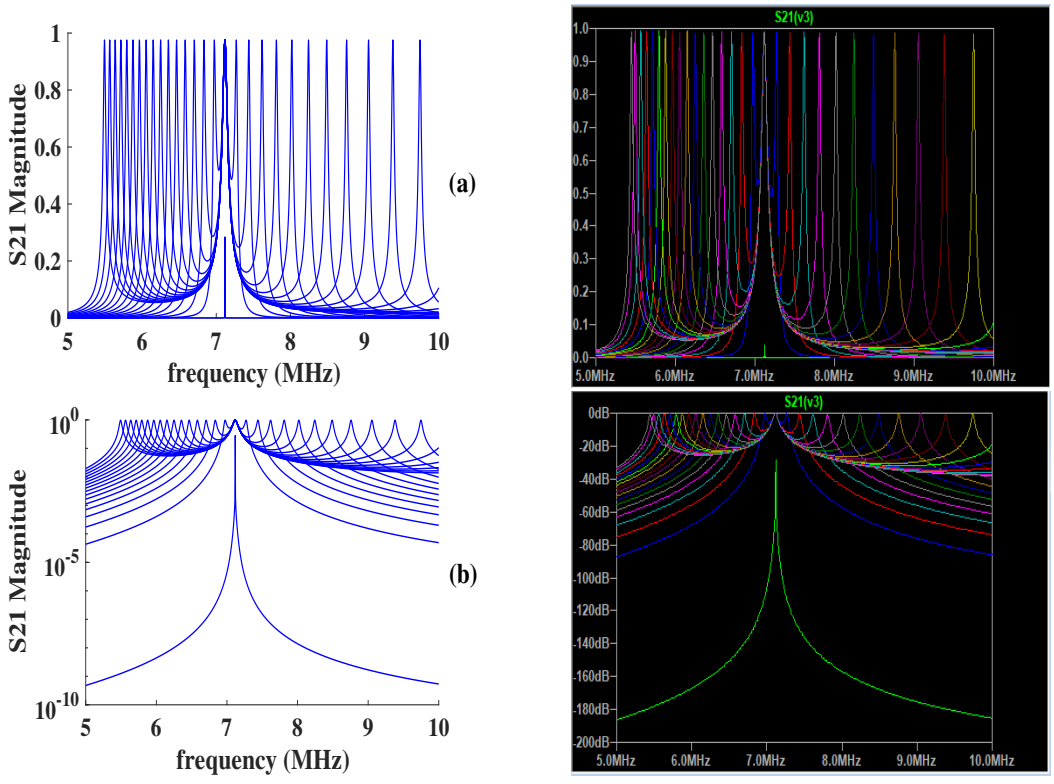

Figure 3.11 shows the evolution of the transfer parameter as a function of the mutual induction coupling and the frequency.

Let us now determine the maximum distance for which we always have an efficient transfer.

The relation linking the coupling parameter as a function of the distance is given by eq.(3.2) [63].

Figure 3.10: Evolution of S_{21} as a function of frequency when we vary the coupling parameter and take $R = 1k\Omega$. (a): The linear curve obtained on Matlab on the left and on LT Spice on the right. (b): The logarithm curve obtained on Matlab on the left and on LT Spice on the right respectively.

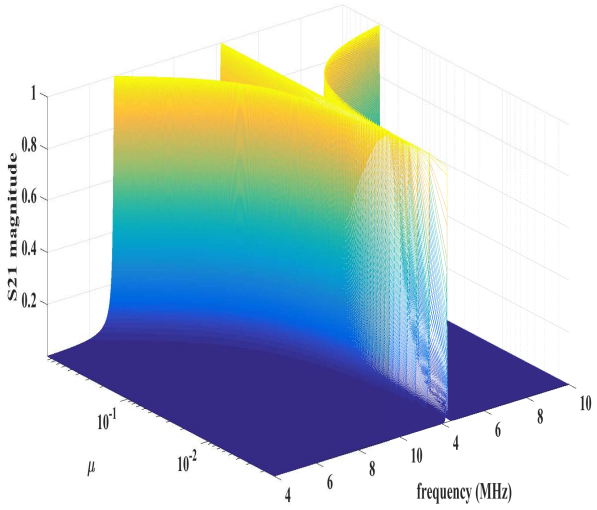

Figure 3.11: Evolution of magnitude as a function of frequency and mutual induction coupling between the three coils of the circuit. ($c = 50nF$; $L = 10nH$; $R = 1k\Omega$; $R_s = R_l = 50\Omega$; $f = 7.1176MHz$).

$$M_{12} = M_{23} = \frac{\mu_0 \pi N_1 N_2 (a_1 a_2)^2}{2(a_1^2 + d^2)^{\frac{3}{2}}}, \tag{3.2}$$

where N_1 and N_2 are numbers of turns, a_1 and a_2 are radii and d is the distance between the coils. Using the relation $\mu = \frac{M}{L}$ where $M = M_{12}$, Figure 3.12 is obtained from figure.3.11 by replacing the coupling coefficient μ by the distance d extracted from eq.(3.2).

Figure 3.13(a) shows the evolution of the transfer parameter as a function of the distance between the coils and figure 3.13(b) gives the evolution of the frequency as a function of the distance between the coils. For a value of $R = 10k\Omega$, we observe that the transfer is efficient (the efficient transfer reaches 99.8%) over a good distance $(0,3 \leq d \leq 1,5m)$ for three specific frequencies. Zhang et al. [56] lists the different results that exist and classify them on several aspects: efficiency, power, distance and many others. Assawaworrarit et al. [60] obtained a total efficiency of 92% and over a distance up to 65 cm between the coils of his circuit. The circuit studied in this paper allows us to obtain an efficient transfer around 100% over a distance of about 1.5 m. Comparing our results, we notice that our circuit is better in terms of efficiency and transmission distance.

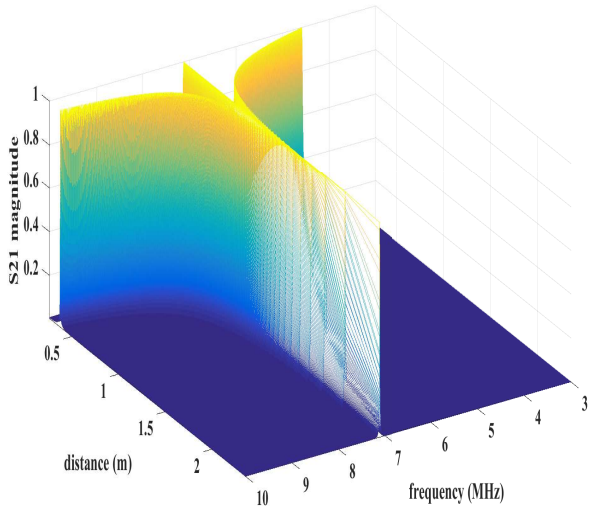

Figure 3.12: Evolution of S_{21} as a function of frequency in $3D$ when we vary the distance and take $R = 1k\Omega$, $N_1 = N_2 = 4turns$, $a_1 = a_2 = 0.05m$.

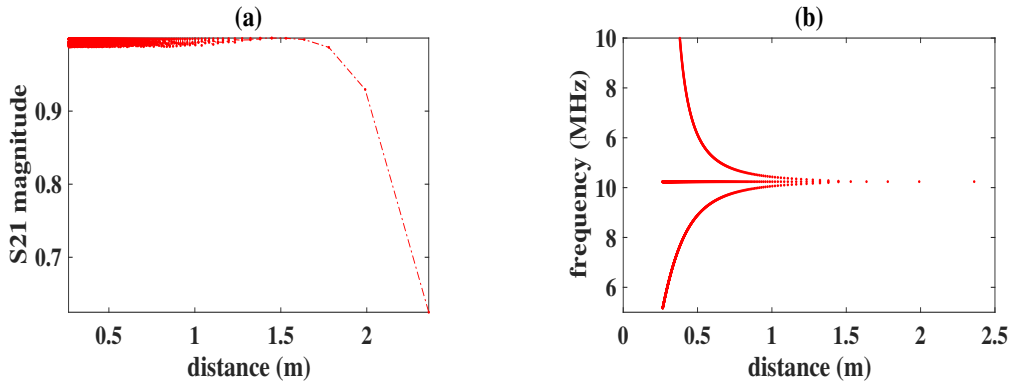

Figure 3.13: Evolution of S_{21} as a function of distance and frequency evolution as a function of distance. (a): maximum efficient transfer as a function of distance. (b): the selective frequencies allowing to have a maximum efficient transfer as a function of distance.

3.5 Generalization of wireless power transfer

The representation of this S-parameter shows that when the value of n increase, the system presents many peaks where the transfer is efficient (Fig.3.14). These peaks are situated around the central frequency. The symmetry of the peaks around the central frequency sufficiently shows the character of the parity time symmetry exhibited by the system [61]. Figure 3.14 is represented for $\mu = 0.3$; $R_S = R_L = 50\,\Omega$; $C = 50nF$ and $L = 10nH$. The frequency is $f = \frac{1}{2\pi\sqrt{5\times10^{-16}}} = 7.1176MHz$.

According to these graphs, from the dimer (Fig.3.14(a)) to the decamer (Fig.3.14(f)) case, the results are analogous to the EIT phenomenon [16] that studies the power of the signal transmitted from the source to the receivers. When the coupling is weak,

the transmitted signal is weak. When we grow to a strong coupling, the transmitted signal reaches its maximum near 100%. Fixing a medium coupling ($\mu = 0.9$) and varying the value of the gain/loss parameter γ in the range of real eigenvalues, the transmitted signal is amplified. This shows that a circuit with parity and time symmetry can better modulate the power of the transmitted signal. For $n = 4$ we have four selective frequencies ($f_1 = 5.840MHz$; $f_2 = 6.537MHz$; $f_3 = 7.886MHz$ and $f_4 = 9.922MHz$); for $n = 5$ the system present five selective frequencies and so on. We observe that the number of selective frequencies is proportional than a number of cells constituting the circuit. If we keep the distance two coils where the transfer is efficient, we notice that, by adding multiple neutral cells between the gain and loss cell, the distance between the source and the load increase. we can use a circuit with several neutral cells to transfer the signal over a greater distance. The $3D$ curves presented in (Fig.3.15(a) and (b)) allow to observe the evolution of the transfer function of signal as a function of the frequency and the coupling parameter μ. In the dimer case, we have two cells, the general PTS electronic circuit offers the possibility to transmit the same signal on several different frequencies. It will therefore b possible to charge the receiver more quickly by using a circuit with several cells. This circuits in the field of telecommunications for charging smartphones and in the automobile for charging batteries will improve the efficiency of the charge.

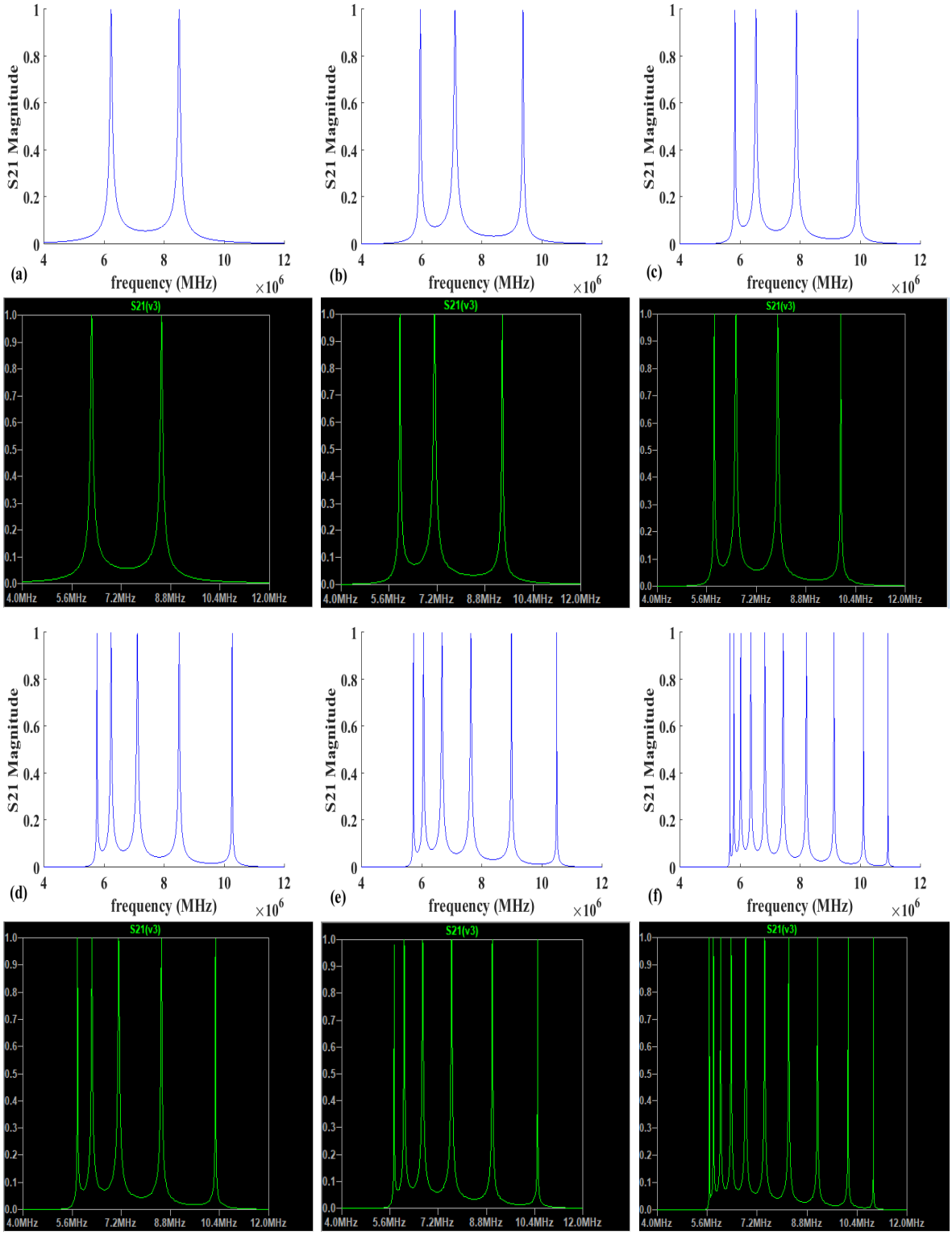

Figure 3.14: Curves of magnitude transfer versus frequency for $\mu = 0.3$. (a): Dimer; (b): Trimer; (c): Quadrimer; (d): Pentamer; (e): Hexamer and (f): Decamer. The white figures are obtained on Matlab and the black figures the corresponding on analog LTspice simulation.

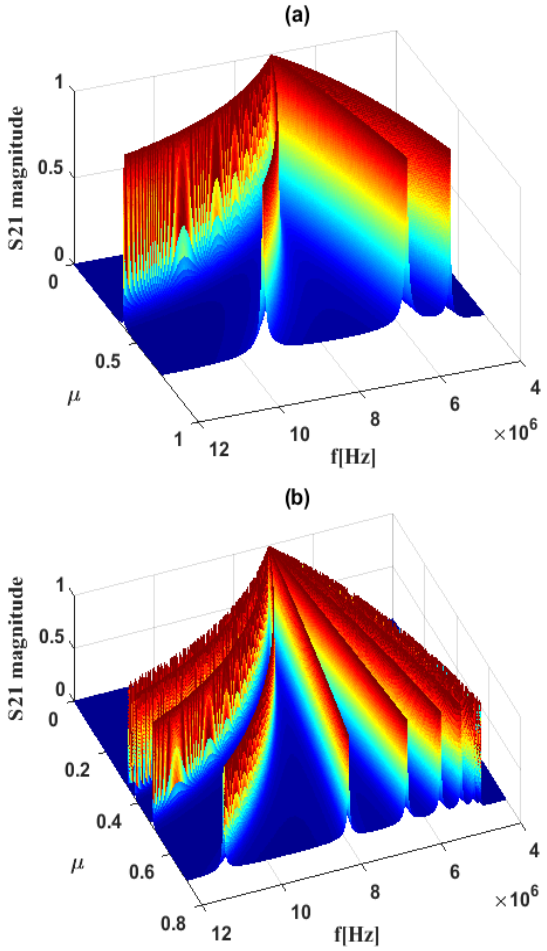

Figure 3.15: Magnitude transfer versus frequency and coupling parameter μ: (a) : case of quadrimer ; (b) : case of decamer

3.6 Conclusion

In this chapter, we have presented and discussed the results obtained in the thesis. We have shown that the non-Hermitian circuits studied do exhibit an exact phase where the eigenvalues are real. In this phase, the circuits oscillate and Hermitian circuit phenomena such as unidirectional transmission are observed. The study of wireless transmission shows that these circuits offer a good percentage of transfer due to the balance gain and loss in the circuit compared with conventional circuits. Based on these results, we can say that circuits with parity and time symmetry will be of capital importance in the choice of useful frequencies for efficient transfer.

General Conclusion

1- Main results of the thesis

Throughout this work, we have focused on the study of wireless transmission in electronic circuits with parity and time symmetry. As this property was originally used in quantum mechanics, its introduction into electronic circuits was not obvious until the appearance of the negative resistor. The wireless coupling used in this work was based on the phenomenon of mutual induction between the coils of the various cells in the circuit. To carry out this work, in Chapter 1 we reviewed the literature on the various key concepts of our work, namely wireless transmission systems and the implementation of time parity symmetry in electronic circuits. Then, in Chapter 2, we presented the analytical and numerical mathematical methods and the analog simulation methods used to solve equations and differential equation systems describing the various circuits studied. In Chapter 3, we presented a summary of the results obtained in this work. These discussions have shown that non-Hermitian circuits have interesting applications, such as the efficient transmission of information. We started with :

⋆ Characterise multi-cell electronic circuits with the characteristic of parity and time symmetry. We carried out investigations on the RLC dimer, the RLC trimer and the RLC quadrimer where we studied the behaviour of their eigenvalues. We have seen that these circuits, although being non-Hermitian, present the real frequency domains where the circuit oscillates and we generalise these circuits by presenting the general matrix for these circuits.

⋆ Study the transmission of a signal from a source to a receiver using our different circuits as intermediary elements. It emerges that these circuits have very specific frequencies where the transfer is efficient. The generalisation this transmission over several circuits shows that the number of frequencies where the transfer is efficient is linked to the number of cells contained in the circuit.

This systems solve the problem of transfer distance, which remains a major challenge when using wireless transfer in many areas, by providing a good distance between the source and the receiver. Compared to the results found in the literature, these results are better, especially in terms of efficiency and distance. These results solve the problem of existing transfer systems that provide maximum transmission for short distances. By applying this system in the field of medicine to recharge cardiac implants, the patient is no longer obliged to stay very close to the source. This circuits in the field of telecom-

munications for charging smartphones and in the automobile for charging batteries will improve the efficiency of the charge. This circuits can also be used for wireless lighting.

2- Future works

Despite the results that were obtained in this thesis, other points of interest may be solved in the future to complete and get a better understanding on topics discussed here.

- It would be interesting to add capacitive cutting in order to see the power of transmission..
- It would be also interesting to Couple different chains and evaluating the transmission between transmitter and receiver.
- In addition to this work, it would be interesting to apply them to practical cases such as wireless charging of equipment in order to analyse the charging power.

Bibliography

[1] Tesla, N. (1904). The transmission of electrical energy without wires. Electrical World and Engineer, 1, 21-24.

[2] Dai, J., Ludois, D. C. (2015). A survey of wireless power transfer and a critical comparison of inductive and capacitive coupling for small gap applications. IEEE Transactions on Power Electronics, 30(11), 6017-6029.

[3] Kalwar, K. A., Aamir, M., Mekhilef, S. (2015). Inductively coupled power transfer (ICPT) for electric vehicle charging–A review. Renewable and Sustainable Energy Reviews, 47, 462-475.

[4] Zhao, J., Zhang, J., Zhu, Y. (2019). A flexible wireless power transfer system with switch controlled capacitor. IEEE Access, 7, 106873-106881.

[5] Alhamrouni, I., Iskandar, M., Salem, M., Awalin, L. J., Jusoh, A., Sutikno, T. (2020). Application of inductive coupling for wireless power transfer. International Journal of Power Electronics and Drive Systems, 11(3), 1109.

[6] Kim, H. J., Hirayama, H., Kim, S., Han, K. J., Zhang, R., Choi, J. W. (2017). Review of near-field wireless power and communication for biomedical applications. IEEE Access, 5, 21264-21285.

[7] Jung, Y. B. (2018). Technical Trend of Long-range Wireless Power Transfer. Journal of IKEEE, 22(1), 216-222.

[8] Lu, F., Zhang, H., Hofmann, H., Mi, C. C. (2016). An inductive and capacitive combined wireless power transfer system with LC-compensated topology. IEEE Transactions on Power Electronics, 31(12), 8471-8482.

[9] Kisseleff, S., Chen, X., Akyildiz, I. F., Gerstacker, W. H. (2016). Efficient charging of access limited wireless underground sensor networks. IEEE Transactions on Communications, 64(5), 2130-2142.

[10] Bender, C. M., Boettcher, S. (1998). Real spectra for non-Hermitian Hamiltonians using a GPT-like transformation. Physical Review Letters, 80(18), 4274.

[11] El-Ganainy, R., Makris, K. G., Christodoulides, D. N., Musslimani, Z. H. (2007). Theory of coupled optical PT-symmetric structures. Optics letters, 32(17), 2632-2634.

[12] Lin, Z., Ramezani, H., Eichelkraut, T., Kottos, T., Cao, H., Christodoulides, D. N. (2011). Unidirectional invisibility induced by P T-symmetric periodic structures. Physical Review Letters, 106(21), 213901.

[13] Regensburger, A., Bersch, C., Miri, M. A., Onishchukov, G., Christodoulides, D. N., Peschel, U. (2012). Parity–time synthetic photonic lattices. Nature, 488(7410), 167-171.

[14] Feng, L., Xu, Y. L., Fegadolli, W. S., Lu, M. H., Oliveira, J. E., Almeida, V. R., Scherer, A. (2013). Experimental demonstration of a unidirectional reflectionless parity-time metamaterial at optical frequencies. Nature materials, 12(2), 108-113.

[15] Feng, L., Wong, Z. J., Ma, R. M., Wang, Y., Zhang, X. (2014). Single-mode laser by parity-time symmetry breaking. Science, 346(6212), 972-975.

[16] Hodaei, H., Miri, M. A., Heinrich, M., Christodoulides, D. N., Khajavikhan, M. (2014, June). *PT* Symmetric Large Area Single Mode DFB Lasers. In CLEO : QELS-Fundamental Science (pp. FM1D-3). Optica Publishing Group.

[17] Brandstetter, M., Liertzer, M., Deutsch, C., Klang, P., Schöberl, J., Türeci, H. E., Rotter, S. (2014). Reversing the pump dependence of a laser at an exceptional point. Nature communications, 5(1), 4034.

[18] Peng, B., Özdemir, Ş. K., Rotter, S., Yilmaz, H., Liertzer, M., Monifi, F., Yang, L. (2014). Loss-induced suppression and revival of lasing. Science, 346(6207), 328-332.

[19] Zhu, L., Dong, L. (2022). Electromagnetically induced transparency metamaterials: theories, designs and applications. Journal of Physics D: Applied Physics, 55(26), 263003.

[20] Lei, X., Ma, L., Yan, J., Zhou, X., Yan, Z., Jia, X. (2022). Electromagnetically induced transparency quantum memory for non-classical states of light. Advances in Physics: X, 7(1), 2060133.

[21] Tagouegni, S., Fotsa-Ngaffo, F., Kenfack-Jiotsa, A. (2022). Non-Hermitian electronics multipods of electromagnetically induced transparency (EIT) and absorption (EIA). Optical and Quantum Electronics, 54(3), 200.

[22] Hodaei, H., Hassan, A. U., Wittek, S., Garcia-Gracia, H., El-Ganainy, R., Christodoulides, D. N., Khajavikhan, M. (2017). Enhanced sensitivity at higher-order exceptional points. Nature, 548(7666), 187-191.

[23] Chen, W., Kaya Özdemir, Ş., Zhao, G., Wiersig, J., Yang, L. (2017). Exceptional points enhance sensing in an optical microcavity. Nature, 548(7666), 192-196.

[24] Yim, J., Zhao, H., Midya, B., Feng, L. (2019). Non-Hermitian heterostructure for two-parameter sensing. Optics Letters, 44(7), 1626-1629.

[25] Zhou, X., Gupta, S. K., Huang, Z., Yan, Z., Zhan, P., Chen, Z., Wang, Z. (2018). Optical lattices with higher-order exceptional points by non-Hermitian coupling. Applied Physics Letters, 113(10).

[26] Sakhdari, M., Chen, P. Y. (2017). Ultrasensitive telemetric sensor based on adapted parity-time symmetry. In 2017 IEEE International Symposium on Antennas and Propagation and USNC/URSI National Radio Science Meeting (pp. 579-580). IEEE.

[27] Chen, P. Y., Sakhdari, M. (2018). High-Order PT-Symmetric Telemetric Sensors with Singularity-Enhanced Sensitivity. In 2018 IEEE International Symposium on Antennas and Propagation and USNC/URSI National Radio Science Meeting (pp. 2011-2012). IEEE.

[28] Azeghap-Simo, I., Fotsa-Ngaffo, F., Kenfack-Jiotsa, A. (2023). Dynamics of cubic–quintic nonlinear PT-symmetry mechanical oscillators. Physica D: Nonlinear Phenomena, 449, 133750.

[29] Mao, X., Qin, G. Q., Yang, H., Zhang, H., Wang, M., Long, G. L. (2020). Enhanced sensitivity of optical gyroscope in a mechanical parity-time-symmetric system based on exceptional point. New Journal of Physics, 22(9), 093009.

[30] Zhang, Z., Pang, H., Georgiadis, A., Cecati, C. (2018). Wireless power transfer—An overview. IEEE transactions on industrial electronics, 66(2), 1044-1058.

[31] Assawaworrarit, S., Fan, S. (2020). Efficient and robust wireless power transfer based on parity-time symmetry. In AIP Conference Proceedings (Vol. 2300, No. 1). AIP Publishing.

[32] Sakhdari, M., Chen, P. Y. (2019). Efficient and misalignment-robust PT-symmetric wireless power transfer. In 2019 IEEE International Symposium on Antennas and Propagation and USNC-URSI Radio Science Meeting (pp. 1459-1460). IEEE.

[33] Sakhdari, M., Hajizadegan, M., Chen, P. Y. (2020). Robust extended-range wireless power transfer using a higher-order PT-symmetric platform. Physical Review Research, 2(1), 013152.

[34] Fang, W., Deng, H., Liu, Q., Liu, M., Jiang, Q., Yang, L., Giannakis, G. B. (2021). Safety analysis of long-range and high-power wireless power transfer using resonant beam. IEEE Transactions on Signal Processing, 69, 2833-2843.

[35] Sakhdari, M., Chen, P. Y. (2019). Efficient and misalignment-robust PT-symmetric wireless power transfer. In 2019 IEEE International Symposium on Antennas and Propagation and USNC-URSI Radio Science Meeting (pp. 1459-1460). IEEE.

[36] Kiani, M., Ghovanloo, M. (2012). The circuit theory behind coupled-mode magnetic resonance-based wireless power transmission. IEEE Transactions on Circuits and Systems I: Regular Papers, 59(9), 2065-2074.

[37] Assawaworrarit, S., Yu, X., Fan, S. (2017). Robust wireless power transfer using a nonlinear parity–time-symmetric circuit. Nature, 546(7658), 387-390.

[38] Baev, A., Prasad, P. N., Ågren, H., Samoć, M., Wegener, M. (2015). Metaphotonics: An emerging field with opportunities and challenges. Physics Reports, 594, 1-60.

[39] Tassin, P., Zhang, L., Koschny, T., Economou, E. N., Soukoulis, C. M. (2009). Low-loss metamaterials based on classical electromagnetically induced transparency. Physical review letters, 102(5), 053901.

[40] Tesla N (1898). High frequency oscillators for electro-therapeutic and other purposes. Electr Eng XXVI(550).

[41] Tesla, N., Childress, D. H. (1993). The fantastic inventions of Nikola Tesla. Adventures Unlimited.

[42] Hutin M, Leblanc M (1894). Transformer system for electric railways. US patent 527 857, 23 Oct 1894

[43] Nikola Tesla. (1943). In : Proceedings of the I.R.E., 194.

[44] Lomas, R., Docking, J. (1999). The man who invented the twentieth century: Nikola Tesla, forgotten genius of electricity (Vol. 146).

[45] Rim, C. T., Mi, C. (2017). Wireless power transfer for electric vehicles and mobile devices. John Wiley and Sons.

[46] Joun, G. B., Cho, B. H. (1998). An energy transmission system for an artificial heart using leakage inductance compensation of transcutaneous transformer. IEEE Transactions on Power Electronics, 13(6), 1013-1022.

[47] Ghahary, A., Cho, B. H. (1990). Design of a Transcutaneous Energy Transmission System Using a Series Resonant Converter', IEEE Power Electronics Specialists Conf.

[48] Green, A. W., Boys, J. T. (1994). 10 kHz inductively coupled power transfer-concept and control.

[49] Elliott, G. A. J., Boys, J. T., Green, A. W. (1995). Magnetically coupled systems for power transfer to electric vehicles. In Proceedings of 1995 International Conference on Power Electronics and Drive Systems. PEDS 95 (pp. 797-801). IEEE.

[50] Jang, Y., Jovanovic, M. M. (2003). A contactless electrical energy transmission system for portable-telephone battery chargers. IEEE Transactions on Industrial Electronics, 50(3), 520-527.

[51] Kim, C. G., Seo, D. H., You, J. S., Park, J. H., Cho, B. H. (2001). Design of a contactless battery charger for cellular phone. IEEE Transactions on Industrial Electronics, 48(6), 1238-1247.

[52] Popović, Z., Falkenstein, E. A., Costinett, D., Zane, R. (2013). Low-power far-field wireless powering for wireless sensors. Proceedings of the IEEE, 101(6), 1397-1409.

[53] Choi, B., Nho, J., Cha, H., Ahn, T., Choi, S. (2004). Design and implementation of low-profile contactless battery charger using planar printed circuit board windings as energy transfer device. IEEE Transactions on Industrial Electronics, 51(1), 140-147.

[54] Hui SYR. (2005). Planar inductive battery charger.

[55] Cheng, L. K. L., Hay, J. W., Beart, P. G. W. (2005). U.S. Patent No. 6,906,495. Washington, DC: U.S. Patent and Trademark Office.

[56] IHS Markit j Leading Source of Critical Information. https ://ihs-markit.com/index.html

[57] Energy Research j Navigant Research. https ://www.navigantresearch.com/

[58] On line : https ://en.wikipedia.org/

[59] Triviño-Cabrera, A., González-González, J. M., Aguado, J. A. (2020). Wireless power transfer for electric vehicles: foundations and design approach.

[60] Chau, K. T. (2015). Electric vehicle machines and drives: design, analysis and application. John Wiley and Sons.

[61] Hui, S. Y. R., Zhong, W., Lee, C. K. (2013). A critical review of recent progress in mid-range wireless power transfer. IEEE Transactions on Power Electronics, 29(9), 4500-4511.

[62] Choi, B. H., Thai, V. X., Lee, E. S., Kim, J. H., Rim, C. T. (2016). Dipole-coil-based wide-range inductive power transfer systems for wireless sensors. IEEE Transactions on Industrial Electronics, 63(5), 3158-3167.

[63] Park, C., Lee, S., Cho, G. H., Rim, C. T. (2014). Innovative 5-m-off-distance inductive power transfer systems with optimally shaped dipole coils. IEEE transactions on power electronics, 30(2), 817-827.

[64] Lim, Y., Tang, H., Lim, S., Park, J. (2013). An adaptive impedance-matching network based on a novel capacitor matrix for wireless power transfer. IEEE Transactions on Power Electronics, 29(8), 4403-4413.

[65] Mohseni, F., Nikzamir, A., Cao, H., Capolino, F. (2022). One-transmitter Multiple-receiver Wireless Power Transfer System Using an Exceptional Point of Degeneracy. arXiv preprint arXiv:2204.10928.

[66] Zhou, J., Zhang, B., Xiao, W., Qiu, D., Chen, Y. (2018). Nonlinear parity-time-symmetric model for constant efficiency wireless power transfer: Application to a drone-in-flight wireless charging platform. IEEE Transactions on Industrial Electronics, 66(5), 4097-4107.

[67] Jiang, C., Chau, K. T., Liu, C., Lee, C. H. (2017). An overview of resonant circuits for wireless power transfer. Energies, 10(7), 894.

[68] Yan, Z., Zhang, Y., Kan, T., Lu, F., Zhang, K., Song, B., Mi, C. C. (2018). Frequency optimization of a loosely coupled underwater wireless power transfer system considering eddy current loss. IEEE Transactions on Industrial Electronics, 66(5), 3468-3476.

[69] Kang, S. G., Song, M. S., Kim, J. W., Lee, J. W., Kim, J. (2021). Near-field communication in biomedical applications. Sensors, 21(3), 703.

[70] Massa, A., Oliveri, G., Viani, F., Rocca, P. (2013). Array designs for long-distance wireless power transmission: State-of-the-art and innovative solutions. Proceedings of the IEEE, 101(6), 1464-1481.

[71] Covic, G. A., Boys, J. T. (2013). Inductive power transfer. Proceedings of the IEEE, 101(6), 1276-1289.

[72] Mayordomo, I., Dräger, T., Spies, P., Bernhard, J., Pflaum, A. (2013). An overview of technical challenges and advances of inductive wireless power transmission. Proceedings of the IEEE, 101(6), 1302-1311.

[73] Zhang, J., Yuan, X., Wang, C., He, Y. (2016). Comparative analysis of two-coil and three-coil structures for wireless power transfer. IEEE Transactions on Power Electronics, 32(1), 341-352.

[74] Kurs, A., Karalis, A., Moffatt, R., Joannopoulos, J. D., Fisher, P., Soljacic, M. (2007). Wireless power transfer via strongly coupled magnetic resonances. science, 317(5834), 83-86.

[75] Cheon, S., Kim, Y. H., Kang, S. Y., Lee, M. L., Lee, J. M., Zyung, T. (2010). Circuit-model-based analysis of a wireless energy-transfer system via coupled magnetic resonances. IEEE Transactions on Industrial Electronics, 58(7), 2906-2914.

[76] Lu, K., Nguang, S. K., Ji, S., Wei, L. (2017). Design of auto frequency tuning capacitive power transfer system based on

[77] Lu, F., Zhang, H., Mi, C. (2017). A review on the recent development of capacitive wireless power transfer technology. Energies, 10(11), 1752.

[78] Jin, K., Zhou, W. (2018). Wireless laser power transmission: A review of recent progress. IEEE Transactions on Power Electronics, 34(4), 3842-3859.

[79] Gibbs, Y. (2015). NASA Dryden Fact Sheets-Beamed Laser Power.

[80] Zhou, W., Jin, K. (2015). Efficiency evaluation of laser diode in different driving modes for wireless power transmission. IEEE Transactions on Power Electronics, 30(11), 6237-6244.

[81] Jung, Y. B. (2018). Technical Trend of Long-range Wireless Power Transfer. Journal of IKEEE, 22(1), 216-222.

[82] Sample, A. P., Meyer, D. T., Smith, J. R. (2010). Analysis, experimental results, and range adaptation of magnetically coupled resonators for wireless power transfer. IEEE Transactions on industrial electronics, 58(2), 544-554.

[83] Fletcher, N. H., Rossing, T. D. (2012). The physics of musical instruments. Springer Science and Business Media.

[84] Mongia, R., Bahl, I. J., Bhartia, P. (1999). RF and microwave coupled-line circuits. (No Title).

[85] Chen, W. K., Choma, J. (2007). Feedback Networks: Theory and Circuit Applications (Advanced Series in Circuits and Systems). World Scientific Press.

[86] Schrödinger, E. (1926). The quantum theory of the radiation problem. I. Annalen der Physik, 79(42), 437-467.

[87] Lechner, G. (2008). Construction of quantum field theories with factorizing S-matrices. Communications in Mathematical Physics, 277, 821-860.

[88] Dyson, F. J. (1949). The S matrix in quantum theory. Physical Review, 75(1), 173.

[89] He, K., Zhang, S., Sun, W., Xu, Y. (2019). Parity-time symmetry in physics. World Scientific Publishing Company.

[90] Kottos, T., Weaver, D. R. (2006). Chaos : from simple systems to turbulence. Cambridge University Press

[91] Longhi, S. (2013). PT symmetry breaking and a road to no gain. Journal of Optics, 15(6), 065401.

[92] Guo, A., Liu, X., Zhang, X. (2021). Non-Hermitian physics : Basic concepts and frontier topics. World Scientific Publishing Company

[93] Wang, X., Wu, J. H. (2016). Optical PT-symmetry and PT-antisymmetry in coherently driven atomic lattices. Optics express, 24(4), 4289-4298.

[94] Bender, C. M. (2007). Making sense of non-Hermitian Hamiltonians. Reports on Progress in Physics, 70(6), 947.

[95] Heiss, W. D. (2004). Exceptional points of non-Hermitian operators. Journal of Physics A: Mathematical and General, 37(6), 2455.

[96] Weigert, S. (2003). Completeness and orthonormality in PT-symmetric quantum systems. Physical Review A, 68(6), 062111.

[97] Mostafazadeh, A. (2003). Exact PT-symmetry is equivalent to Hermiticity. Journal of Physics A: Mathematical and General, 36(25), 7081.

[98] Bender, C. M., Brody, D. C., Jones, H. F. (2002). Complex extension of quantum mechanics. Physical review letters, 89(27), 270401.

[99] Makris, K. G., El-Ganainy, R., Christodoulides, D. N., Musslimani, Z. H. (2008). Beam dynamics in P T symmetric optical lattices. Physical Review Letters, 100(10), 103904.

[100] Humire, F. R., Lazo, E. (2019). PT-symmetric direct electrical transmission lines: Localization behavior. Physical Review E, 100(2), 022221.

[101] Mostafazadeh, A. (2009). Spectral singularities of complex scattering potentials and infinite reflection and transmission coefficients at real energies. Physical review letters, 102(22), 220402.

[102] Fleury, R., Sounas, D., Alu, A. (2015). An invisible acoustic sensor based on parity-time symmetry. Nature communications, 6(1), 5905.

[103] Mostafazadeh, A. (2010). Pseudo-Hermitian representation of quantum mechanics. International Journal of Geometric Methods in Modern Physics, 7(07), 1191-1306.

[104] Ramezani, H., Li, H. K., Wang, Y., Zhang, X. (2014). Unidirectional spectral singularities. Physical review letters, 113(26), 263905.

[105] Sukhorukov, A. A., Xu, Z., Kivshar, Y. S. (2010). Nonlinear suppression of time reversals in PT-symmetric optical couplers. Physical Review A, 82(4), 043818.

[106] Lumer, Y., Plotnik, Y., Rechtsman, M. C., Segev, M. (2013). Nonlinearly induced P T transition in photonic systems. Physical review letters, 111(26), 263901.

[107] Makris, K. G., El-Ganainy, R., Christodoulides, D. N., Musslimani, Z. H. (2010). PT-symmetric optical lattices. Physical Review A, 81(6), 063807.

[108] West, C. T., Kottos, T., Prosen, T. (2010). P t-symmetric wave chaos. Physical review letters, 104(5), 054102.

[109] Longhi, S. (2010). PT-symmetric laser absorber. Physical Review A, 82(3), 031801.

[110] Chong, Y. D., Ge, L., Stone, A. D. (2011). P t-symmetry breaking and laser-absorber modes in optical scattering systems. Physical Review Letters, 106(9), 093902.

[111] Lin, Z., Ramezani, H., Eichelkraut, T., Kottos, T., Cao, H., Christodoulides, D. N. (2011). Unidirectional invisibility induced by P T-symmetric periodic structures. Physical Review Letters, 106(21), 213901.

[112] Ramezani, H., Christodoulides, D. N., Kovanis, V., Vitebskiy, I., Kottos, T. (2012). P T-symmetric Talbot effects. Physical review letters, 109(3), 033902.

[113] Regensburger, A., Miri, M. A., Bersch, C., Näger, J., Onishchukov, G., Christodoulides, D. N., Peschel, U. (2013). Observation of defect states in p t-symmetric optical lattices. Physical review letters, 110(22), 223902.

[114] Peng, B., Özdemir, Ş. K., Rotter, S., Yilmaz, H., Liertzer, M., Monifi, F., Yang, L. (2014). Loss-induced suppression and revival of lasing. Science, 346(6207), 328-332.

[115] Ge, L., Stone, A. D. (2014). Parity-time symmetry breaking beyond one dimension: the role of degeneracy. Physical Review X, 4(3), 031011.

[116] Vysloukh, V. A., Kartashov, Y. V. (2014). Resonant mode conversion in the waveguides with unbroken and broken PT symmetry. Optics letters, 39(20), 5933-5936.

[117] Savoia, S., Castaldi, G., Galdi, V., Alu, A., Engheta, N. (2014). Tunneling of obliquely incident waves through PT-symmetric epsilon-near-zero bilayers. Physical Review B, 89(8), 085105.

[118] Turduev, M., Botey, M., Giden, I., Herrero, R., Kurt, H., Ozbay, E., Staliunas, K. (2015). Two-dimensional complex parity-time-symmetric photonic structures. Physical Review A, 91(2), 023825.

[119] Peng, B., Özdemir, Ş. K., Liertzer, M., Chen, W., Kramer, J., Yılmaz, H., Yang, L. (2016). Chiral modes and directional lasing at exceptional points. Proceedings of the National Academy of Sciences, 113(25), 6845-6850.

[120] Hassan, A. U., Zhen, B., Soljačić, M., Khajavikhan, M., Christodoulides, D. N. (2017). Dynamically encircling exceptional points: exact evolution and polarization state conversion. Physical review letters, 118(9), 093002.

[121] Sakhdari, M., Chen, P. Y. (2019, July). Efficient and misalignment-robust PT-symmetric wireless power transfer. In 2019 IEEE International Symposium on Antennas and Propagation and USNC-URSI Radio Science Meeting (pp. 1459-1460). IEEE.

[122] Fotsa-Ngaffo, F., Tabeu, S. B., Tagouegni, S., Kenfack-Jiotsa, A. (2017). Threshold-less characterization in space and time reflection symmetry electronic dimers. JOSA B, 34(3), 658-667.

[123] Assawaworrarit, S., Fan, S. (2020, December). Efficient and robust wireless power transfer based on parity-time symmetry. In AIP Conference Proceedings (Vol. 2300, No. 1). AIP Publishing.

[124] Sakhdari, M., Hajizadegan, M., Chen, P. Y. (2020). Robust extended-range wireless power transfer using a higher-order PT-symmetric platform. Physical Review Research, 2(1), 013152.

[125] Bender, C. M., Boettcher, S., Savage, V. M. (2000). Conjecture on the interlacing of zeros in complex Sturm–Liouville problems. Journal of Mathematical Physics, 41(9), 6381-6387.

[126] Bender, C. M. (1999). The complex pendulum. Physics Reports, 315(1-3), 27-40.

[127] Mostafazadeh, A. (2002). Pseudo-Hermiticity versus PT symmetry: the necessary condition for the reality of the spectrum of a non-Hermitian Hamiltonian. Journal of Mathematical Physics, 43(1), 205-214.

[128] Peng, B., Özdemir, Ş. K., Lei, F., Monifi, F., Gianfreda, M., Long, G. L., Yang, L. (2014). Parity–time-symmetric whispering-gallery microcavities. Nature Physics, 10(5), 394-398.

[129] Chang, L., Jiang, X., Hua, S., Yang, C., Wen, J., Jiang, L., Xiao, M. (2014). Parity–time symmetry and variable optical isolation in active–passive-coupled microresonators. Nature photonics, 8(7), 524-529.

[130] Li, J., Yu, R., Ding, C., Wu, Y. (2016). PT-symmetry-induced evolution of sharp asymmetric line shapes and high-sensitivity refractive index sensors in a three-cavity array. Physical Review A, 93(2), 023814.

[131] Liu, Z. P., Zhang, J., Özdemir, Ş. K., Peng, B., Jing, H., Lü, X. Y., Liu, Y. X. (2016). Metrology with PT-symmetric cavities: enhanced sensitivity near the PT-phase transition. Physical review letters, 117(11), 110802.

[132] Schindler, J., Li, A., Zheng, M. C., Ellis, F. M., Kottos, T. (2011). Experimental study of active LRC circuits with PT symmetries. Physical Review A, 84(4), 040101.

List of Publications

Publications in International Refereed Journals

NJIKE NJIKE, I.B., Fotsa-Ngaffo, F., Tabeu, S.B., and Kenfack-Jiotsa, A.(2022). Frequency Selectivity and Enhancement of Efficiency in Wireless Power Transfer-Based Parity-Time Symmetric trimer. *Arabian journal for science and engineering*, 47(3), 3659-3667.

Arabian Journal for Science and Engineering
https://doi.org/10.1007/s13369-022-06615-w

RESEARCH ARTICLE-ELECTRICAL ENGINEERING

Frequency Selectivity and Enhancement of Efficiency in Wireless Power Transfer-Based Parity-Time Symmetric Trimer

Idriss Baudouin Njike-Njike[1,2] · Fernande Fotsa-Ngaffo[4] · Stéphane Boris Tabeu[1,2,3] · Aurélien Kenfack-Jiotsa[2]

Received: 8 July 2021 / Accepted: 28 October 2021

Abstract
In this paper, we analyze the mutual induction coupling in a parity-time symmetry electronic system made up of three cells (trimer). This circuit has two transitions separating three phases, namely a real phase and two complex phases. In the real phase where the system oscillates, the efficient transfer reaches almost 100% for a high value of the resistance of the gain and loss cells of the circuit. The maximum distance obtained between the coils when the transfer is still efficient is about 1.5 m for coils with four turns, and this distance increases as the number of turns increases. The transfer curve presents three selective frequencies for which we have the maximum wireless power transmission of signal.

Keywords Frequency · Parity-time symmetry · Selectivity · Wireless power transfer

1 Introduction

Many electrical and electronic devices are powered, charged or connected by cables. Wireless connection simplifies the use of devices in many areas: in medicine for charging heart implants [1–3]; in the telecommunications industry with wireless charging of smartphones [4,5] and in the automotive industry for wireless chargers for electric cars [6–9]. With the evolution of technology, macrosystems are emerging such as wireless energy transfer via a resonant beam [10] to charge different devices in the house. Wireless transfer is positioned as the means of connection for future networks [11] in the fields of detection, signal processing and many others. Wireless transfer systems operate on the basis of capacitive coupling [12], inductive coupling [13] or both together [14]. It is therefore necessary to find electronic circuits that can offer a large transfer distance between the source and the receiver with good efficiency. Takahiro Imura et al. [15] obtained a transfer efficiency of about 97% for wireless charging of electric vehicles at 20 cm and less than 20% when the distance reaches 40 cm. In order to mitigate this problem, Assawaworrarit et al. [16] presented a combined inductive and capacitive system, in which the efficiency is improved to some extent. Zhang et al. [17] review and summarize the various existing wireless mechanisms and classify them in terms of power transfer , efficiency, transfer distance and many others. After the introduction of parity-time symmetric (PTS) systems by Bender et al. [18], many researchers have studied and characterized several configurations of these systems using different couplings. Fotsa-Ngaffo et al. [19] studied the different domains in a coupled RLC dimer and presented how to achieve PT symmetry without transition thresholds. These systems, compared to non-symmetric PT systems, offer new properties such as the existence of transitions that separate the different phases (real, complex and pure imaginary) of the system. Focusing on the real phase of the PT symmetric system, investigations between two RLC cells coupled by mutual induction, capacitive or both, give a better transfer compared to non-PT symmetric systems.

Recent studies have been carried out with RLC cells in series [20]. Assawaworrarit et al. [21] studied wireless transfer in a nonlinear parity-time symmetric circuit. To our

✉ Idriss Baudouin Njike-Njike
njikeiss@gmail.com

1 Laboratory of Mechanics, Materials and Structures, Department of Physics, Faculty of Science, University of Yaoundé I, P.O. Box 812 Yaoundé, Cameroon

2 Nonlinear Physics and Complex Systems Group, Department of Physics, The Higher Teacher's, Training College, University of Yaoundé I, P.O. Box 47 Yaoundé, Cameroon

3 Laboratory of Electronics and Signal Processing, Department of Electrical and Telecommunication Engineering, National Advanced School of Engineering, University of Yaoundé I, P.O. Box 8390 Yaoundé, Cameroon

4 Institute of Wood Technologies, University of Yaoundé I, P.O. Box 306 Mbalmayo, Cameroon

Published online: 10 February 2022

knowledge, no parallel RLC circuit has been studied for wireless transfer, especially in the trimer configuration. We set out to study a PTS system consisting of three mutually inductively coupled cells (Trimer), two of which have the R, L and C components connected in parallel, with a neutral cell in the middle containing the L and C components. After characterization, our system offers a transfer efficiency of about 100% with a distance of about 1.5 m between the coils. Further analysis shows that the maximum transfer distance increases as the number of coil windings increases. The efficiency varies with the Gain-Loss parameter of the system.

The paper is structured as follows. Section 2 presents the electrical model of the trimer and the resulting eigenvalues. In Sect. 3, we study of the eigenvalues and the different transitions. Section 4 gives the dynamic evolution of the system where in the real phase the system exhibits oscillations. In this work, wireless power transmission is studied in Sect. 5. After that, we come to Sect. 6 which summarizes the main results of the paper.

2 Models and Equations

The electronic circuit consists of three oscillators each having a resistance R, an inductance L and a capacitor C (RLC oscillator). The gain cell with an amplification is generated by a negative resistance ($-R$), and the loss cell with an attenuation is introduced by a positive resistance (R). The neutral cell located between the Gain cell and the loss cell has an inductance L and a capacitor C (LC oscillator). The three cells coupled by mutual induction between the coils (wireless coupling) are shown in Fig. 1

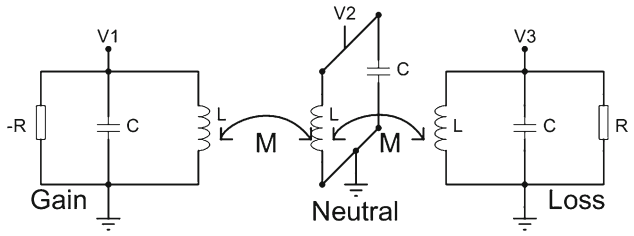

Fig. 1 Electronic trimer circuit consisting of a gain cell having a negative resistance ($-R$) and a loss cell having a positive resistance (R) coupled by mutual induction via a neutral cell

Using Kirchhoff's laws, the equations of the system in the frequency domain can be written as follows:

$$\begin{cases} \frac{\mathrm{d}^2V_1}{\mathrm{d}\tau^2} = -(1-\mu^2)\varepsilon V_1 + \mu\varepsilon V_2 - \mu^2\varepsilon V_3 + \gamma\frac{\mathrm{d}V_1}{d\tau} \\ \frac{\mathrm{d}^2V_2}{\mathrm{d}\tau^2} = \mu\varepsilon V_1 - \varepsilon V_2 + \mu\varepsilon V_3 \\ \frac{\mathrm{d}^2V_3}{\mathrm{d}\tau^2} = -\mu^2\varepsilon V_1 + \mu\varepsilon V_2 - (1-\mu^2)\varepsilon V_3 - \gamma\frac{dV_3}{d\tau} \end{cases} \quad (1)$$

where $\varepsilon = \frac{1}{1-2\mu^2}$ with $0 \le \mu < \frac{\sqrt{2}}{2}$; $\mu = \frac{M}{L}$; $\gamma = \frac{1}{R}\sqrt{\frac{L}{C}}$.

We consider that the voltage of each cell of the circuit oscillates according to $V_j = V_{0j}e^{i\omega\tau}$, inserting into eq.(1), its characteristic equation can be obtained as:

$$\begin{aligned}(2\mu^2-1)\omega^6 \; &+((2\mu^2-1)\gamma^2 - 2\mu^2 + 3)\omega^4 \\ &+(\gamma^2-3)\omega^2 + 1 = 0\end{aligned} \quad (2)$$

By solving the characteristic equation of eq.(2), we obtain the eigenvalues of the system given by:

$$\omega_{1,2} = \pm\left(\frac{1}{6}\frac{(-108DA^2+36CBA+12A\sqrt{3}\sqrt{27A^2D^2-18ABCD+4AC^3+4B^3D-B^2C^2-8B^3})^{1/3}}{A} - \frac{2}{3}\frac{3AC-B^2}{A(-108DA^2+36CBA+12A\sqrt{3}\sqrt{27A^2D^2-18ABCD+4AC^3+4B^3D-B^2C^2-8B^3})^{1/3}} - \frac{1}{3}\frac{B}{A}\right) \quad (3)$$

$$\omega_{3,4,5,6} = \pm\left(\begin{array}{l} -\frac{1}{12}\frac{(-108DA^2+36CBA+12A\sqrt{3}\sqrt{27A^2D^2-18ABCD+4AC^3+4B^3D-B^2C^2-8B^3})^{1/3}}{A} \\ -\frac{1}{3}\frac{3AC-B^2}{A(-108DA^2+36CBA+12A\sqrt{3}\sqrt{27A^2D^2-18ABCD+4AC^3+4B^3D-B^2C^2-8B^3})^{1/3}} - \frac{1}{3}\frac{B}{A} \\ \pm i\frac{1}{2}\sqrt{3}\left(\begin{array}{l}\frac{1}{6}\frac{(-108DA^2+36CBA+12A\sqrt{3}\sqrt{27A^2D^2-18ABCD+4AC^3+4B^3D-B^2C^2-8B^3})^{1/3}}{A} \\ +-\frac{2}{3}\frac{3AC-B^2}{A(-108DA^2+36CBA+12A\sqrt{3}\sqrt{27A^2D^2-18ABCD+4AC^3+4B^3D-B^2C^2-8B^3})^{1/3}}\end{array}\right)\end{array}\right) \quad (4)$$

where $A = (2\mu^2-1)$; $B = ((2\mu^2-1)\gamma^2 - 2\mu^2 + 3)$; $C = (\gamma^2-3)$ and $D = 1$ are coefficients of Eqs. (3) and (4)

3 Eigenmodes Analysis

The eigenvalues given in Eqs. (3) and (4) have phase transitions at the value $\gamma = \gamma_{\mathrm{th}}$. Phase transitions are obtained by solving the expression under the square root $27A^2D^2 - 18ABCD + 4AC^3 + 4B^3D - B^2C^2 = 0$. Coefficients A, B, C and D are given in Eq. (4).

Solving this equation yields four solutions whose real and imaginary parts are shown in Fig. 2a, b, respectively. Analysis of these figures shows that, among the four transitions, two are real (red and green). These two transitions limit the three domains observed on the eigenvalue curves given in Fig. 3. This coupling highlights two exceptional points of

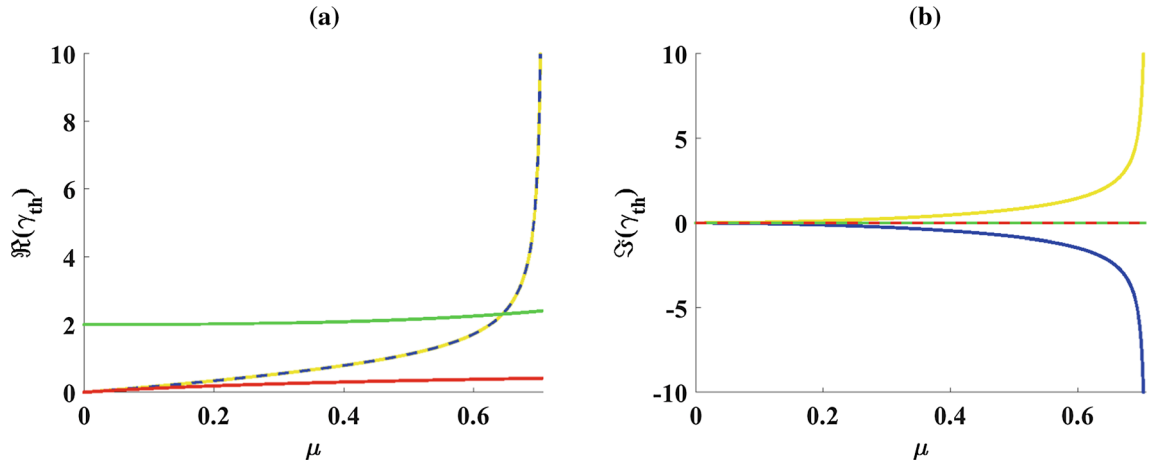

Fig. 2 Evolution of the different transition of system. **a** Real part of transition. **b** Imaginary part of transition

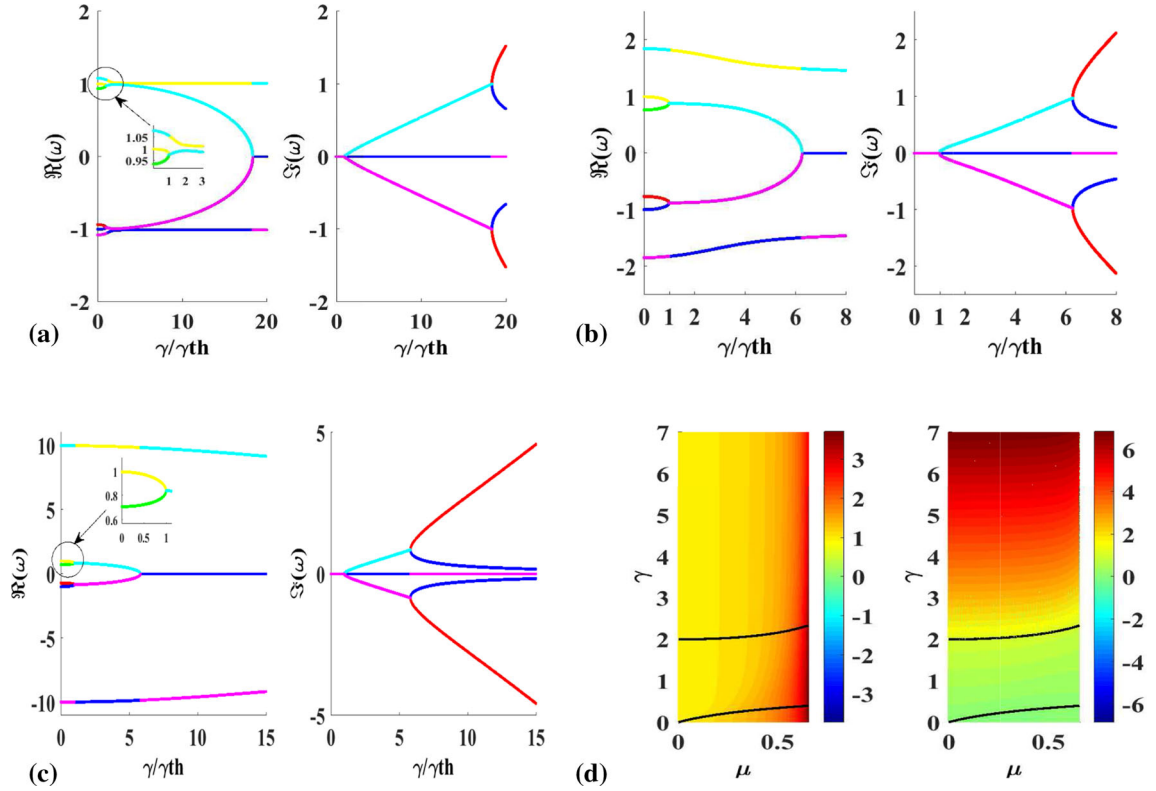

Fig. 3 Evolution of the eigenmode: **a** the real domain is very small and the three frequencies are close ($\mu = 0.1$); **b** one of the three eigenvalues moves away from the other two ($\mu = 0.5$); **c** the real domain is almost constant and the third eigenvalue moves away more and more from the two others which remain close ($\mu = 0.7$); **d** summary of eigenvalues in three dimensions

order two. Before the first transition, the eigenvalues are real (exact phase) and the system shows oscillations. After this transition, in the other two domains, the eigenvalues become complex (broken phase) and the oscillations of the system vary exponentially.

4 Dynamic Evolution

Solving the system of equations yields the time solutions $V_i(t)$ shown in Fig. 4. In the first domain where the eigenvalues are real (i.e. $\Im(\omega) = 0$), as we approach the transition, we go from simple oscillations in Fig. 4a to Rabi oscillations in Fig. 4b. After this transition, the eigenvalues become

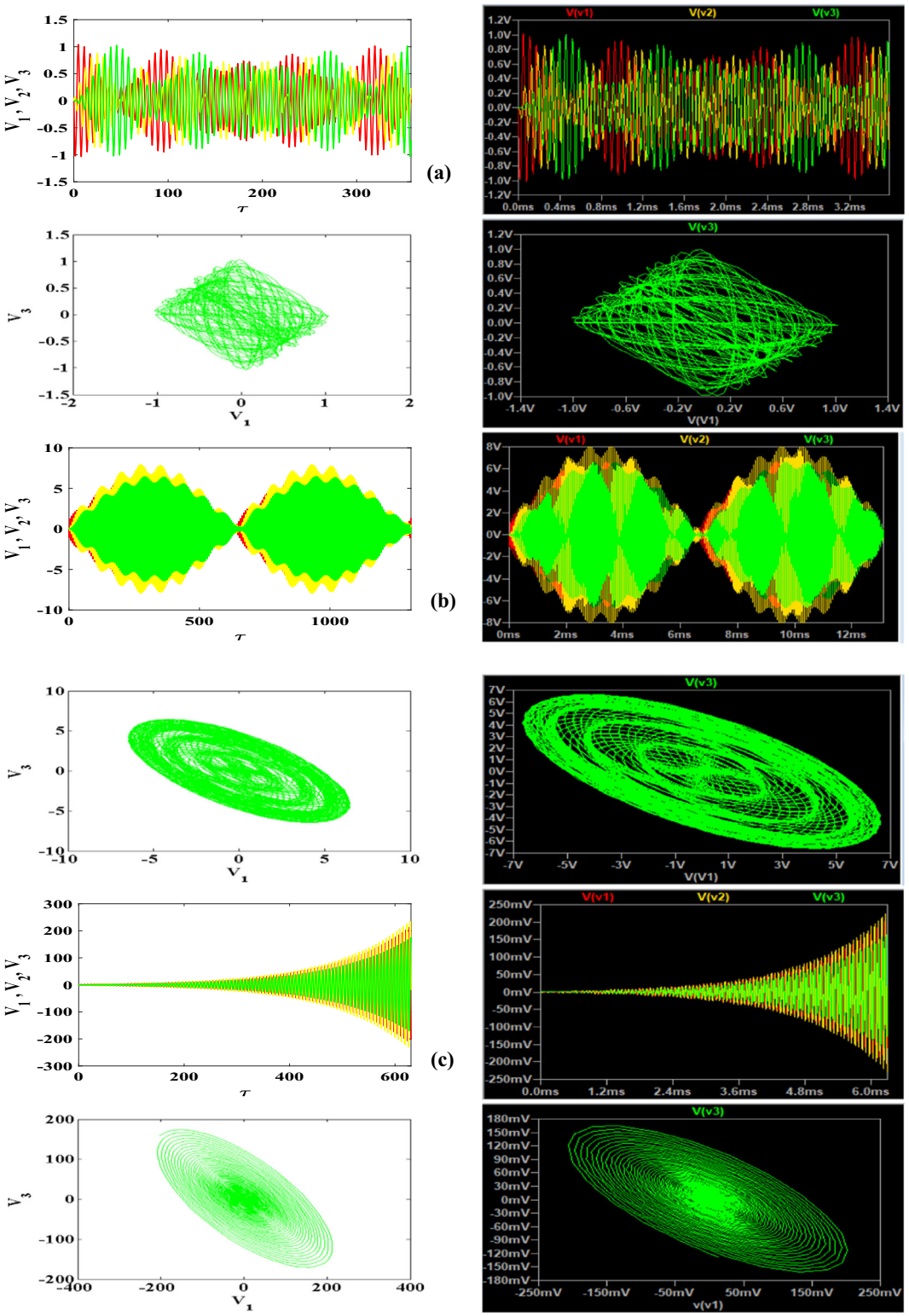

Fig. 4 First column: Real voltage dynamic across the loss, neutral and the gain cells obtained from the numerical simulation at (**a**): $\frac{\gamma}{\gamma_{PT}} = 0.25\,(25\%)$ ($f_{\text{theo}} = 2.23$ kHz, $R = 36.6\ k\Omega$, $f_{\text{exp}} = 2.23$ kHz); **b**: $\frac{\gamma}{\gamma_{PT}} = 0.99\,(99\%)$ ($f_{\text{theo}} = 1.37$ kHz, $R = 9.25\ k\Omega$, $f_{\text{exp}} = 1.73$ kHz) and **c**: $\frac{\gamma}{\gamma_{PT}} = 0.102\,(102\%)$ ($f_{\text{theo}} = 1.26$ kHz, $R = 8.97\ k\Omega$, $f_{exp} = 1.29$ kHz). Second column: experimental verification by simulation in LTspice respectively

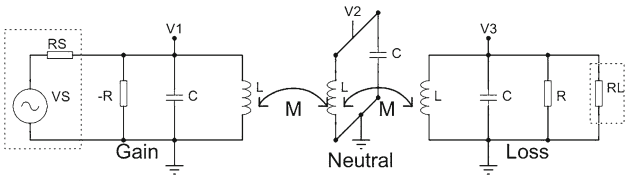

Fig. 5 Circuit of wireless power transfer with the source mounted on the gain cell and the load mounted on the loss cell

complex (i.e. $\Im(\omega) \neq 0$). As a consequence, the oscillations grow exponentially in Fig. 4c. The curves in the first column are obtained with Matlab and those in the second column with the electronic simulation software LTspice. The theoretical frequency (f_{theo}) obtained on Matlab is identical to that obtained by experimental simulation on LTspice (f_{exp}).

5 Wireless Power Transfer with M Coupling

Let's introduce a signal to the gain cell, which here is the source voltage V_s. This voltage is connected in series with R_s, and we place a receiver R_l at the loss cell. The aim here is to determine the transfer function of the system in order to find the distance and the maximum transfer rate of the information between the source and the load.

Applying Kirchhoff's laws to the circuit in Fig. 5, we obtain the system of equations given by Eq. (5):

$$\begin{cases} \frac{V_1 - V_s}{R_s} - Y_1 V_1 + i_1 = 0 \\ V_1 = Z_l i_1 + j\omega M_{12} i_2 \\ Z_e i_2 + j\omega M_{12} i_1 + j\omega M_{23} i_3 = 0 \\ V_3 = Z_l i_3 + j\omega M_{23} i_2 \\ Y_2 V_3 + i_3 = 0 \end{cases} \tag{5}$$

with

$$k_{xy} = \frac{M_{xy}}{\sqrt{L_x L_y}}, \quad x, y = 1, 2 \, or \, 3 \tag{6}$$

By introducing Eqs. (6) into (5) and combining them, we obtain the transfer function of Eq. (7) giving the relationship between the signal on the receiver and the source.

$$\frac{V_l}{V_s} = \frac{\omega^2 k_{12} k_{23} L_2 \sqrt{L_1 L_3}}{\left(\begin{array}{l} L_1 L_2 R_s Y_1 Y_2 Z_l {k_{12}}^2 \omega^2 + L_2 L_3 R_s Y_1 Y_2 Z_l {k_{23}}^2 \omega^2 + L_1 L_2 R_s Y_1 {k_{12}}^2 \omega^2 \\ + L_1 L_2 Y_2 Z_l {k_{12}}^2 \omega^2 + L_2 L_3 R_s Y_2 {k_{23}}^2 \omega^2 + L_2 L_3 Y_2 Z_l {k_{23}}^2 \omega^2 + L_1 L_2 {k_{12}}^2 \omega^2 \\ + R_s Y_1 Y_2 Z_e {Z_l}^2 + R_s Y_1 Z_e Z_l + R_s Y_2 Z_e Z_l + Y_2 Z_e {Z_l}^2 + R_s Z_e + Z_e Z_l \end{array} \right)} \tag{7}$$

where

$$\begin{cases} Z_l = jL\omega \\ Z_c = \frac{1}{jC\omega} \\ Z_e = Z_l + Z_c \\ Y_1 = \frac{1}{Z_c} \\ Y_2 = \frac{1}{R} + \frac{1}{Z_c} + \frac{1}{R_l} \end{cases} \tag{8}$$

$$\begin{cases} R_l = R_{\text{load}} \\ R_s = R_{\text{source}} \end{cases} \tag{9}$$

Using Eq. (8), we calculate the equivalent transfer parameter as in [22] and [23], given by Eq. (10)

$$S_{21} = 2 \frac{V_{\text{Load}}}{V_{\text{Source}}} \left(\frac{R_{\text{Source}}}{R_{\text{Load}}} \right)^{1/2} \tag{10}$$

We take $C = 50$ nF ; $L = 10$ nH ; and $R_s = R_l = 50\Omega$. The frequency is $f = \frac{1}{2\pi\sqrt{5\times10^{-16}}} = 7.1176$ MHz. We consider $k_{12} = k_{23} = \mu = 0.3$.

As the value of the gain-loss parameter (R) increases, the system moves from the complex domain after the second transition to the real domain. Figure 6 shows the evolution of the parameter S_{21} as a function of frequency in the different eigenvalue phases. The system changes from one peak with a low transfer coefficient to three peaks with a high transfer coefficient. These peaks indicate the frequencies at which the transmission is maximum. The troughs between the peaks characterize the frequency ranges at which the transmission is low. In each range, the number of frequencies is related to the number of positive real part eigenvalues. In the complex domain after the second transition, we have a single frequency. Between the two transitions, the system has two frequencies in Fig. 6a related to the two eigenvalues of this domain. In the real domain, the system has three eigenvalues with positive real part which correspond to the three selective frequencies (Fig. 6b) for which the transfer becomes more efficient. When we are close to the beginning of the real domain in Fig. 6c (when the value of R is high), we reach full efficiency (100%).

For a fixed value of R, Fig. 7 presents the transfer function for different values of the mutual induction coupling ($0.0001 \leq \mu \leq 0.5$). Each curve represents the transfer parameter as a function of frequency for a value of μ. The higher the value of the mutual induction coupling, the more

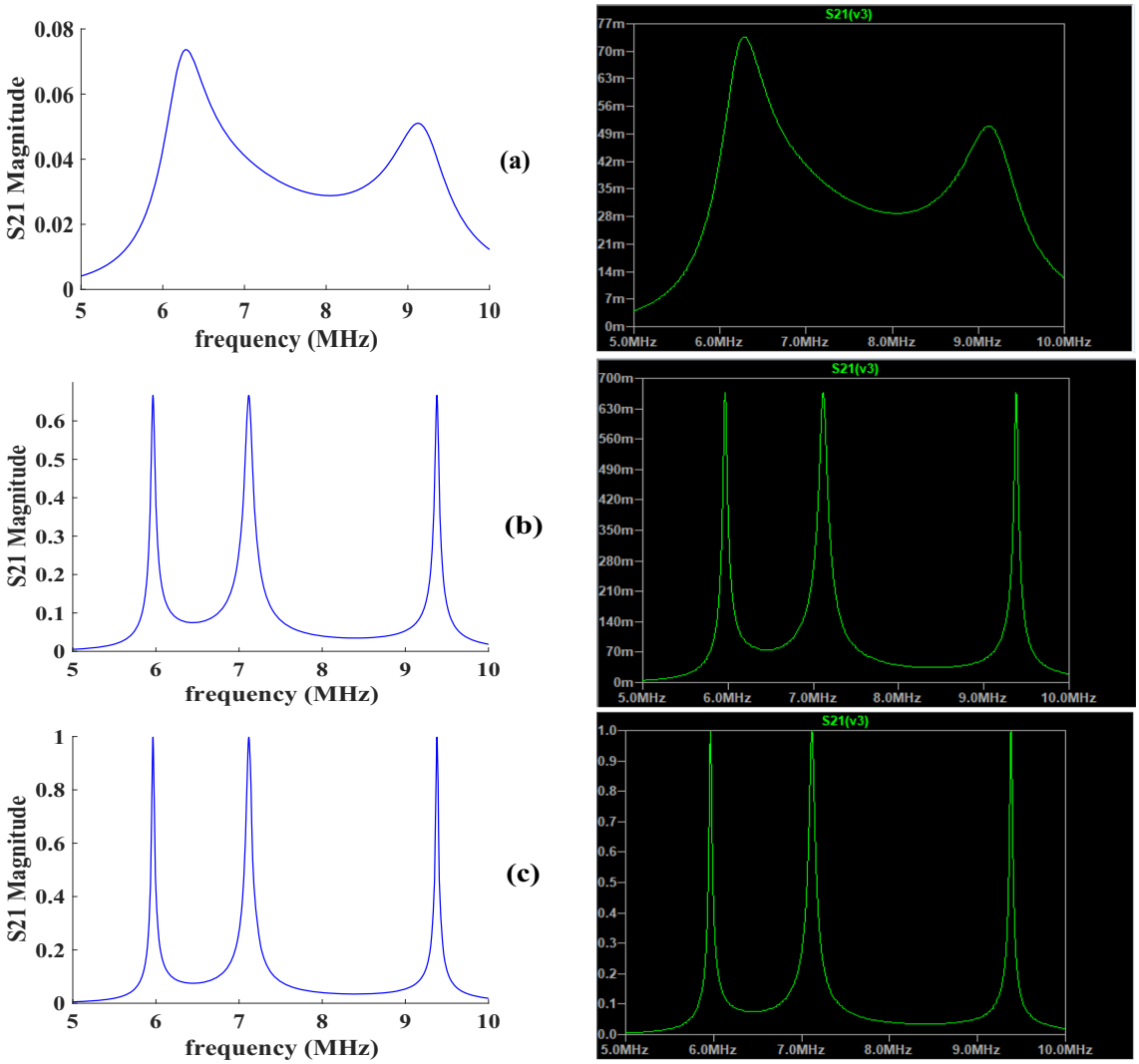

Fig. 6 Evolution of S_{21} as a function of frequency, the left graphs are the matlab curves and the right graphs are the LT curve: **a** complex domain having two eigenvalues with real positive part ($R = 1\ \Omega$); **b** real domain a little far from the first transition ($R = 50\ \Omega$); **c** real domain very far from the first transition ($R = 10\ k\Omega$)

efficient the transfer. When this coupling parameter is low, the distance between the coils is large and the transfer is low.

Figure 8 shows the evolution of the transfer parameter as a function of the mutual induction coupling and the frequency. Let us now determine the maximum distance for which we always have an efficient transfer.

The relation linking the coupling parameter as a function of the distance is given by Eq. (11) [24].

$$M_{12} = M_{23} = \frac{\mu_0 \pi N_1 N_2 (a_1 a_2)^2}{2(a_1^2 + d^2)^{\frac{3}{2}}} \tag{11}$$

where N_1 and N_2 are numbers of turns, a_1 and a_2 are radii and d is the distance between the coils. Using the relation $\mu = \frac{M}{L}$ where $M = M_{12}$, Fig. 9 is obtained from Fig. 8 by replacing the coupling coefficient μ by the distance d extracted from Eq. (11).

Figure 10a shows the evolution of the transfer parameter as a function of the distance between the coils, and Fig. 10b gives the evolution of the frequency as a function of the distance between the coils. For a value of $R = 10k\Omega$, we observe that the transfer is efficient (the efficient transfer reaches 99.8%) over a good distance ($0,3 \leq d \leq 1,5$ m) for three specific frequencies. Zhang et al. [17] list the different results that exist and classify them on several aspects: efficiency, power, distance and many others. Assawaworrarit et al. [21] obtained a total efficiency of 92% and over a distance up to 65 cm between the coils of his circuit. The circuit studied in this paper allows us to obtain an efficient trans-

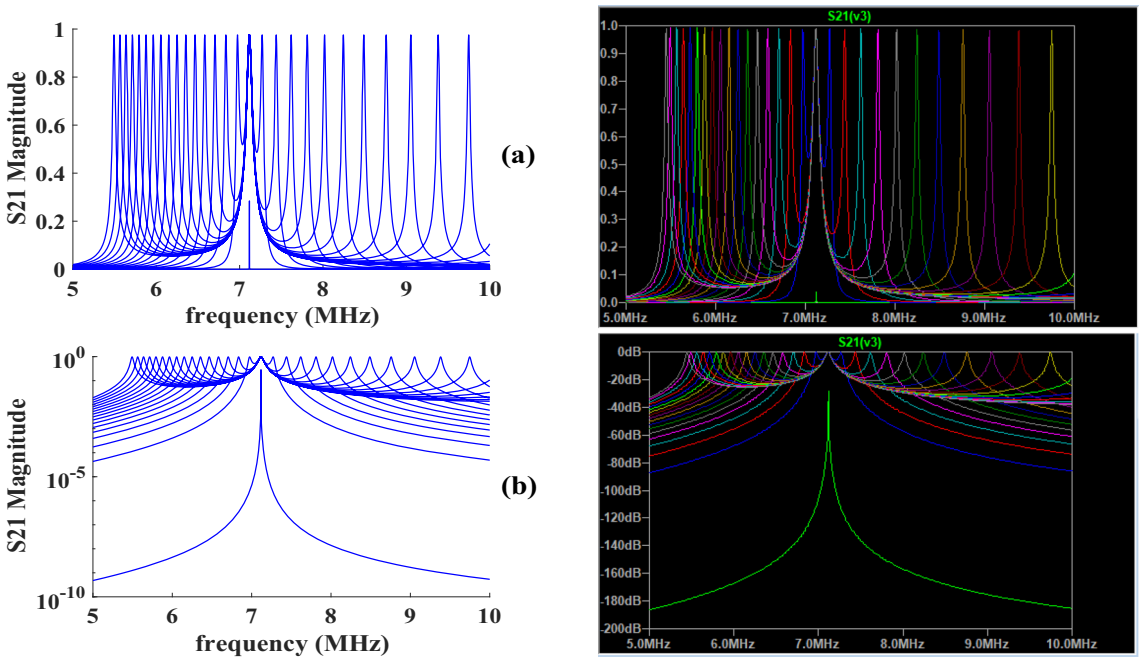

Fig. 7 Evolution of S_{21} as a function of frequency when we vary the coupling parameter and take $R = 1\ k\Omega$. **a** The linear curve obtained on Matlab on the left and on LT Spice on the right. **b** The logarithm curve obtained on Matlab on the left and on LT Spice on the right, respectively

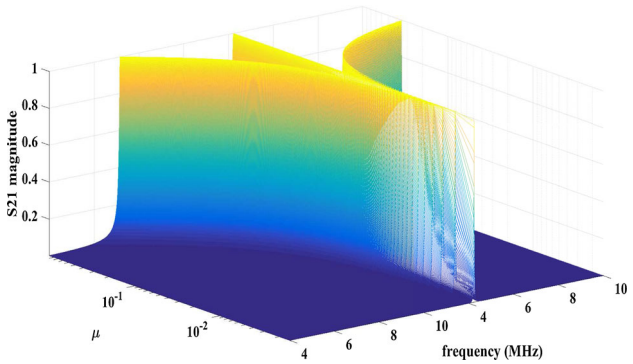

Fig. 8 Evolution of magnitude as a function of frequency and mutual induction coupling between the three coils of the circuit. (c = 50 nF; L = 10 nH; R = 1 kΩ;$R_s = R_l$ = 50Ω ; f = 7.1176 MHz)

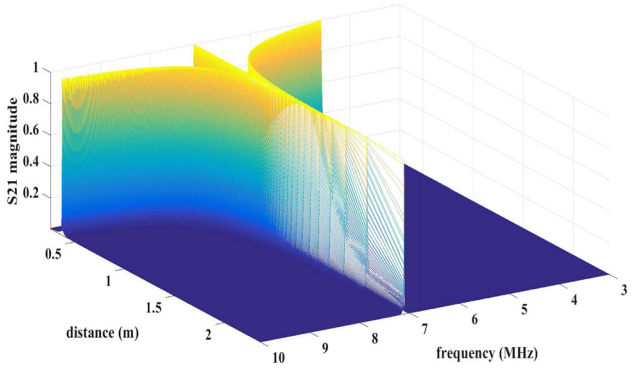

Fig. 9 Evolution of S_{21} as a function of frequency in 3D when we vary the distance and take $R = 1k\Omega$, $N_1 = N_2 = 4$ turns , $a_1 = a_2 = 0.05$ m

fer around 100% over a distance of about 1.5 m. Comparing our results, we notice that our circuit is better in terms of efficiency and transmission distance.

6 Conclusion

In summary, we have performed a study on the characterization of two gain-loss cells separated by a neutral cell and coupled by mutual induction. After the real phase preceding the first transition, the system enters a complex phase. A thorough analysis of this system in the case of a wireless transfer shows that there are specific frequencies for which the transfer is efficient. This system solves the handover distance problem which remains a major challenge when using wireless handover in several domains by giving a good distance between the source and the receiver. Compared to the results found in the literature, these results are better, especially in terms of efficiency and distance. These results solve the problem of existing handover systems that provide maximum handover for short distances. By applying this system in the field of medicine to recharge cardiac implants, the patient is no longer obliged to stay very close to the source. This circuit in the field of telecommunications for charging smartphones and in the automobile for charging batteries will improve the efficiency of the charge. This circuit can also be used for wireless lighting. In the quantum field, it can be

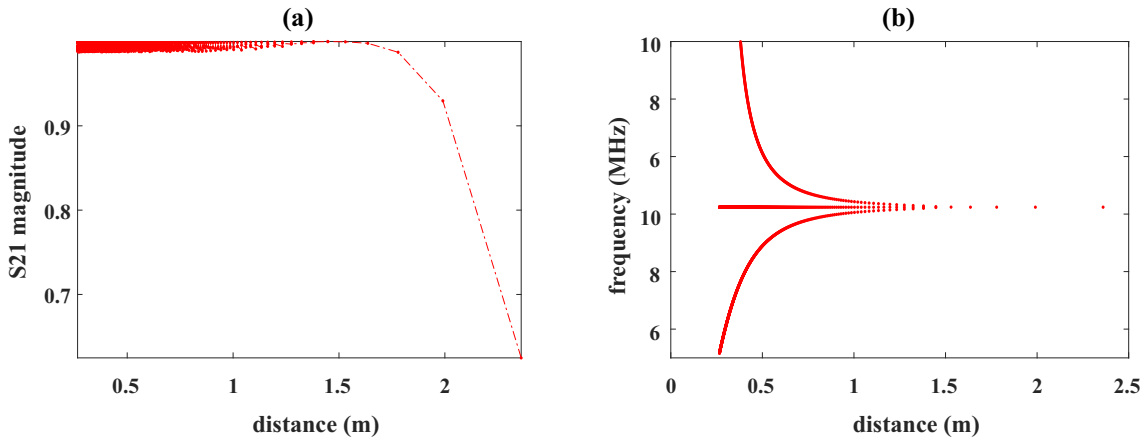

Fig. 10 Evolution of S_{21} as a function of distance and frequency evolution as a function of distance. **a** Maximum efficient transfer as a function of distance. **b** The selective frequencies allowing to have a maximum efficient transfer as a function of distance

used to explain interference phenomena, including electromagnetically induced double transparency.

Supplementary Information The online version contains supplementary material available at https://doi.org/10.1007/s13369-022-06615-w.

Declarations

Conflict of interest The authors declare that they have no conflict of interest.

References

1. Hochmair, E.: System optimization for improved accuracy in transcutaneous signal and power transmission. IEEE Trans. Biomed. Eng. **BME–31**(2), 177–186 (1984)
2. Kush, A.; Rangarajan, J.; Guo, Y.X.; Thakor, N.V.: Wireless power transfer strategies for implantable bioelectronics. IEEE Rev. Biomed. Eng. **10**, 136–161 (2017)
3. Ahn, D.; Hong, S.: Wireless power transmission with self-regulated output voltage for biomedical implant. IEEE Trans. Ind. Electron. **61**(5), 2225–2235 (2014)
4. Zenkner, H.; Ngern, W.K.: Energy transfer by resonance coupling. Int. J. Electr. Comput. Eng. **3**(5), 668–682 (2013)
5. Hui, S.Y.: Planar wireless charging technology for portable electronic products and qi. Proc. IEEE **101**(6), 1290–1301 (2013)
6. Zhu, C.; Liu, K.; Yu, C.; Ma, R.; Cheng, H.: Simulation and experimental analysis on wireless energy transfer based on magnetic resonances. In: Vehicle Power and Propulsion Conference, 2008. VPPC '08. IEEE, pp.1-4, Sept. (2008)
7. Zhang, Z.: Chapter 11 energy cryptography for wireless charging of electric vehicles in energy systems for electric and hybrid vehicles. The Institution of Engineering and Technology, pp. 319-417 (2016)
8. Buja, G.; Bertoluzzo, M.; Dashora, H.K.: Lumped track layout design for dynamic wireless charging of electric vehicles. IEEE Trans. Ind. Electron. **63**(10), 6631–6640 (2016)
9. Rim, C.T.; Mi, C.: Wireless Power Transfer for Electric Vehicles and Mobile Devices. Wiley, Hoboken (2017)
10. Fang, W.; Deng, H.; Liu, Q.; Liu, M.; Jiang, Q.; Yang, L.; Giannakis, G.B.: Safety analysis of long-range and high-power wireless power transfer using resonant beam. IEEE Trans. Signal Process. **69**, 2833–2843 (2021)
11. Clerckx, B.; Huang, K,; Varshney, L.R. et al.: Wireless power transfer for future networks: Signal processing, machine learning, computing, and sensing. arXiv preprint arXiv:2101.04810, (2021)
12. Liu, C.; Hu, A.P.; Wang, B.; Nair, N.C.: A capacitively coupled contactless matrix charging platform with soft switched transformer control. IEEE Trans. Ind. Electron. **60**(1), 249–260 (2013)
13. Covic, G.A.; Boys, J.T.: Inductive power transfer. Proc. IEEE **101**(6), 1276–1289 (2013)
14. Dai, J.; Ludois, D.C.: A survey of wireless power transfer and a critical comparison of inductive and capacitive coupling for small gap applications. IEEE Trans. Power Electron. **30**(11), 6017–6029 (2015)
15. Imura, T.; Okabe, H.; Hori, Y.: Basic experimental study on helical antennas of wireless power transfer for electric vehicles by using magnetic resonant couplings. IEEE Vehicle Power Propuls. Conf (2009). https://doi.org/10.1109/VPPC.2009.5289747
16. Assawaworrarit, S.; Yu, X.; Fan, S.: Robust wireless power transfer using a nonlinear parity-time-symmetric circuit. Nature **546**, 387–390 (2017)
17. Zhang, Z.; Pang, H.; Georgiadis, A.; Cecati, C.: Wireless power transfer: an overview. IEEE Trans. Ind. Electron. **66**(2), 1044–1058 (2019)
18. Bender, C.M.; Boettcher, S.: Real spectra in non-Hermitian Hamiltonians having PT symmetry. Phys. Rev. Lett. **80**, 5243–5246 (1998)
19. Fotsa-Ngaffo, F.; Tabeu, S.B.; Tagoueni, S.: Thresholdless characterization in space and time reflection symmetry electronic dimers. J. Opt. Soc. Am. B **34**(3), 658 (2017)
20. Liu, G.; Zhang, Bo.: Dual-coupled robust wireless power transfer based on parity-time-symmetric model. Chin. J. Electr. Eng. **4**(2), 50–56 (2018)
21. Assawaworrarit, S.; Fan, S.: Efficient and robust wireless power transfer based on parity-time symmetry, International conference on physics and chemistry of combustion and processes in extreme environments (comphyschem'20-21) and vi international summer school modern quantum chemistry methods in applications (2020)
22. Sample, A.P.; Meyer, D.A.; Smith, J.R.: Analysis, experimental results, and range adaptation of magnetically coupled resonators for wireless power transfer. IEEE Trans. Ind. Electron. **58**, 544–554 (2017)

23. Mongia, R.: RF and Microwave Coupled-Line Circuits. Artech House, Norwood (2007)

24. Kim, D.; Abu-Siada, A.; Sutinjo, A.: State-of-the-art literature review of WPT: current limitations and solutions on IPT. Electric Power Syst. Res. **154**, 493–502 (2018)